UC Riverside
UC Riverside Electronic Theses and Dissertations

Title

Electron Transport and Scattering in Graphene Devices Transferred to SrTiO3 Substrates

Permalink

https://escholarship.org/uc/item/2vr0f9sd

Author

Sachs, Raymond

Publication Date

2013

Peer reviewed|Thesis/dissertation

UNIVERSITY OF CALIFORNIA
RIVERSIDE

Electron Transport and Scattering in Graphene Devices
Transferred to SrTiO$_3$ Substrates

A Dissertation submitted in partial satisfaction
of the requirements for the degree of

Doctor of Philosophy

in

Physics

by

Raymond Thomas Sachs

August 2013

Dissertation Committee:
        Dr. Jing Shi, Chairperson
        Dr. Roland Kawakami
        Dr. Vivek Aji

The Dissertation of Raymond Thomas Sachs is approved:

_____

_____

_____

Committee Chairperson

University of California, Riverside

Acknowledgments

my wife Victoria. I would not have ever been able to complete this degree without your unending support. Thank you and I love you! And to my daughter Amelia, you haven't done much yet except scream at me with the occasional smile. In fact, you are sitting in my lap and screaming as I submit the final version of this thesis to Grad Division. But I still love you.

ABSTRACT OF THE DISSERTATION

Electron Transport and Scattering in Graphene Devices
Transferred to SrTiO$_3$ Substrates

by

Raymond Thomas Sachs

Doctor of Philosophy, Graduate Program in Physics
University of California, Riverside, August 2013
Dr. Jing Shi, Chairperson

Graphene has become one of the most widely researched materials lately since its discovery in 2004. It has interested scientists due to the exceptional electronic properties of the relativistic Dirac fermions. In this thesis I will present the research I have done to study the charged impurity scattering mechanism in graphene by placing a device on a high-κ material. An entire device with metal electrodes can be fabricated on SiO$_2$ substrates and transferred to any arbitrary substrate using the device transfer method that I have developed. This method eliminates the need to locate single layer graphene with optical microscopy for alignment and patterning on substrates other than 300nm thick SiO$_2$ which may be very difficult. The target substrate I used is 200μm thick SrTiO$_3$ (STO). The dielectric constant is two orders of magnitude higher than SiO$_2$ at room temperature and increases to 5,000 to 10,000 at cryogenic temperatures. We expected to observe an

associated increase in the mobility with the increased dielectric screening of charged impurities. The mobility is only affected around the Dirac point which is in agreement with theory. An unusual gate dependent hysteretic effect and time dependence is also observed and explained using a surface dipole model of STO. It is graphene that is sensitive to the surface states of the STO.

Table of Contents

List of Figures

Chapter 1
Introduction

1.1   Carbon Allotropes

Carbon, the sixth element on the Periodic Table, is a stimulating material to study. It is the chemical basis for life on Earth and is found in all living organisms. The physical properties of carbon are widely varied and are dependent on the form it is in. The three allotropes of carbon are diamond, graphite, and amorphous carbon.

Diamond is the hardest naturally occurring substance known to man. It is transparent and has low electrical conductivity. The crystal structure is that of a tetrahedron with an additional carbon atom at the center. The lattice resembles a face-centered cubic structure with covalent sp^3 bonds. These properties are in sharp contrast to those of graphite.

Graphite is an exceptionally soft material. It is opaque and has a high conductivity. Stacked sheets of carbon atoms compose bulk graphite. The sheets are held together by weak van der Waals forces while the atoms within the sheets form three sp^2 bonds with nearest neighbors to construct a honeycomb lattice. Graphitic materials will be discussed further.

1.2   Graphene and Graphitic Materials

Graphene was first experimentally discovered in 2004 by Andre Geim and Konstantin Novoselov at the University of Manchester [1]. This discovery earned them the Nobel Prize in Physics in 2010. Graphene is an atomically thin layer of carbon atoms arranged tightly into a two-dimentional (2D) honeycomb lattice. Graphene is the building block for other graphitic materials of different dimensionalities. C_{60}, also known as fullerenes or buckyballs, is a zero-dimensional (0D) graphene sheet curled up to resemble a soccer ball. Carbon nanotubes are the one-dimensional (1D) allotrope of graphene that has been rolled into a tube. And of course graphite is the three-dimensional (3D) form of stacked sheets of graphene. Graphitic materials are illustrated in Fig. 1-1.

Strictly 2D materials were previously thought impossible to create even in a laboratory setting as they would be too thermodynamically unstable [2, 3]. The strong carbon-carbon bond prevents the layer from being destroyed by thermodynamic fluctuations. Graphene and other 2D crystals would remain as only theoretical applications for decades until the now ubiquitous "Scotch tape method" was first employed.
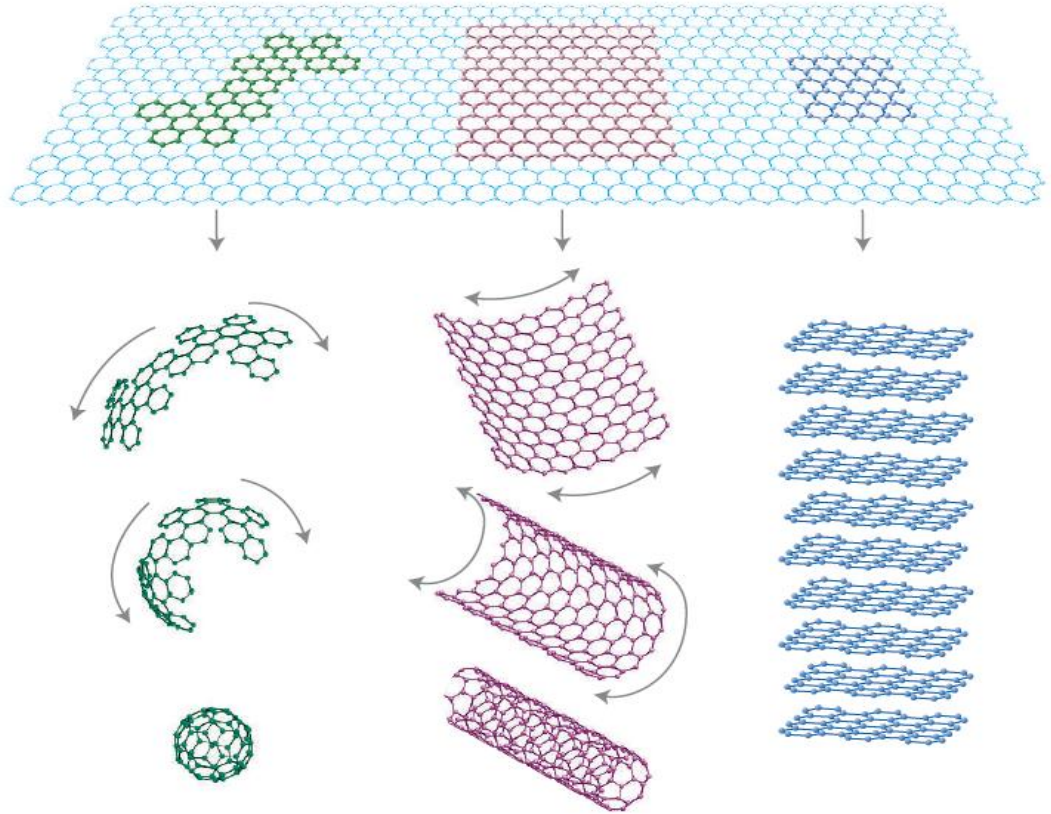
Fig. 1-1 Graphene and its allotropes. Curled into 0D buckyball. Rolled into 1D carbon nanotube. Stacked into 3D graphite [4].

1.3   Graphene Lattice Structure and Dispersion Relation

The honeycomb lattice structure of graphene arises due to the hybridized sp^2 orbital. These three orbitals lie in the same plane and are separated by 120°. The σ-band produced by this orbital structure has filled electron shells and does not contribute significantly to the electronic properties. The π-band, which is oriented 90° with respect to the plane of σ bonds, is half filled and provides the main contribution to the electronic properties. Electrons in this band are weakly bonded

and can easily hop to the nearest neighbor. A triangular Bravais lattice can be constructed for graphene. Two carbon atoms (A and B) are in the unit cell with a nearest neighbor distance of a = 1.42Å. The lattice vectors can be written as

$$\overrightarrow{a_{1,2}} = \frac{a}{2}(3, \pm\sqrt{3}) \qquad (1)$$

The reciprocal lattice vectors have the form

$$\overrightarrow{b_{1,2}} = \frac{2\pi}{a}(1, \pm\sqrt{3}) \qquad (2)$$
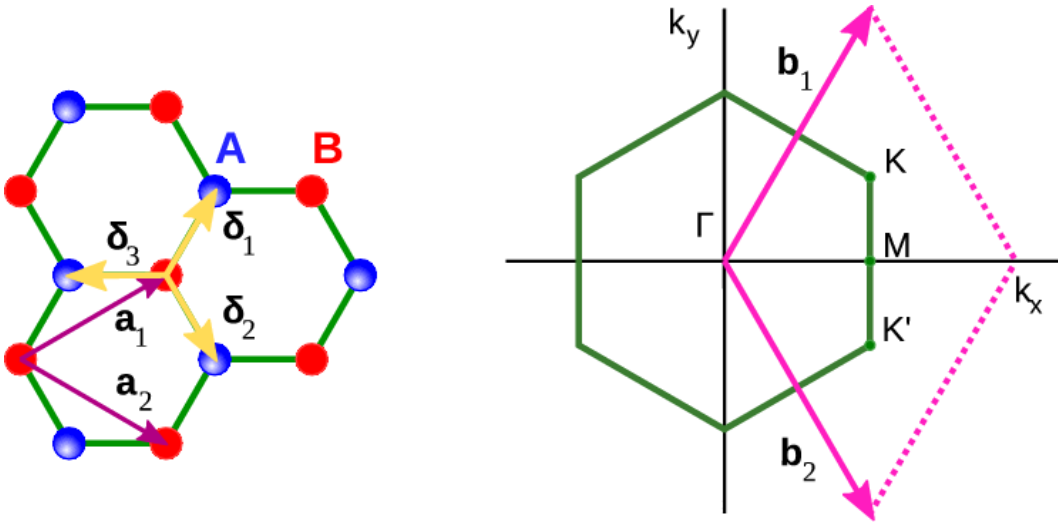
Fig. 1-2 Graphene lattice in real space and reciprocal space.

The symmetry of the graphene lattice provides a simple method for determining the energy spectrum [5]. By assuming that an individual electron resides in a superposition of the same orbits over all atomic sites, the tight-binding method can be used to derive the dispersion relation. Assuming only nearest

neighbor interactions and since all neighboring sites are completely equivalent, the energy bands can be derived in k-space

$$E(\vec{k}) = \pm t \sqrt{3 + f(\vec{k})} \qquad (3)$$

$$f(\vec{k}) = 2\cos(\sqrt{3}k_y a) + 4\cos(\frac{\sqrt{3}}{2}k_y a)\cos(\frac{3}{2}k_x a) \qquad (4)$$

The plus/minus sign accounts for the upper and lower π-band and t = 2.8eV is the nearest neighbor hopping energy. The energy spectrum is highly symmetric with points at the corners of the Brillouin zone touching (but not overlapping). These points at K and K' are called the Dirac points. Fig. 1-3 illustrates symmetric energy dispersion relation with a zoomed-in view of the low energy, linear dispersion around the Dirac points.
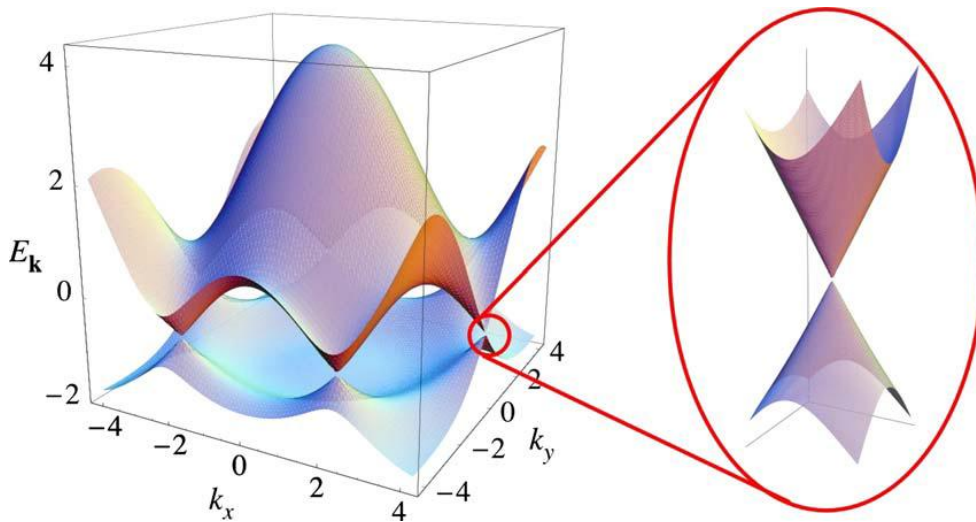
Fig. 1-3 Energy spectrum of graphene. Low energy is linear in k around K and K' (Dirac points).

By expanding Eq. (3) around the Dirac point, a low energy dispersion relation can be derived which is linear in $\vec{k}$

$$E(\vec{k}) = \pm \hbar v_F |\vec{k}| \qquad (5)$$

v_F is the Fermi velocity and is equal to

$$v_F = \frac{\sqrt{3}at}{2\hbar} = 10^6 \, ^m/_S \qquad (6)$$

It is noticeable that Eq. (5) has no dependence on mass. This is in contrast with the energy dispersion for a 2D electron gas

$$E(\vec{k}) = \frac{\hbar^2 \vec{k}^2}{2m} \qquad (7)$$

In most instances, the Schrödinger equation is used when dealing with materials in condensed matter physics. However, the charge carriers in graphene are unique and behave as massless Dirac fermions. Due to the periodic potential of the honeycomb lattice, electrons effectively lose their rest mass and can be described by the Dirac equation [6, 7], hence the name Dirac points for K and K'. The speed of light c is replaced by the Fermi velocity v_F in the equation.

1.4 Electronic Properties of Graphene

The exceptional quality of graphene's electronic properties is evident in its ambipolar electric field-effect. The charge carriers can be tuned by sweeping an

applied gate voltage. The carrier type switches from electrons to holes as the Fermi

energy passes through the Dirac point (Fig. 1-4). Graphene has a high mobility µ that

rivals all semiconductor materials, even under ambient conditions. The mobility

could reach as high as 200,000 cm²/Vs in high quality samples [5]. Charge scattering

serves to limit the mobility. Sources of scattering in graphene will be discussed in

the next chapter.
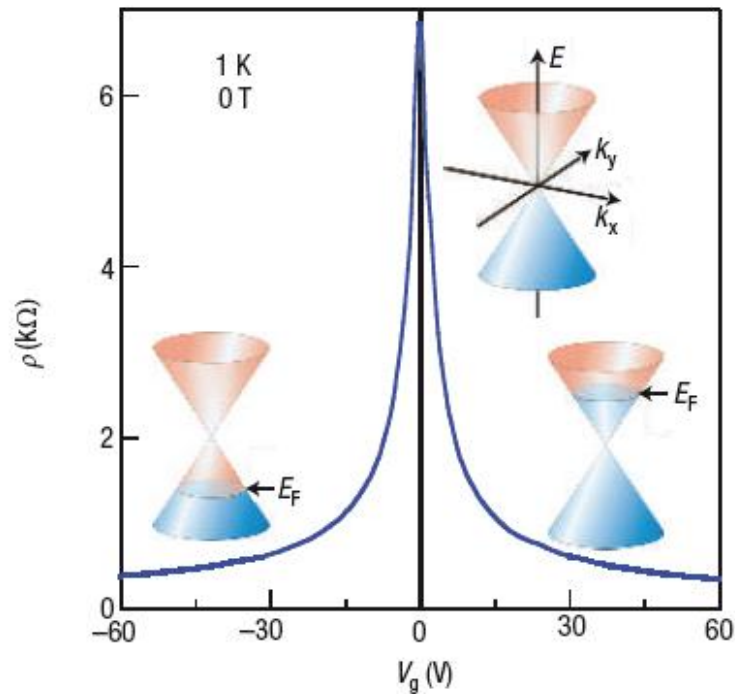
Fig. 1-4 Ambipolar electric field effect in graphene. Carrier density is adjusted
and switches from electrons to holes as Fermi energy passes through Dirac point.

The quantum Hall effect, which is observed in 2D electron systems with a

perpendicular magnetic field, has peculiar features in graphene. Using a high

magnetic field and cryogenic temperatures, the QHE in graphene differs from a conventional QHE in that the filling factors are shifted by a half integer [7, 8]. This is a result of the relativistic nature of the charge carriers and a non-zero Berry's phase of π. The fractional QHE has been observed in ultra-clean, suspended graphene samples [9, 10]. Removing extrinsic effects, such as the substrate and impurities which obscure underlying intrinsic physics, strong correlations between electrons give rise to plateaus at fractional filling factors. These interactions lift the degeneracy due to spin and pseudospin. While QHE has generally been detected at cryogenic temperatures below the boiling point of liquid helium, it is surprising that it has also been observed in graphene at room temperature [11].

In addition to the superior electronic properties of ultra-clean graphene [1, 4, 7-10] there are a host of additional intriguing properties that make it an important contributor to carbon-based technology. The high quality of the crystalline structure is evident by imaging with a scanning tunneling microscope [12, 13]. The thermal conductivity of graphene suggests that it can outperform carbon nanotubes in heat conduction [14, 15]. It is also the strongest material that has ever been mechanically tested [16, 17]. Graphene is also an attractive material in the field of spintronics [18, 19]. With the small atomic number of carbon, a low spin-orbit interaction and hyperfine coupling is expected to produce an intrinsic spin lifetime on the order of microseconds. However, this thesis will focus on the electronic properties and charge transport in single layer graphene.

Chapter 2
Scattering in Graphene

The excellent electronic properties in graphene have drawn the interest of physicists. Many novel electronic applications can be realized. The robust nature of the sigma bonds makes it difficult to replace a carbon atom in the lattice. Because of this, the mean-free-path is rather large and the carrier mobility is exceptionally high. The theoretical absence of backscattering has led to speculation that mobility could be extremely high even at room temperature. However, mechanisms for scattering, both intrinsic and extrinsic, exist in graphene which serves to limit the mobility. Sources of scattering will be discussed further.

2.1 Phonon Mediated Scattering

Graphene has an advantage over other high mobility 2D systems such as GaAs in that it lacks strong long-range polar optical phonon scattering [20]. This should lead to very high intrinsic mobility in clean, defect-free graphene limited only by weak deformation-potential scattering from acoustic phonons. However, it has been shown that electron-acoustic phonon scattering in clean graphene on SiO_2 is indeed independent of the carrier density, but contributes only ~30Ω to the room temperature resistance [21]. This resistivity contribution is strongly temperature dependent above 200K. This dependence on temperature and carrier density is

consistent with extrinsic scattering in graphene caused by surface phonons in the

SiO$_2$ substrate.
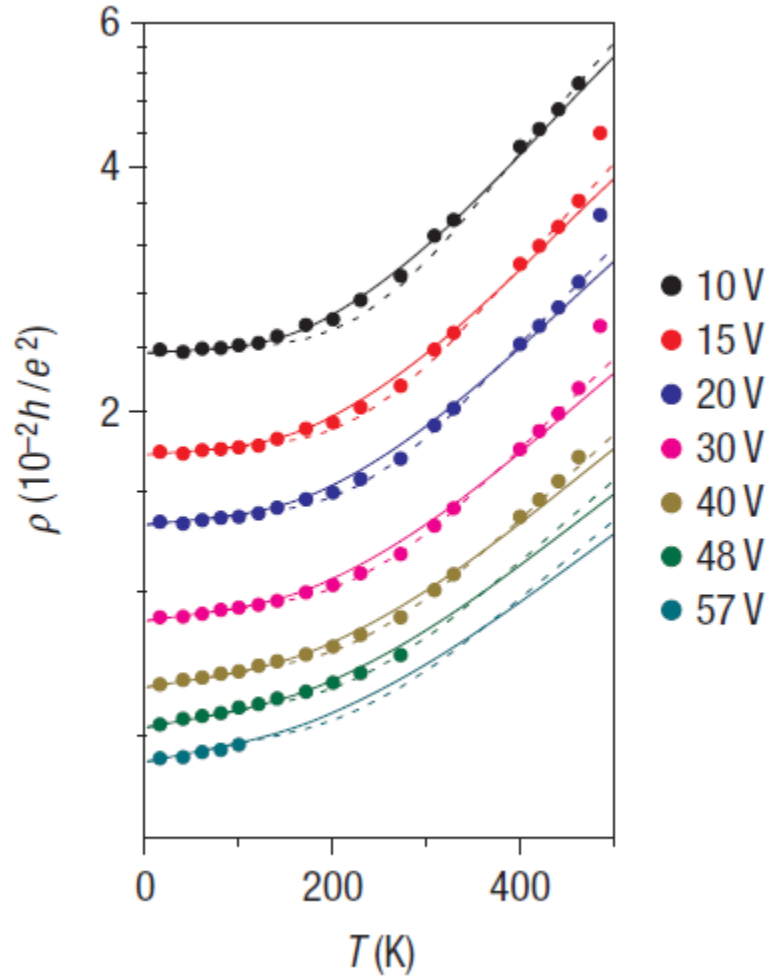
Fig. 2-1 Temperature dependent resistivity of graphene sample. Solid lines are a fit for acoustic and optical phonon scattering in SiO$_2$ substrate. Dashed lines are a fit for acoustic phonon scattering plus a Bose-Einstein term [21].

At low temperature, the longitudinal acoustic (LA) phonon scattering is

expected to be independent of carrier density and linear in temperature:

$$\rho(V_g, T) = \rho_0(V_g) + \rho_A(T); \quad \rho_A(T) = \left(\frac{h}{e^2}\right)\frac{\pi^2 D_A^2 k_B T}{2h^2 \rho_s v_s^2 v_F^2} \quad (1)$$

The residual resistivity is given by $\rho_0(V_g)$ and the acoustic phonon resistivity

contribution is given by $\rho_A(T)$ High temperature resistivity by contrast is expected

to be non-linear and highly dependent on gate voltage.

$$\rho(V_g, T) = \rho_0(V_g) + \rho_A(T) + \rho_B(V_g, T) \quad (2)$$

Zone boundary (ZA) phonons and optical (ZO) mode phonons are out-of-plane

phonons, are not observed in carbon nanotubes [22, 23], and are not expected to be

strong scatterers in graphene. The strong carrier density dependence of graphene

optical phonons scattering is inconsistent with experimental results [21].

Remote interfacial phonon (RIP) scattering is known to be a limiting factor of

carrier mobility in 2D structures. The polar nature of a gate dielectric causes the

carriers to couple to the long-range polarization field created at the dielectric

interface. It has been shown that epitaxial graphene on SiC has weakly interacting

RIP scattering due to the low polarizability of the substrate and the high phonon

frequencies of the Si-C bond. RIP scattering is much stronger in SiO_2 [24]. The

supremacy of RIP scattering over LA phonon scattering at room temperature poses

a remarkable dilemma. A material with higher dielectric constants means there are

atomic groups (often metal-oxygen bonds) which are easily polarized [25, 26]. This

easy polarization means the frequency of RIP phonons is small and leads to higher

occupation numbers for phonons. While graphene on a high-κ substrate will have a suppression of Coulomb scattering due to dielectric screening, the electron scattering by RIP will necessarily be stronger at room temperature [21, 24].

Remote Oxide Phonons (ROP) have been used to explain the behavior of temperature dependent resistivity in graphene on SiO_2 with an amorphous HfO_2 overlayer with higher κ grown with ALD[27].
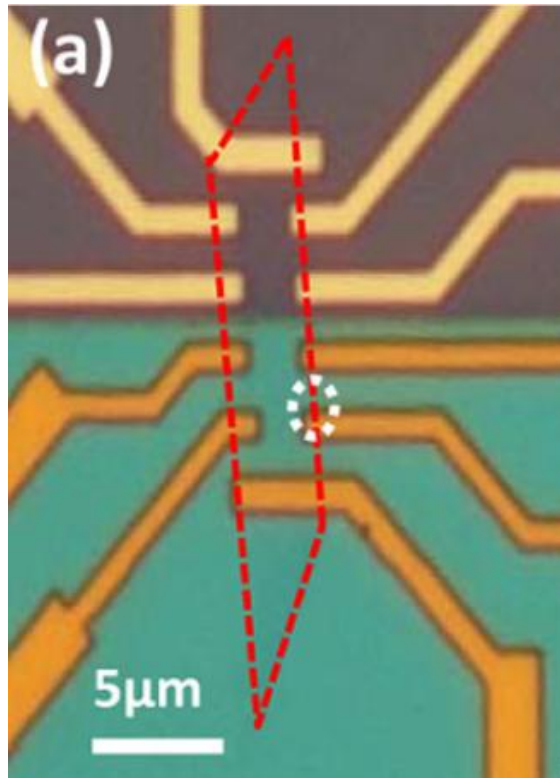
Fig. 2-2 Optical microscope image of graphene device partially covered by 30nm HfO$_2$ (bottom half, green) [27].

At low temperature (10 – 100K) the dependence of pristine and HfO_2 covered graphene is linear and is in agreement with previous work [21]. Above 100K, the

slope for HfO_2 covered graphene increases faster than the pristine side. A model incorporating ROP scattering contribution fits well with the data.
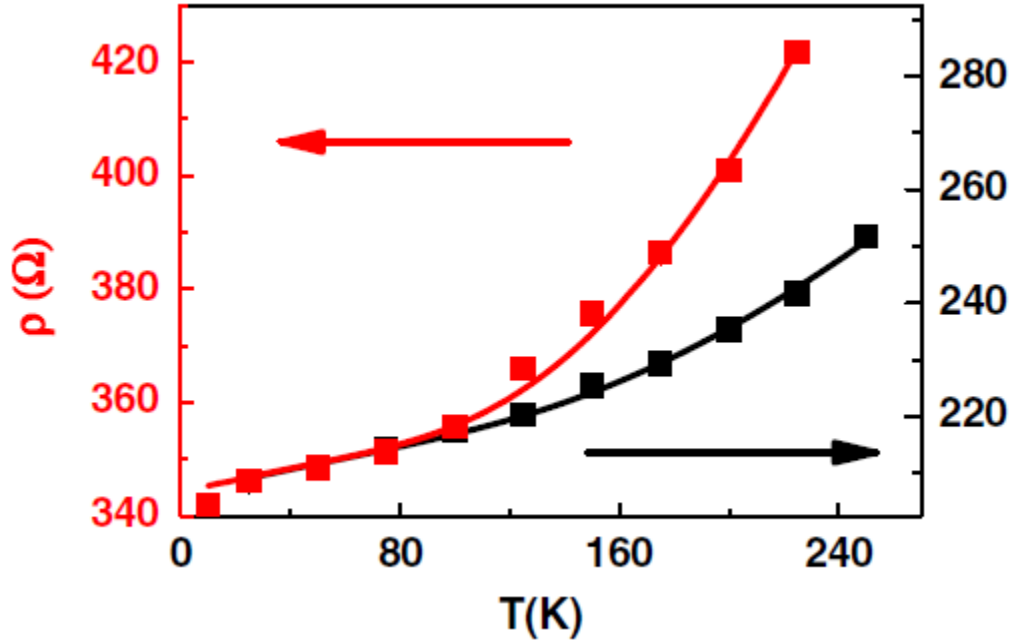
Fig 2-3 ρ(T) of HfO₂ covered graphene device. Red is for device covered with 30nm HfO_2. Black is pristine graphene. Measurement done at $n = 3.0 \times 10^{12}$ cm^{-2} [26].

The ROP scattering at high temperature serves to limit the carrier mobility in HfO_2 covered graphene to 20,000 cm²/Vs. The mobility was calculated from the field-effect ($\mu_{FE} = (d\sigma/dn)(1/e)$).

Temperature dependent measurements have also been done on suspended graphene devices [28] and are considerably different than SiO_2 supported graphene devices [21]. While for supported devices, ρ(T) is linear at 10K < T < 100K and superlinear for T > 100K, ρ(T) for suspended devices is separated into two regimes for high and low carrier density. Pristine suspended devices exhibit non-metallic

behavior at low density (ρ increasing with decreasing T), but high density exhibits

metallic behavior (ρ decreasing with decreasing T).
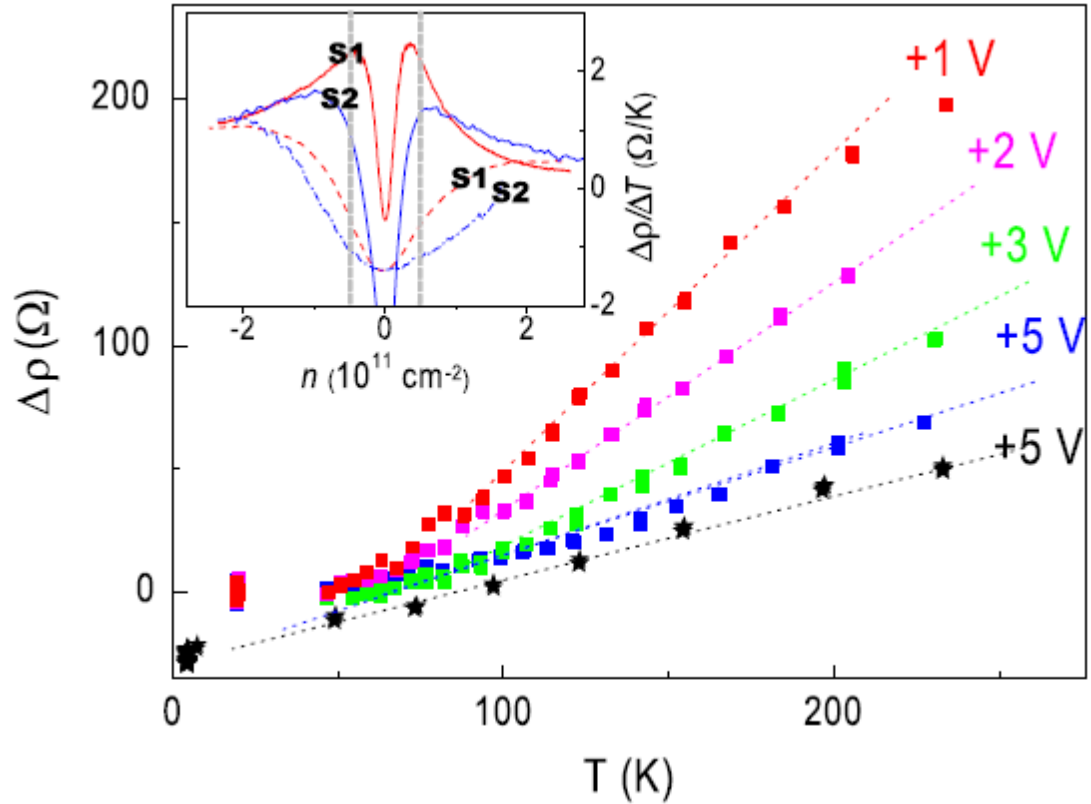
Fig. 2-4 Temperature dependence of suspended graphene devices.

The absence of the superlinear behavior at high temperature in suspended devices

suggests that it is not an intrinsic property of graphene but emanates from the SiO_2

substrate via RIP scattering.

2.2 Ripples in Graphene

Scattering can also arise from microscopic corrugations in the graphene sheet. This disorder is unavoidable due to the strictly 2D crystals being tremendously soft and flexible and, in fact, on the verge of structural instability.
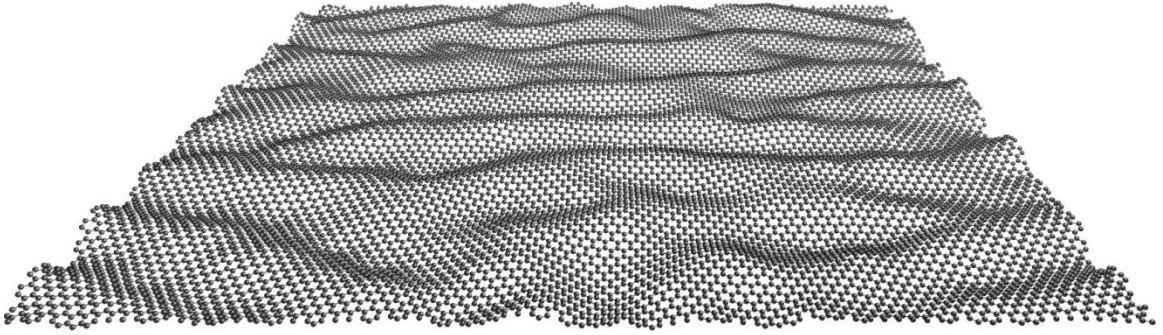
Fig. 2-5 Illustration of ripples in graphene. Image hosted at website http://chaos.utexas.edu.

Local curvature of a graphene sheet will change the interatomic distances and angles between the C-C bonds. This change in nearest-neighbor hopping parameter is equivalent to the appearance of a vector potential and the change in next-nearest-neighbor hopping also leads to an electrostatic potential. Both potentials contribute similarly to the resistivity [29]. From the potentials, the resistivity contribution can be calculated:

$$\delta\rho \approx \frac{h}{4e^2}\frac{z^4}{R^2 a^2} \qquad (3)$$

R and z are the radius and height of the ripple and a is the interatomic distance.

Experiments have shown that ripples in graphene sheets, although present, are very small. The average ripple height is Δ= 1.9Å while the in-plane correlation length is ξ= 320Å [13]. Using Boltzmann formalism, Adam and Das Sarma [30] calculated the resistivity and mean-free-path for surface roughness:

$$\rho_{R=}\frac{h}{e^2}\frac{8\sqrt{\pi}k_F\Delta^2 r_S^2}{\xi} \qquad (4)$$

$$\ell_R = \frac{\xi}{16\sqrt{\pi}k_F^2 r_S^2 \Delta^2} \qquad (5)$$

Using values for the Δ and ξ from experiment, the mean-free-path ℓ_R is typically larger than the sample size. This removes the uncertainty on whether electron scattering from graphene ripples has any discernible effect on the transport properties of graphene.

Theoretical calculations of electron transport properties of epitaxial graphene on SiC over a substrate step has concluded that very little change in resistance arises from the change in morphology as the graphene bends over steps of varying heights [31]. The resistance is nevertheless increased, in agreement with experiment [32], and is explained as arising almost entirely from the coupling between the graphene and the substrate which varies dramatically in the vicinity of the step.
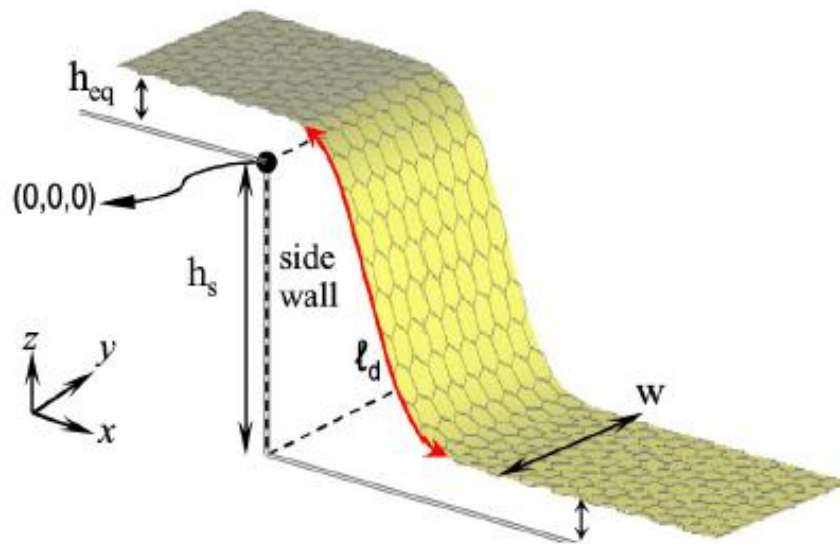
Fig. 2-6 Illustration of graphene over a substrate step. [31]

It is sensible to consider that not much can be done to change the rippled configuration of graphene on a substrate. As a free-standing membrane prior to exfoliation, the graphene sheet is subject to dynamic out-of-plane thermal fluctuations. When brought into contact with a substrate, the van der Waals force instantly pin it to the surface where it becomes static and robust at all temperatures.

2.3   Short-Range Scattering

Short-range scattering can occur in graphene due to defects or dislocations in the carbon lattice. Theoretically, these point defects and resonant scatterers are expected to play a more dominant scattering role in devices with very high mobility (due to the low charge impurity concentration) and at high carrier density.

In contrast to charged impurity scattering which gives a conductivity that is linearly proportional to the carrier density, short-range scattering is expected to give rise to a constant conductivity [33]. Using the estimation that the highest mobility samples have a ratio of point defect density to charged impurity density of $n_p/n_i \sim 0.2$, sublinear behavior in the conductivity is expected at higher carrier densities.
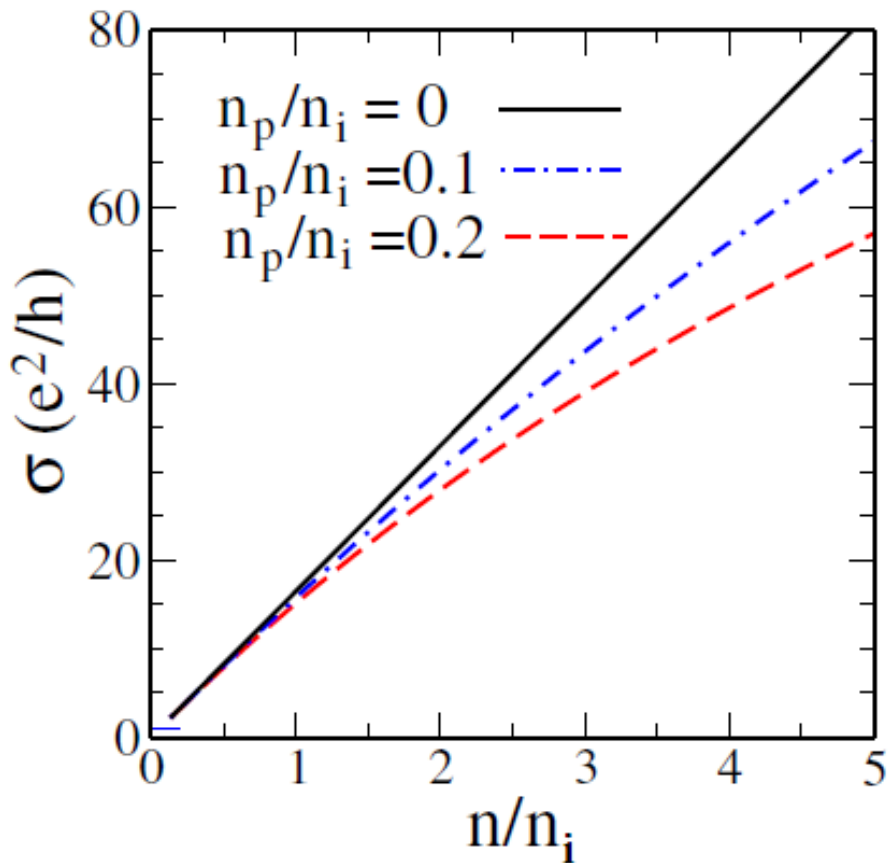
Fig. 2-7 Graphene conductivity calculation using combination of short- and long-range scatterers. Linear behavior is expected for samples with no point defects. Sublinear behavior is likely seen in samples at high density and with low charged impurity density [33].

Experimental data has been in good agreement with theory. Employing the semi-classical Drude model to estimate the mobility of several samples ($\mu = (en\rho)^{-1}$), the samples with the highest mobility exhibit sublinear behavior at high carrier density [34]. In general, for poorer quality samples, the Dirac points are shifted away from $V_g = 0$, indicating a larger charge doping. The difference in slope between devices with varying mobilities is apparent.
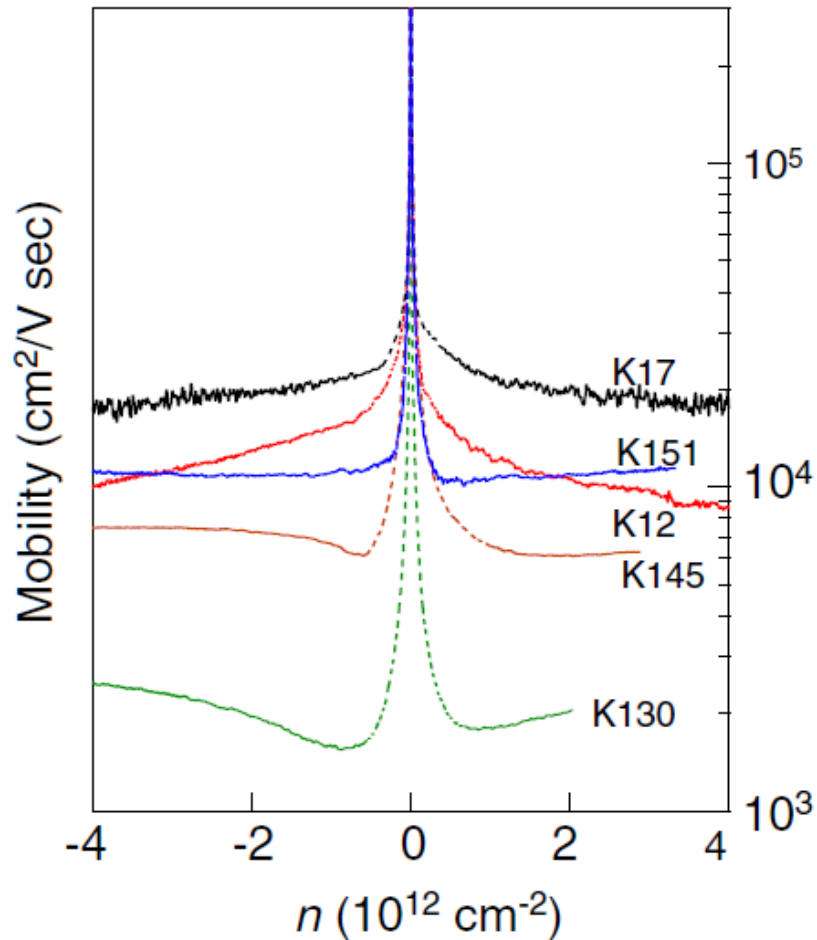
Fig. 2-8 Mobility of graphene devices estimated by the Drude model [34]. Higher mobility is seen in devices with greater short-range scattering.

Fitting the measured conductivity to an equation derived from Boltzmann transport theory with charged impurity scattering:

$$\sigma(V_g) \approx C \frac{e^2}{h} \frac{n}{n_i} \quad \text{for } n > n^*$$

$$(6)$$

$$\sigma(V_g) \approx C \frac{e^2}{h} \frac{n^*}{n_i} \quad \text{for } n < n^*$$
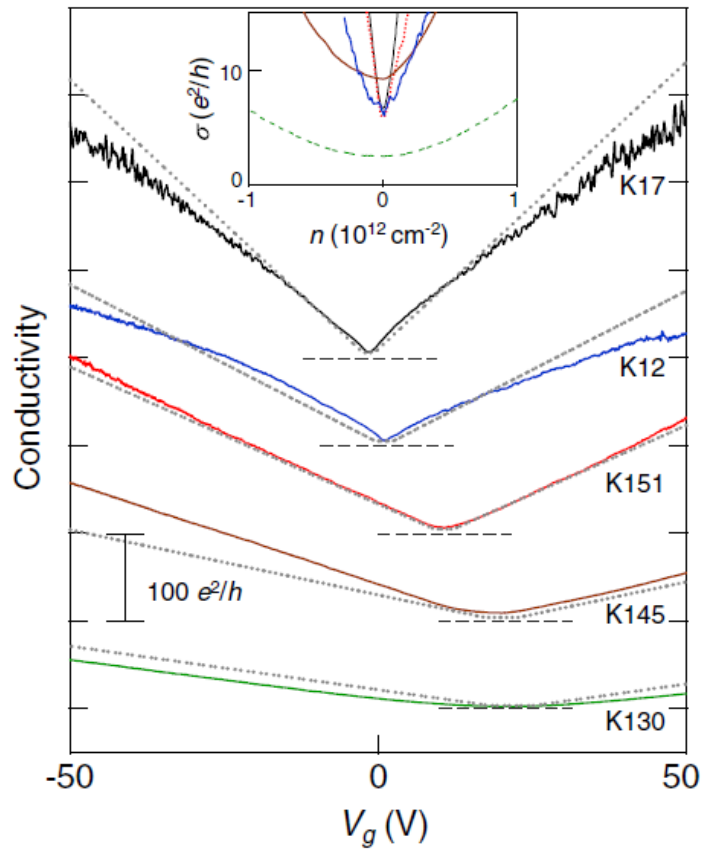
Fig. 2-9 Conductivity of graphene devices with varying mobilities. The dotted line shows a fit to Eq. (6). Curves are vertically displaced for clarity [34].

The self-consistent residual carrier density is given by n^* and takes into account the electron/hole puddles formed. C is a dimensionless parameter describing the scattering strength of potential fluctuations. The only fit parameter, n_i, is calculated to be 2.2, 4.0 4.6, 9.7 and 14.5 (10^{11} cm^{-2}) for samples K17 through K130 respectively [34]. These values are in good agreement to previously reported values [35].

By removing the substrate, the induced carrier inhomogeneity caused by trapped charges at the graphene-oxide interface can be eliminated [36, 37]. This not only leads to higher mobility, but can help to shed light on the effects of short-range scattering. At low carrier densities just outside the electron/hole puddle regime ($n \approx$ 4 x 10^9 cm^{-2}), the mobility for suspended graphene (SG) is significantly higher than non-suspended graphene (NSG), reaching 185,000 cm^2/Vs at 20K. At higher carrier densities ($n > 4$ x 10^{11} cm^{-2}) the mobilities of SG and NSG become comparable at ~10,000 cm^2/Vs. This difference of μ at different n reflects that long-range scatterers are the limiting factor at low n (short-range scatterers are too weak near Dirac point due to small density of states) while at high n short-range scatterers are dominant. Similar conclusions can be made from a calculation of the mean free path (mfp = σh/($2e^2$k$_F$)). A plot of mfp vs. n reveals a positive slope for NSG, indicating long-range scattering. For SG, the negative slope is consistent with the absence of long-range scatterers such as charged impurities. For this work, μ and mfp were calculated from the measured σ [36]. RIP scattering is also necessarily absent in SG.
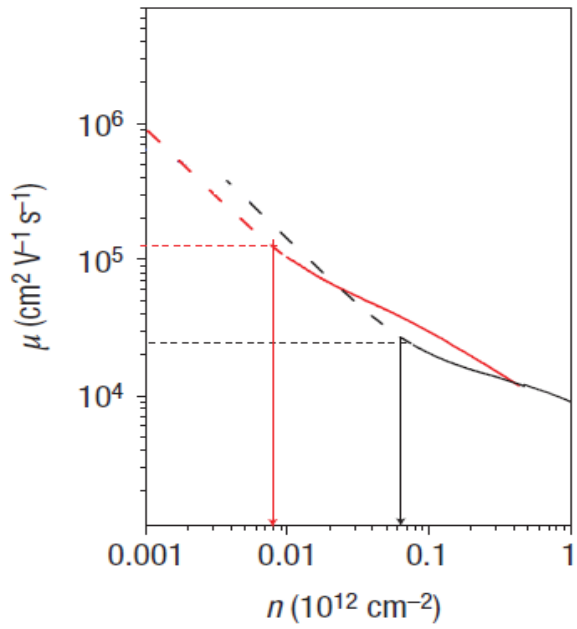
Fig 2-10 Density dependence of mobility for NSG (black) and SG (red). Arrows indicate onset of electron/hole puddle regime [36].
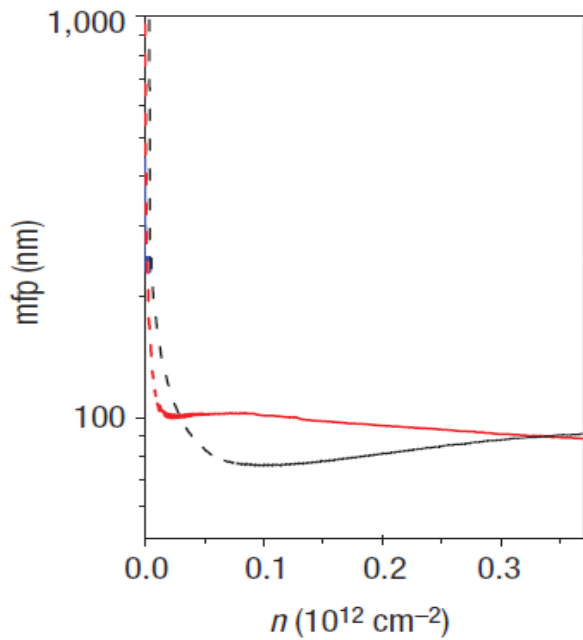
Fig. 2-11Density dependence of mfp for NSG (black) and SG (red) at 100K [36].

Short-range scatterers such as lattice vacancies can be induced in a graphene sheet. Cleaned graphene has been irradiated with Ne⁺ in UHV at low temperature [38]. Raman spectra of the graphene after exposure reveals a *D* peak that was previously absent, indicating significant intervalley scattering (short-ranged) [39].
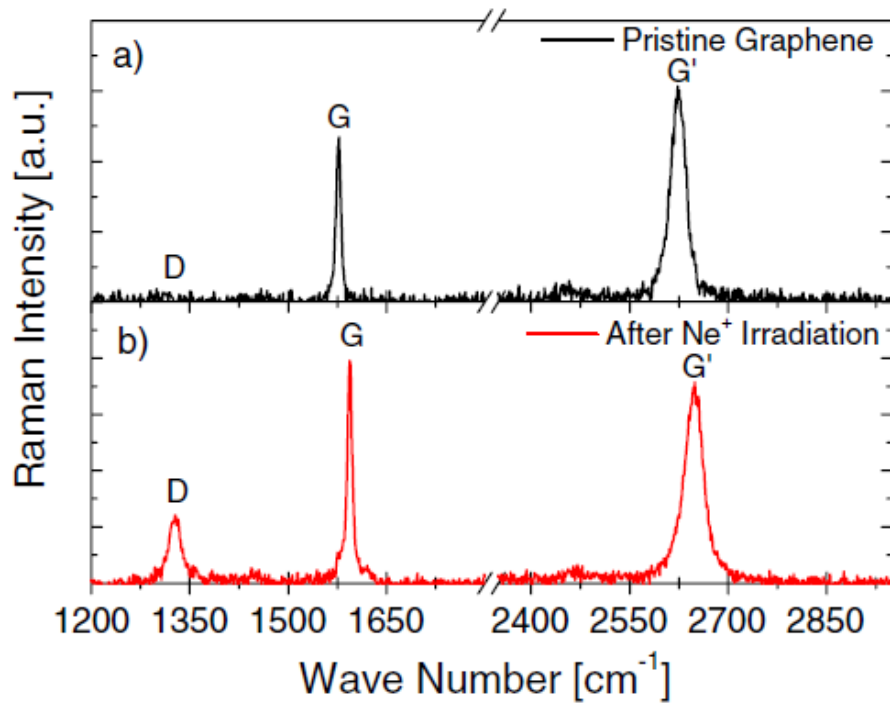
Fig. 2-12 Raman spectra for (a) pristine graphene and (b) after irradiation by Ne⁺. The appearance of a *D* peak indicates local defects have been induced[38].

Measuring $\sigma(V_g)$ for the pristine device and after sequential doses of Ne⁺ irradiation, the slope declines. The decrease in mobility is caused by increased scattering by defects and is 4X lower than a similar covering of charged impurities. The strong disorder is predicted to produce midgap states in graphene which are linear in *n*.
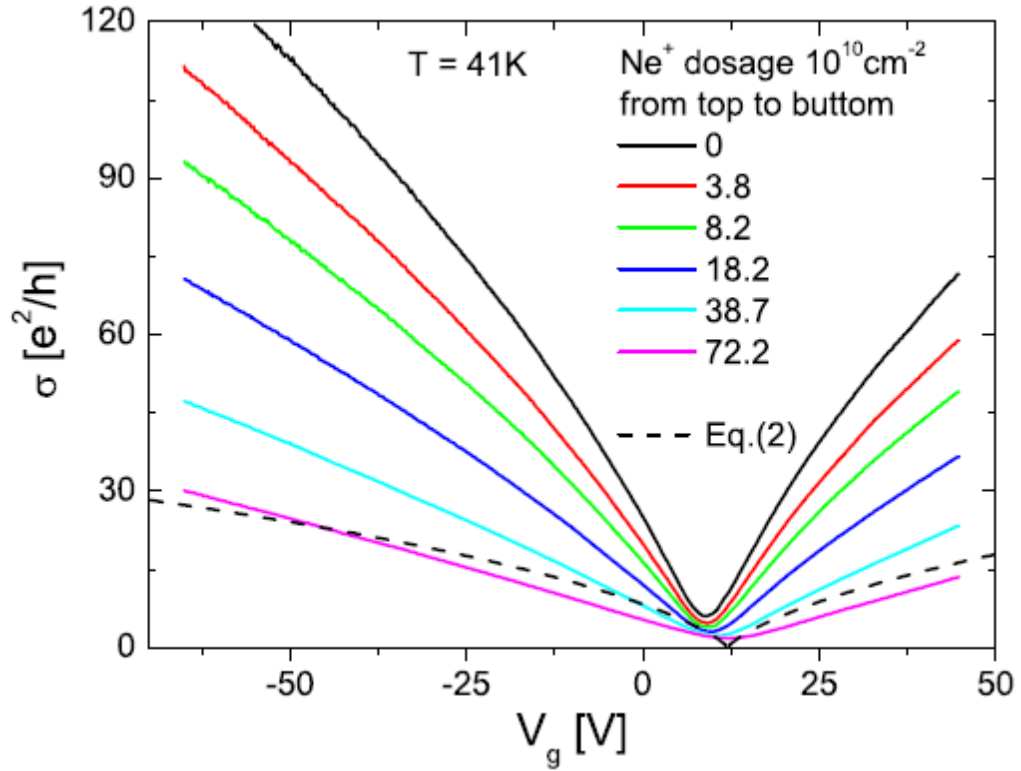
Fig. 2-13 σ vs. V_g for pristine graphene device (black) followed by subsequent Ne⁺ irradiation doses. Mobility decreases with increased exposure [38].

Similar results were observed for the introduction of low energy atomic hydrogen adsorbed on the surface of graphene [40] and via high energy hydrogen plasma [41]. Transport and Raman spectroscopy measurements show that the hydrogen adds a short-range scattering potential which establishes an intervalley scattering. But only a small and finite amount of charge is transferred to the graphene as evidenced by the small shift in the Dirac point voltage. This transferred charge is effectively screened by carriers in graphene [40].
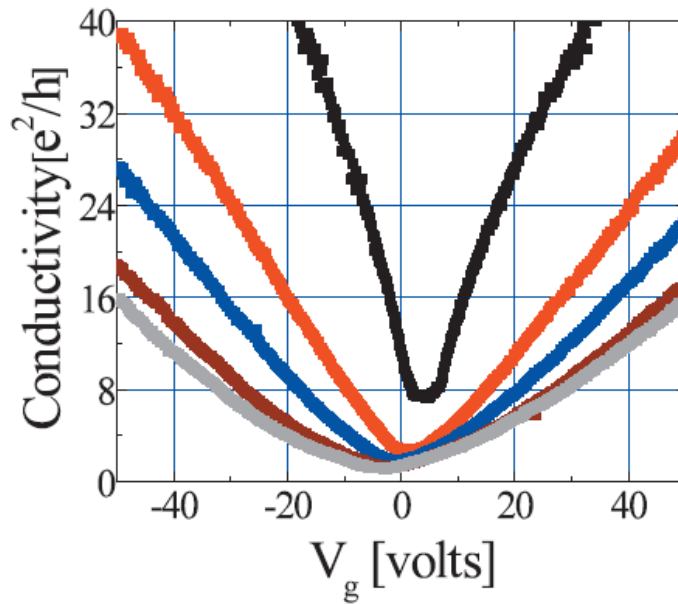
Fig. 2-14 Effect of atomic hydrogen on the transport properties of graphene.
Areal densities (cm^{-2}) of hydrogen atoms are zero (pristine, black), 1.4 x 10^{14} (orange), 2.8 x 10^{14} (blue), 5.6 x 10^{14} (red), 8.5 x 10^{14} (gray) [40].

2.4   Charged Impurity Scattering

Long-range charged impurities are expected to be the dominant scatterers in graphene. These extrinsic Coulomb charge disorders can be found as adsorbates on the surface or as impurities in the substrate itself. The charged impurity model [33, 42 - 46] is in good qualitative agreement with existing experimental transport data. The experimentally observed finite, minimum of conductivity at low density can be explained by the spatially inhomogeneous, random charge puddles, dependent on the charged impurity configuration in the sample.

The Boltzmann transport theory can be used to provide an accurate

determination of the charged impurity density n_i and the mobility can be calculated

in the presence of randomly distributed charged impurities being screened by the

2D electron gas in the random phase approximation (RPA). The Boltzmann theory is

expected to be exact in the high carrier density regime where the system is

homogeneous. The conductivity for graphene comes from the massless, chiral Dirac

spectrum and is given by:

$$\sigma = \frac{e^2}{h} \frac{2E_F \langle \tau \rangle}{\hbar} \qquad (7)$$

The energy averaged finite temperature scattering time is given by $\langle \tau \rangle$ [33]. The

comparison of this theory with experiments [6, 7] is remarkable, as illustrated in

Fig. 2-15.
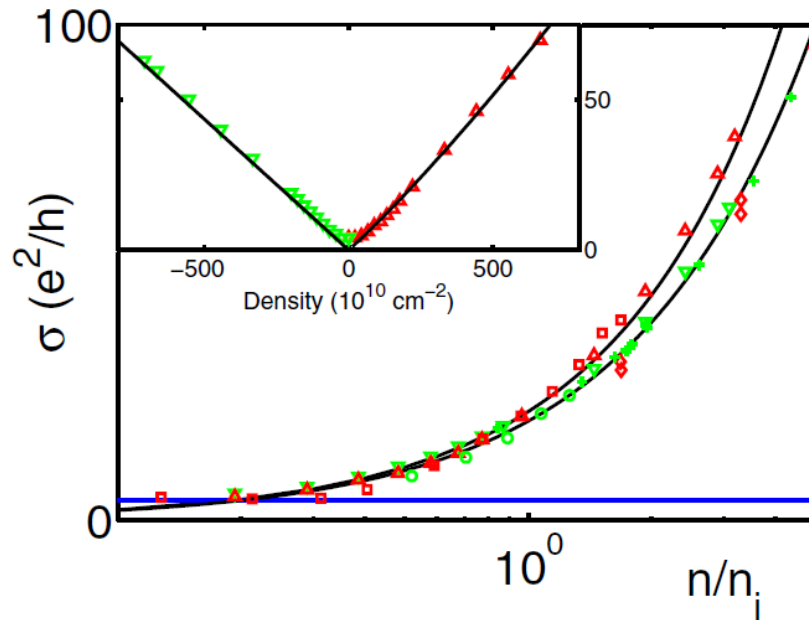
Fig. 2-15 Comparison of experimental data with fit to Eq. (7) [33].

By introducing charged impurities on the surface of graphene in a controlled

environment the veracity of the charged impurity model can be probed. Chemical

doping of graphene by NO_2 gas appears to have a negligible effect on the carrier

mobility. The doping only shifted the Dirac point to the right indicating hole doping,

without changes to the overall shape of the plot (Fig. 2-16)[47]. Complimentary Hall

effect measurements show the mobility $\mu_H = \rho_{xy}/\rho_{xx}B$ is also unaffected by the

doping and the values are very close to those determined by the electric field-effect.
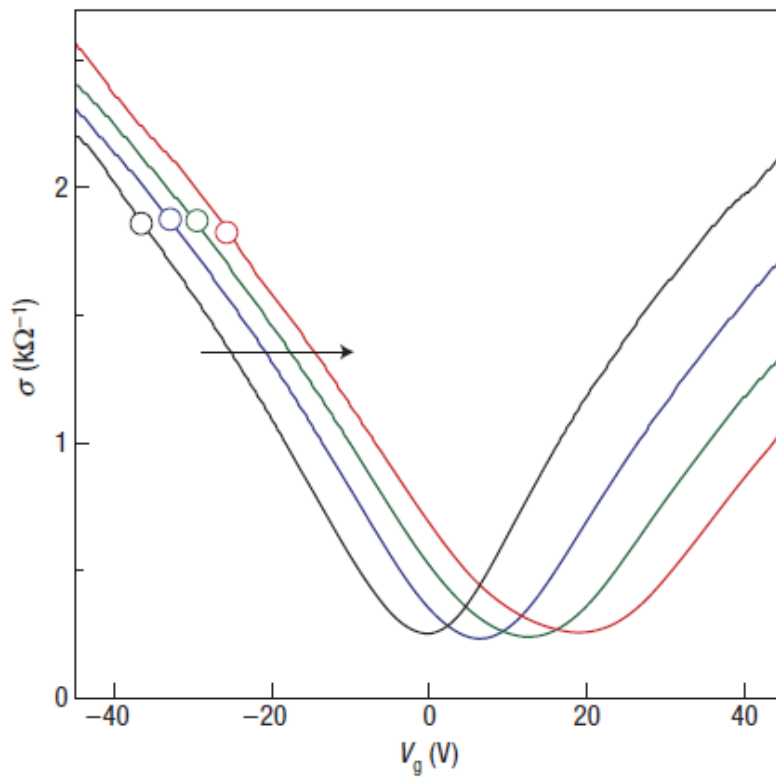
Fig. 2-16 Doping of graphene by NO_2. Increased from zero (black) to ~1.5 x 10^{12}cm^{-2} (red)[47].

Additional research has been done to dope graphene with impurities. To vary the density of charged impurities, thoroughly cleaned and pristine devices have been dosed with a potassium flux at T = 20K in sequential 2 second intervals [48, 49]. The potassium donates an electron to graphene, leaving a positive ion as a charged scattering center. The plot of σ vs. V_g (Fig. 2-17) reveals several interesting points. The slope decreases indicating that the mobility is decreasing. The pristine device exhibits sublinear behavior at high carrier density, but with successive K-doping, the graph becomes more linear indicating charged impurity scattering is dominant even at high density. The minimum conductivity $σ_{min}$ broadens with increased doping, the V_g position is shifted to negative voltages, but the value of $σ_{min}$ remains approximately the same $\sim 4e^2/h$. All of these results are predicted by theory and provide proof that charged impurity scattering is dominant. The resulting changes in mobility of this experiment are contradictory to previous work [47]. This is explained by the low initial mobility of the graphene devices and the likely presence of both positively and negatively charged impurities.
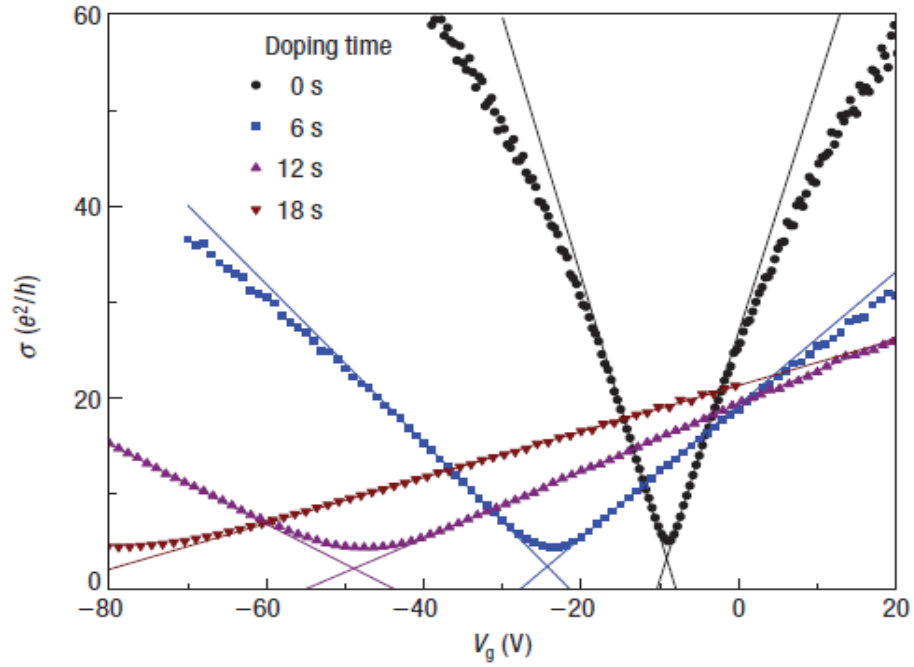
Fig. 2-17 Effect of K-doping on a pristine graphene sample. [48]

The potassium doping experiment was repeated, this time thermal annealing the sample to probe the influence on the electronic transport properties [50]. The K ions are expected to experience mutual Coulomb repulsion producing correlations in their positions. By varying the temperature from 20K to 180K and measuring $\sigma(n)$, the conductivity is observed to increase with increasing temperature, indicating an increase in mobility. For the largest K-doping concentration, the field effect mobility exhibited a fourfold increase. The plot of σ vs. n in Fig. 2-18 is fitted to the equation:

$$\sigma(n, n_K, T) = \left\{ \sigma_{pristine}(n)^{-1} + \rho_{ph}(T) + \rho_K[n, n_K, T] \right\}^{-1} \quad (8)$$

The conductivity of pristine graphene is given by σ_{pristine} and the increase in acoustic phonon scattering with temperature is taken into account by $\rho_{\text{ph}}(T)$. The resistivity due to the scattering by correlated K ions is given by $\rho_K(n, n_K, T)$ where the only free fitting parameters are K density n_K and the correlation length r_C [50]. Correlated charged impurities are known to be vital in realizing high mobilities in doped semiconductors [51 – 53] and the results are well understood theoretically [54].
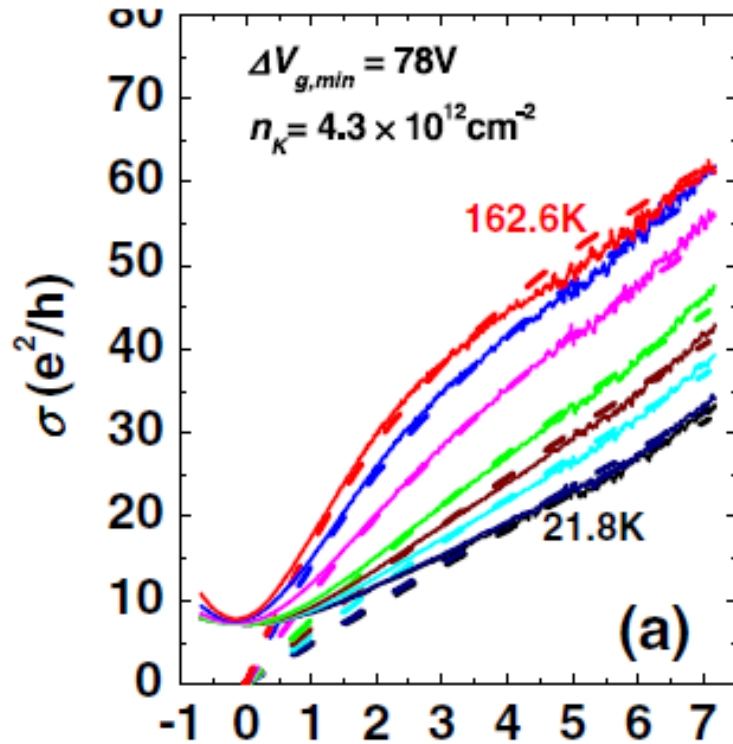
Fig. 2-18 Carrier density dependence of graphene conductivity at varying temperatures. T = 21.8K (black), 42.5, 100, 116.5, 130.1, 146.3, 156.6, 162.6K (red). The dashed lines are fits to Eq. (8) [50].

Similar results were obtained for gold nanoclusters on the surface of graphene [55]. Au was deposited at a cryogenic temperature of 18K. Due to the n-doping of the adatoms, the usual phenomena of shifted Dirac point, broadening of the conductivity minimum and decreases in mobility are observed for increased Au coverage. As the temperature is gradually increased to room temperature, the Dirac point shifts back toward zero and the mobility is recovered. Because such moderate temperatures do not provide enough thermal energy to evaporate Au, this effect is explained by the clustering of the adatoms. Theoretical work predicts that the formation of large, circular clusters will decrease the scattering cross section compared to point-like impurities [56]. The retention of the shape of the σ vs. V_g curve upon a second cool down indicates the irreversible nature of the clustering. AFM images confirm the presence of large, circular nanoclusters of gold at room temperature.
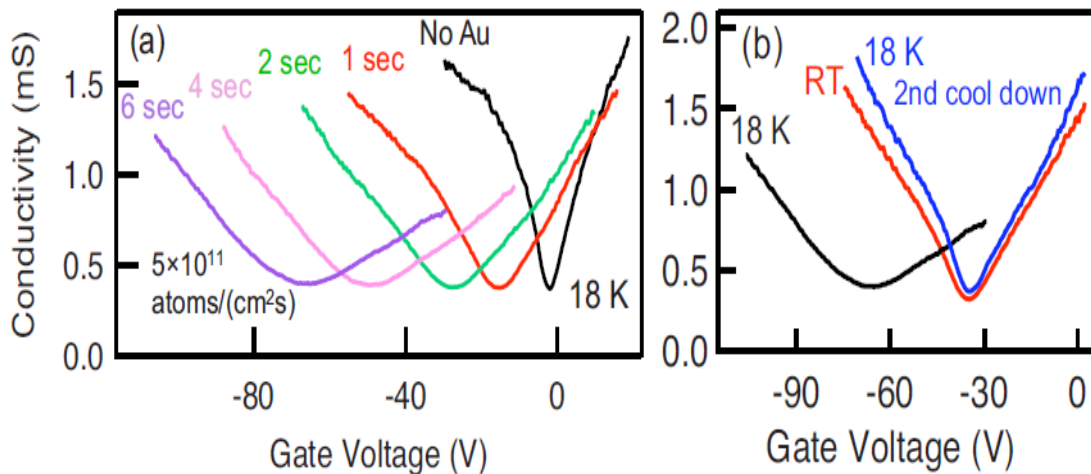
Fig. 2-19 (a) Gate dependent σ at increasing Au coverage. (b) Comparison of σ after Au deposition, heating to room temp. and after second cooling. [55]

2.5   Summary

Intrinsic (ripples, lattice defects) and extrinsic (charged impurities, electron-phonon coupling) scattering mechanisms in graphene have been explored. Pristine, as-prepared exfoliated graphene is expected to contain a low density of point defects. Phonon scattering can be affected by the substrate and surface roughness can alter the rippling. Additionally, placing graphene in varying dielectric environments can tune the transport properties by Coulomb screening. This will be discussed further.
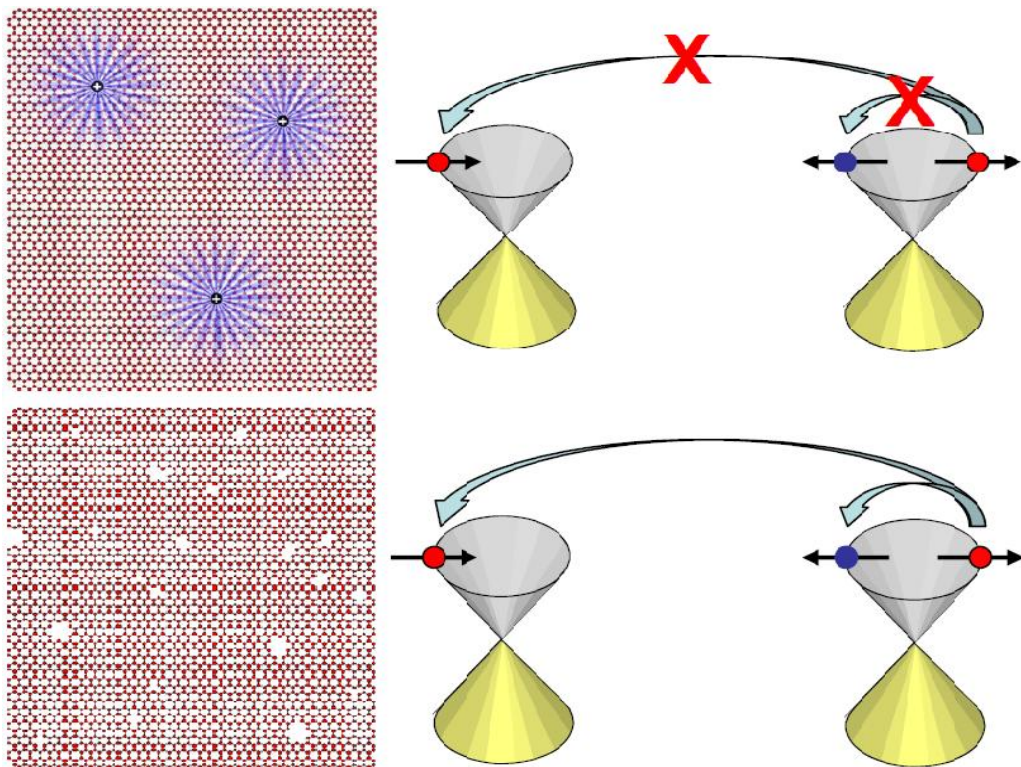
Fig. 2-20 Charged impurity and defect scattering in graphene. Backscattering and intervalley scattering is not allowed for long-ranged charged impurity scattering. Short-ranged scattering does allow for this [57].

Chapter 3
Graphene and High-κ Environments

Because graphene is a strictly two-dimensional material, the charge carriers are confined to a plane of atomic thickness. This fact has numerous ramifications to the electronic properties. We have discussed in the previous chapter how adatoms and other charged impurities can degrade the mobility. By changing the surrounding environment, the properties can be enormously tuned. Coulomb screening can be achieved by placing graphene on a substrate with a higher dielectric constant as well as more effective gating with higher capacitance. Atomically flat substrates can be used to decrease ripples and corrugations. Lattice matching to the honeycomb structure of graphene can also be achieved, as is the case with hexagonal boron nitride (hBN).

3.1   Tuning the Fine Structure Constant

The fine structure constant α was first introduced by Arnold Sommerfeld in 1916 [58]. It is a dimensionless number very nearly equal to:

$$\alpha = \frac{e^2}{4\pi\varepsilon_0 \hbar c} \approx \frac{1}{137.036} \qquad (1)$$

ε_0 is the permittivity of free space, c is the speed of light in a vacuum and $\hbar$ is Planck's constant over 2π. The constant was developed as a means to explain observed splitting of energy levels of the hydrogen atom. The relativistic variation of

the mass of an electron should be taken into account in determining the energy levels [59]. The Wigner-Seitz radius r_s takes the form of α and it is seen now as a coupling interaction term for the electromagnetic force which describes the relative strength of Coulomb interactions. It is the ratio between the graphene Coulomb potential energy and kinetic energy. For graphene, the fine structure term is written:

$$\alpha = \frac{e^2}{4\pi\kappa\varepsilon_0\hbar v_F} \qquad (2)$$

The speed of light c has been replaced by the Fermi velocity of graphene, $v_F \approx c/300$. This "fine structure constant" for graphene is independent of carrier density and mass, but it can still be tuned by substituting different dielectric media with different κ.
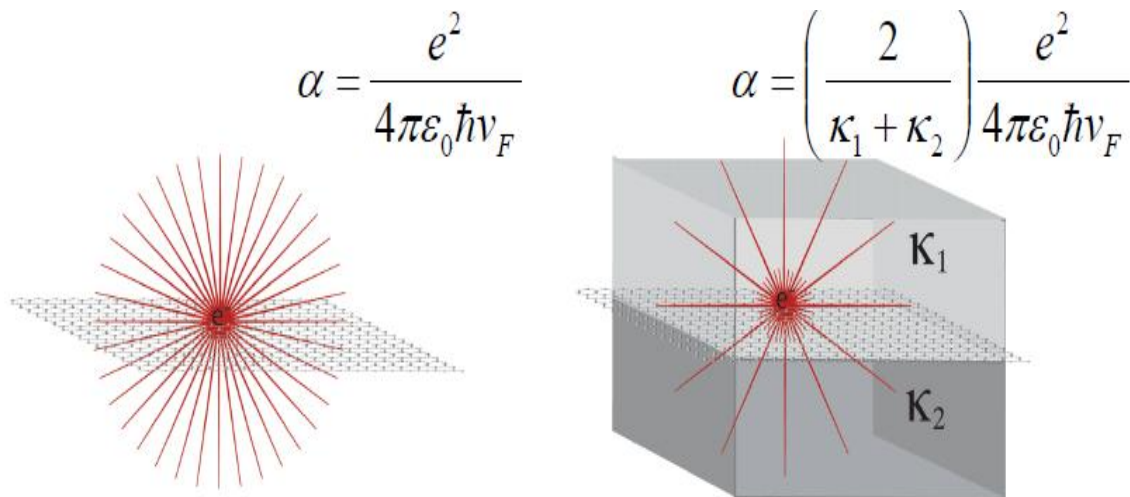
Fig. 3-1 Illustration of dielectric screening in graphene. Varying the dielectric environment controls the interaction strength parametrized by the coupling constant α [60].

3.2   Dielectric Media

Experiments have been carried out to observe the effect of submersing graphene devices in liquids with varying dielectric constants [61-65] and depositing dielectric materials on top of graphene [27, 60, 67]. Submersion in dielectric liquids will be discussed first.

Because the strength of charged impurities should depend on the dielectric environment, Leonid Ponomarenko of Andre Geim's group in Manchester researched the effect of covering graphene with glycerol ($\kappa \approx 45$) and ethanol ($\kappa \approx 25$). The mobility is expected to increase by over an order of magnitude. The addition of glycerol significantly improves the device characteristics (ρ vs. V_g is more symmetric, narrower peak is shifted more toward $0V_g$), but the typical change in μ as measured from the Hall effect did not exceed 30%. Covering with ethanol and deionized water yielded results that disagree with Coulomb scattering mechanism theory. Because of gate leakage problems, the voltage was applied directly to the ethanol/water so that liquid-gate voltage falls across a high capacitance double layer at the graphene-liquid interface. Minimal changes in μ are seen in the devices. An increase by a factor of 5 (20) should have been observed by covering with ethanol (water). This leads to the conclusion that charged impurity scattering is not the limiting factor for mobility enhancement in graphene [61].
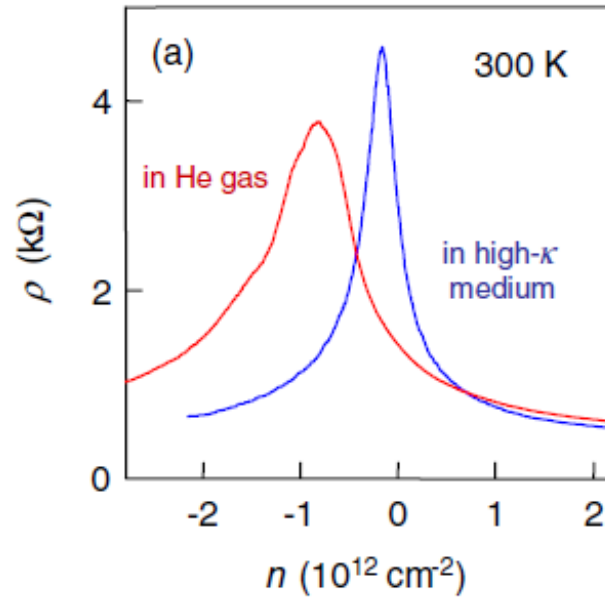
Fig. 3-2 Electronic properties of graphene covered with high-κ liquid glycerol.
Density varied by Si backgate. Change in peak position is not accompanied by 10-fold increase in μ [61].
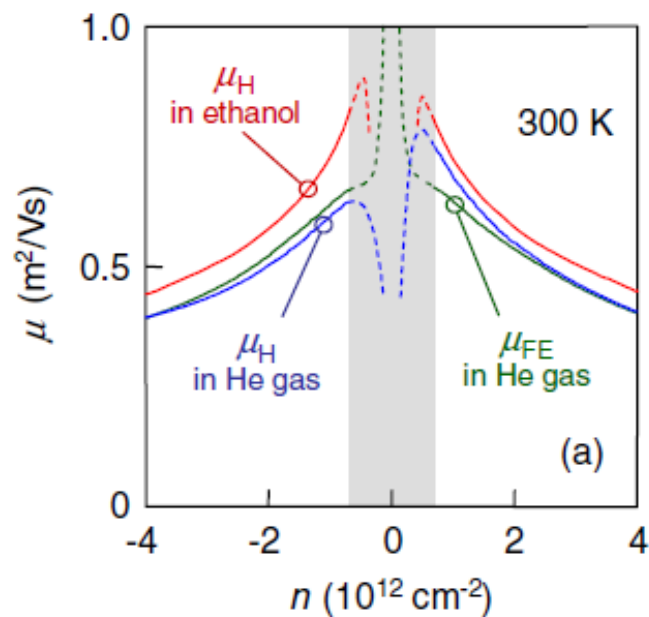
Fig. 3-3 Changes in μ induced by ethanol. [61]

The experiment was repeated by the Fuhrer group in Maryland, but with the use of a backgate [57]. Isopropanol (κ = 19.9) and DI water (κ = 80) were used as the covering liquids. Dramatic increases in carrier mobility were recorded with the addition of these high-κ liquids. Increases of 510% for isopropanol and 820% for DI water were observed. The difference in these two experiments is the use of a backgate as opposed to liquid gating. The gate charges in the electrolyte liquid are ions and behave as additional scatterers to limit the mobility. No additional scatterers are present for the Si backgate as illustrated in Fig. 3-5.
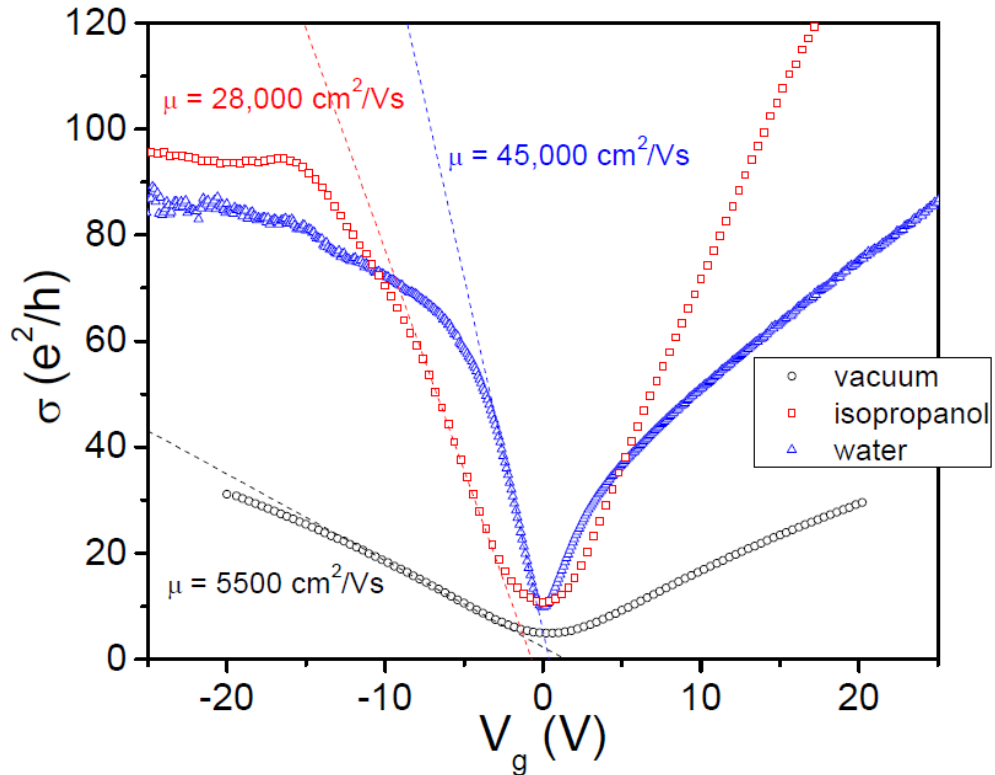
Fig. 3-4 Effect of high-κ liquids covering graphene device. Si backgate is used [57].
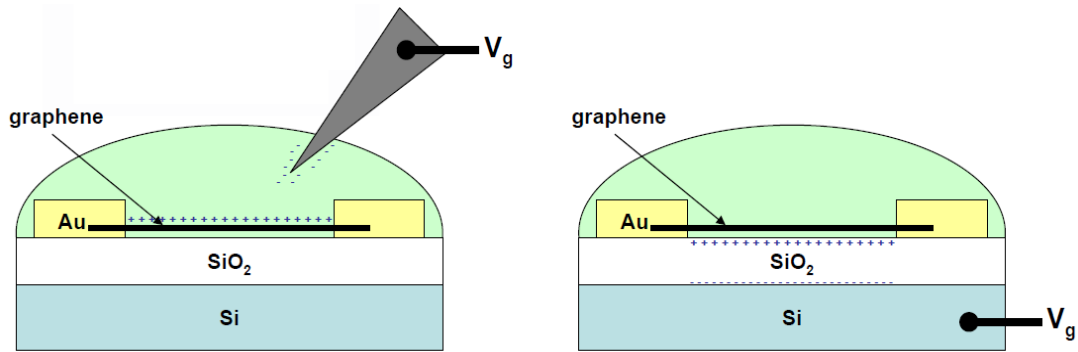
Fig. 3-5 Gating of graphene via liquid-gating and backgating with Si. [57]

Further work has been done with dielectric liquids. Covering a device with high-κ liquids increases the mobility dramatically up to ∼7 x 10^4 cm^2/Vs. As the dielectric constant increases further, the mobility remains nearly unchanged, indicating the approach of the intrinsic limit of room temperature mobility on SiO$_2$ substrates [62, 63]. These results are explained to be originating from Coulomb scattering from the charged impurities in SiO$_2$ and at the graphene/ SiO$_2$ interface.
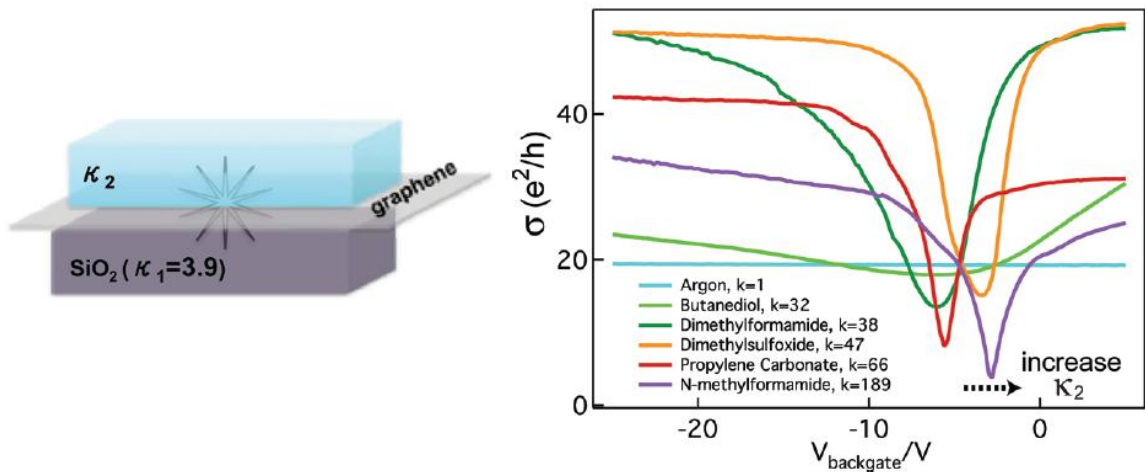
Fig. 3-6 Increase in mobility with increasing dielectric constant of covering liquids. [62]

Suspended graphene has been studied in liquids to surround both sides in a dielectric environment [64]. In addition, the manifestations of the charged impurities are only those adsorbed on the surface of graphene. Substrate induced scattering is effectively eliminated. Non-polar solvents hexane (κ = 1.9), toluene (κ = 2.3) and anisole (κ = 4.3) used to cover the graphene have exhibited increases in mobility proportional to the dielectric constant. This behavior is in qualitative agreement with Coulomb scattering [66] and previous experiments. In contrast, covering with polar solvents, although higher dielectric constant (isopropanol κ = 18, ethanol κ = 25, methanol κ = 33) results in a drop in mobility. This is confirmed by adding TBATPhB salt to non-polar anisole. The increase in concentration is inversely proportional to mobility. The addition of charged ions in the polar liquids contributes to scattering. This could also be a consequence of electrolyte gating since the backgate is in contact with the liquid.
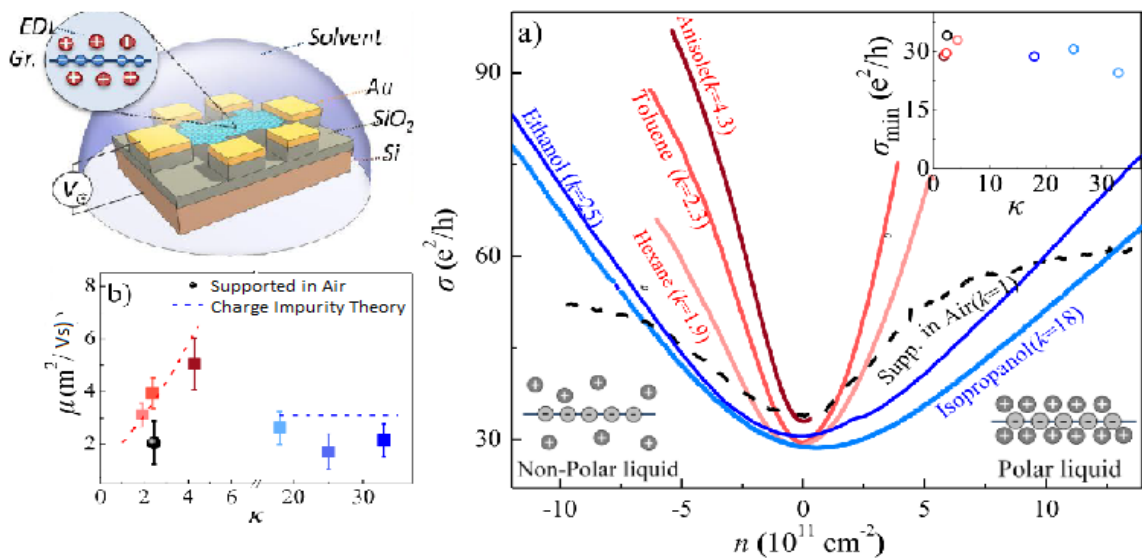
Fig. 3-7 Effect of dielectric liquids on mobility of suspended graphene. [64]

Depositing a top layer dielectric to graphene will also dramatically affect the electronic properties. Ice has been added to the top surface and interesting phenomena have been observed. The mobility of pristine graphene, which has an initial value of 9,000 cm^2/Vs, increases with added ice layers and saturates at 3 layers at 12,000 cm^2/Vs. However, the position of the conductivity minimum remains unchanged [60]. This is consistent with the Boltzmann transport theory including screening within the random phase approximation (RPA). The conductivity data is fitted to:

$$\sigma^{-1}(V_g, \alpha) = (ne\mu)^{-1} + (\sigma_s)^{-1} \quad (3)$$

$ne = c_g|V_g - V_{g,min}|$, e is the electric charge and $c_g = 1.15 \times 10^{-8}$ F/cm^2 is the gate capacitance per area for 300nm SiO_2. α is the charge coupling term in Eq. (2), calculated to be ≈ 0.81 for vacuum and ≈ 0.56 for ice layer on top.
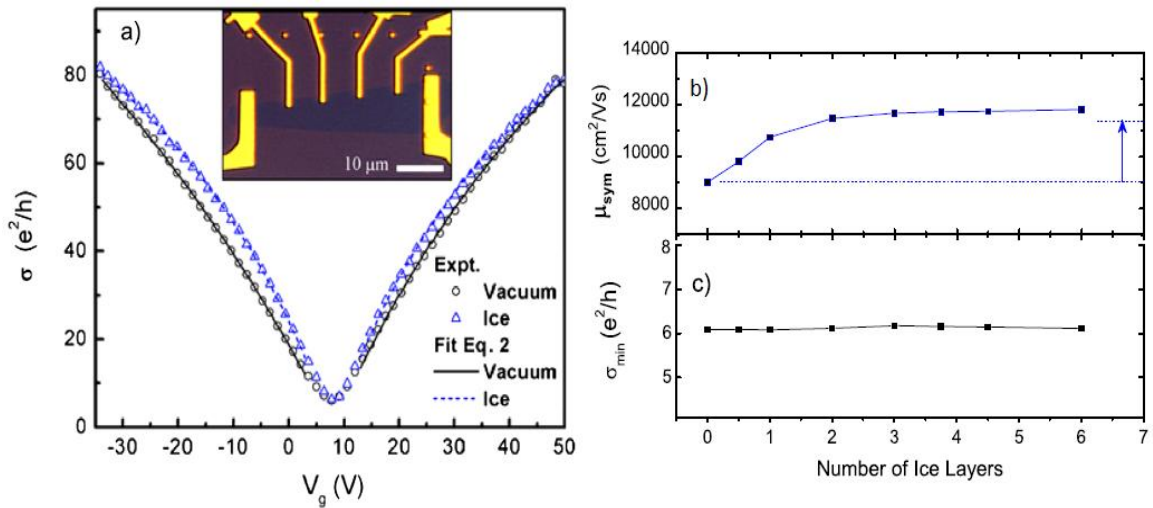
Fig. 3-8 σ vs. V_g for pristine graphene and with ice layer. Fit is to Eq. (3). Mobility saturates at 3 ice layers. σ_{min} remains unchanged [60].

3.3 The Role of the Substrate

We have discussed the role of dielectric top layers and covering liquids on the electronic properties of graphene. These were used with graphene still adhered to the SiO_2 substrate. Remarkable physics can be displayed when the underlying gate dielectric is changed completely.

Mica has been used as a substrate [61, 68] by first mechanically cleaving the crystallite on SiO_2, then depositing graphene further on top. It has been reported that for this substrate (and for bismuth strontium calcium copper oxide or BSCCO) the resistivity experiences a large hysteresis as a function of V_g [61]. The same effect is seen in our experiments which will be discussed in Chapter 6. The same typical mobilities are calculated from the Hall effect for devices on mica and on SiO_2. Graphene in contact with a freshly cleaved mica substrate is strongly hole-doped with carrier density of $\sim 9 \times 10^{12}$ cm^{-2}, resulting in permanent charge transfer [68].
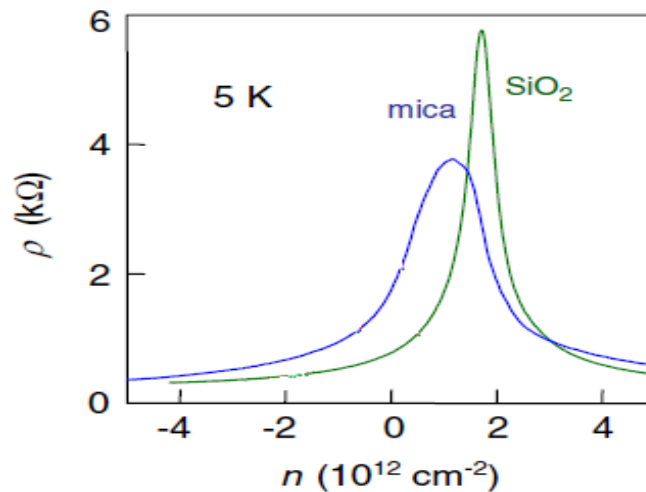
Fig. 3-9 Resistivity of graphene on mica. [61]

Another candidate substrate for graphene electronics is hexagonal boron nitride (hBN). High mobility devices have been fabricated from CVD grown graphene placed on hBN [69] and mechanically exfoliated graphene has been aligned and stamped onto an hBN flake [71]. This substrate is of particular interest because it is an insulator which couples weakly to the graphene, exhibits the highest mobility ever reported for graphene on any substrate, and strongly suppresses charge inhomogeneities due to the absence of dangling bonds or surface charge traps. These qualities are manifest due to the fact hBN is an isomorph of graphene with boron and nitrogen atoms occupying the inequivalent *A* and *B* sublattices in the Bernal structure and a lattice constant that is 1.8% longer. The ρ vs. V_g peak is extremely narrow and occurs at nearly $0V_g$. The width can be used to estimate the charge carrier inhomogeneity resulting from electron/hole puddles and is found to be a factor of 3 improvement over SiO_2 supported devices. The sublinear shape of σ vs. V_g is not a result of increased short-range scattering, but from a decrease in charged impurity scattering. Most remarkable is the enhancement in carrier mobility calculated from the Hall effect. The high density μ is ~$25,000 cm^2/Vs$ while the μ near the Dirac point is ~$140,000 cm^2/Vs$, the highest reported for substrate supported graphene.
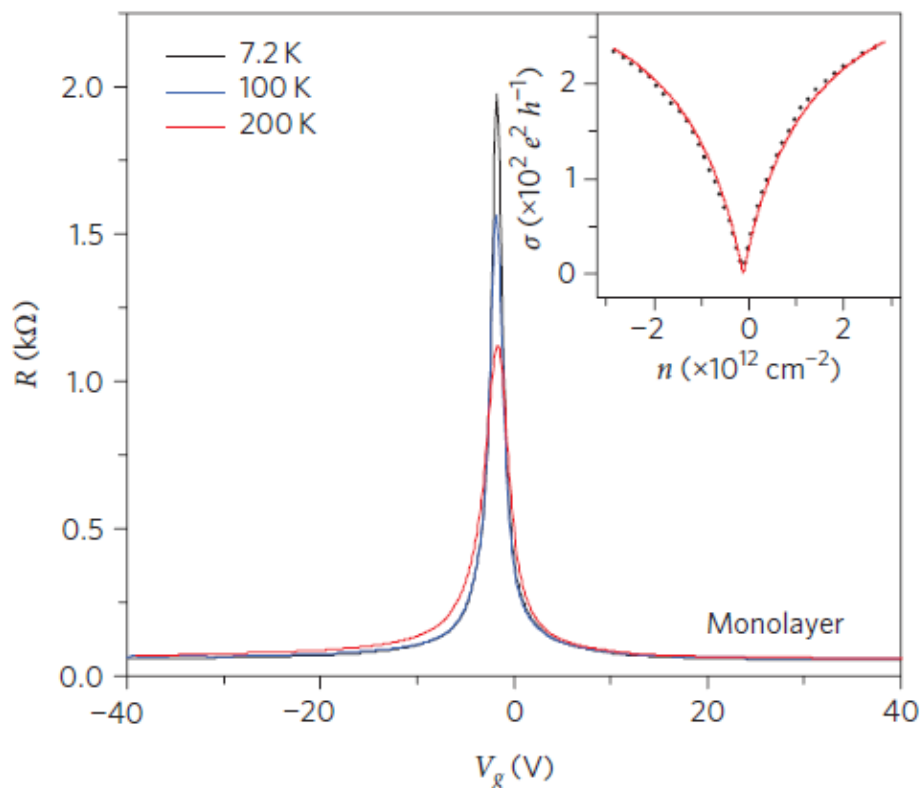
Fig. 3-10 Resistance vs. gate voltage for graphene on hBN. Inset is corresponding conductivity [71].

3.4   Summary

Much research has been done to probe the nature of charged impurity scattering in graphene. Experiments are in agreement with the theory that dielectric screening can be enhanced by changing the environment. The contradictory results can be explained by the addition of scatterers, either by electrolyte gating or polar solvents. Only a handful of substrates other than SiO_2 have been used to support graphene devices. In Chapter 5 I will present my device transfer method to place a device on any arbitrary substrate. The next chapter will focus on the substrate used in my research, strontium titanate.

Chapter 4
Strontium Titanate as a Substrate

Strontium titanate (chemical symbol: $SrTiO_3$) is referred to as STO. It is a

high-κ insulator that has extraordinary temperature dependent properties. It is an

intriguing material to use as a substrate. The characteristics of STO and the effect on

graphene electronic properties will be discussed in this chapter.

4.1   Strontium Titanate

At room temperature, STO is a cubic perovskite. It is paraelectric with

dielectric constant κ ≈ 200-300 and a wide band gap of ~3.2eV [72]. The highly

symmetric space group is *Pm3m* with a lattice parameter of *a_0* = 0.3905nm and a

density of $5.12g/cm^3$. As seen in Fig. 4-1, the Ti^{4+} ions at the center are coordinated

by six O^{2-} ions. Each of the Sr^{2+} ions located at the corners of the cube is coordinated

by twelve O^{2-} ions and is surrounded by four TiO_6 octahedra. Covalent bonding takes

place between the hybridized O-*2p* states and the Ti-*3d* states while Sr^{2+} and O^{2-}

exhibit ionic bonding [73]. For any planar direction (*h k l*), there are always two

possible, distinct terminating surfaces. For instance, STO (100) can have and SrO or

TiO_2 terminating surfaces. The differing terminating surfaces for each plane is

illustrated in Fig. 4-2.
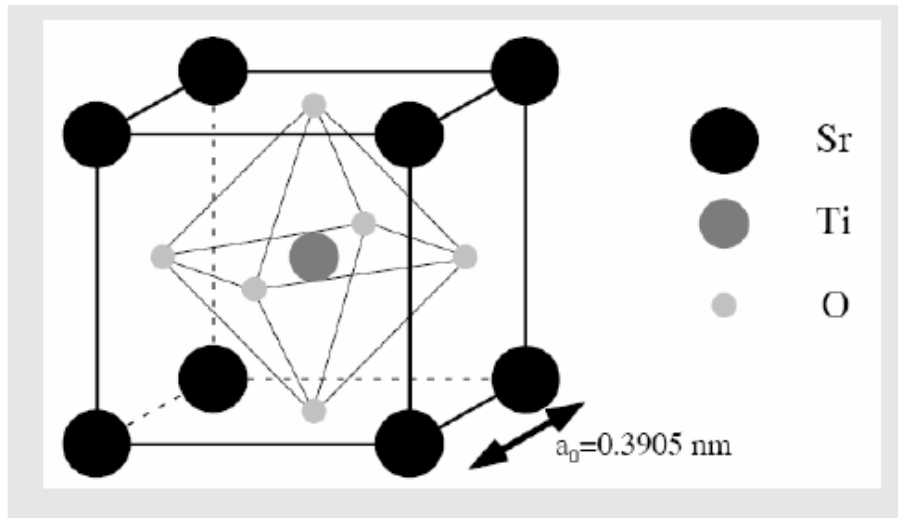
Fig. 4-1Cubic perovskite structure of STO. [73]
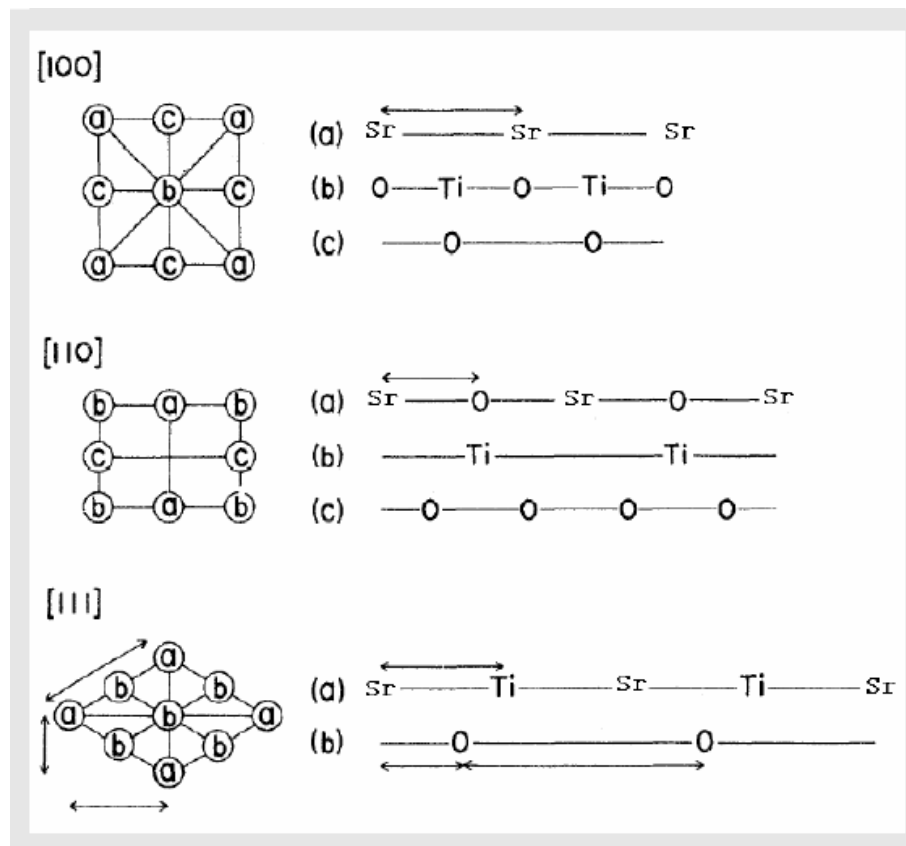
Fig. 4-2 Atomic arrangements for planar terminating surfaces of STO. [73]

Goldschmidt's tolerance factor, first described by Victor Moritz Goldschmidt in 1924, can be used to assess the distortion and stability of perovskites [74]. The tolerance factor is represented by t:

$$t = \frac{r_A + r_0}{\sqrt{2}(r_B + r_0)} \qquad (1)$$

r_A is the radius of the A-cation (Sr), r_B is the radius of the B-cation (Ti) and r_0 is the radius of the anion (O). For STO, r_{Sr} = 1.44Å, r_{Ti} = 0.605Å, and r_O = 1.40Å. The tolerance factor is t = 1 meaning the ion packing is ideal for a perovskite structure. Larger and smaller values of t for other titanate perovskites, such as $BaTiO_3$ (t = 1.062) and $CaTiO_3$ (t = 0.82) favor ferroelectricity and quantum paraelectricity respectively. However the symmetry can vary with temperature. Cubic STO at RT can transition to tetragonal ($a = b \neq c$, space group *I4/mcm*) between 110K – 65K, orthorhombic between 55K – 35K and the symmetry is unclear below 10K. X-ray diffraction evidence suggests a rhombohedral structure [75]. This change in symmetry would shift the packing of ions and change the tolerance factor. This can account for the piezoelectric [76] and ferroelectric phase transitions [77, 78] and the increase in dielectric constant [79, 80] at low temperature. We are most interested in the increase in κ with decreasing temperature. The dielectric constant can rise to between 5,000 and 10,000 at cryogenic temperatures as seen in Fig. 4-3.
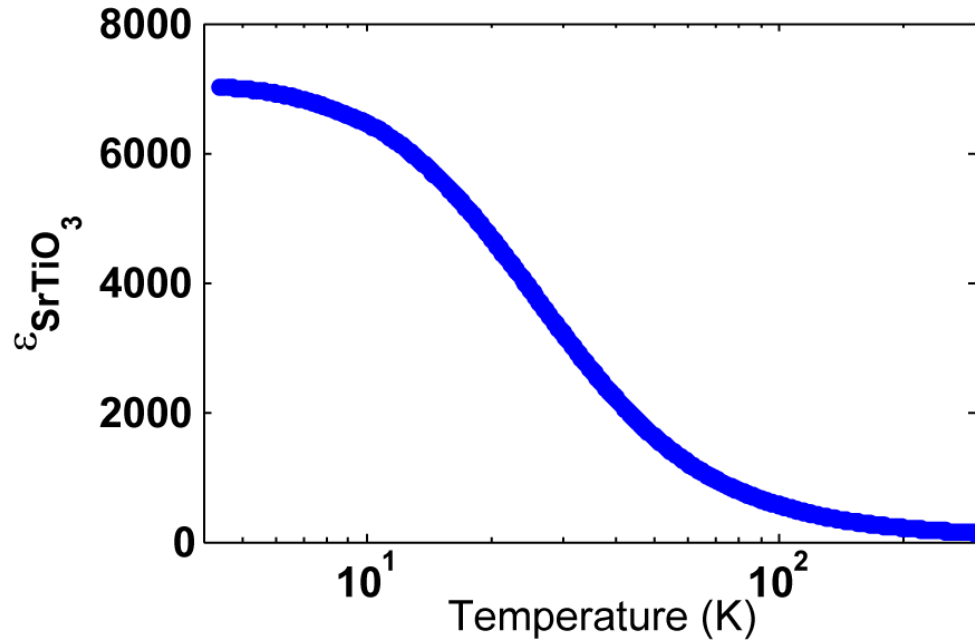
Fig. 4-3 Increase of dielectric constant of STO with decreasing temperature.
[80]

4.2 Local Effects of Graphene on STO

Graphene exfoliated onto STO has been studied by various local scanning

probe techniques. Kelvin probe force microscopy (KPFM) can be used for

investigating electronic properties of low-dimensional systems [81]. It can provide

information on the absolute value of the work functions of surfaces. KPFM studies

have determined the work function of mechanically polished STO(100) to be Φ_{STO} =

3.979 ± 0.058eV, slightly lower than found in literature for bulk. It is mostly likely

TiO_2 terminated with areas of SrO terminated. The contact potential difference for

single layer graphene on STO is Φ_{SLG} = 4.409 ± 0.039eV and increases monotonically

with increasing layers until saturation at five layers. When graphene is placed on a

substrate, charge transfer can occur. The material with the lower work function will

transfer electrons to the material with higher work function. Graphene is

intrinsically n-doped by the STO [81].
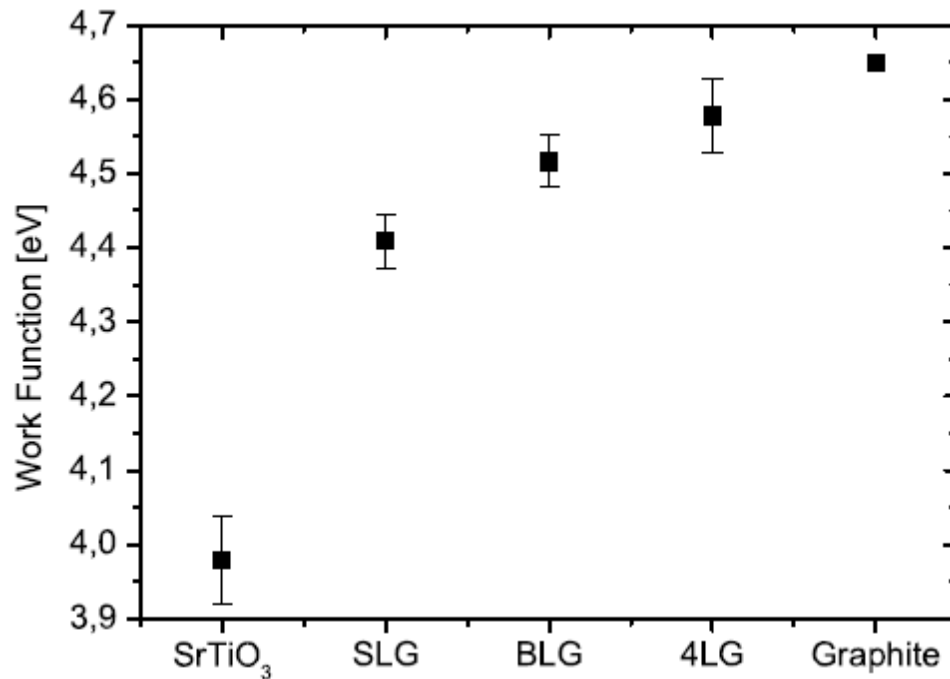
Fig. 4-4 Work function of graphene increases with added layers. Saturation
occurs at 5 layers [81].

Capacitance is an important fundamental electronic property of a material.

However, low-dimensional systems have a finite density of states and are unable to

accumulate enough charges to completely screen an external field. Under these

circumstances, a two-dimensional electron gas (2DEG) manifests itself as a

capacitor. This is called its quantum capacitance, C_q, and was first introduced by

Serge Luryi in 1987 [82]. In conventional 2D systems, the C_q is constant and comparatively small, but with a unique Dirac-type band structure of low energy massless fermions, C_q of graphene is proportional to the Fermi level and variable with different dielectric substrates. C_q has been measured as a function of the Fermi energy on SiO₂ and STO via Scanning Capacitance Spectroscopy (SCS) [83]. The relation of C_q to E_F is defined as:

$$C_q(E_F) = \frac{A_{eff}e^2}{\sqrt{2\pi^2}\hbar^2 v_F^2 f(N)} E_F \qquad (2)$$

$f(N)$ is a function of the ratio of the effective area A_{eff} and the area of the probe tip. C_q is substantially higher for graphene deposited on STO which is predominantly due to the increase in the effectively biased area caused by the enhanced dielectric screening of the high-κ substrate.
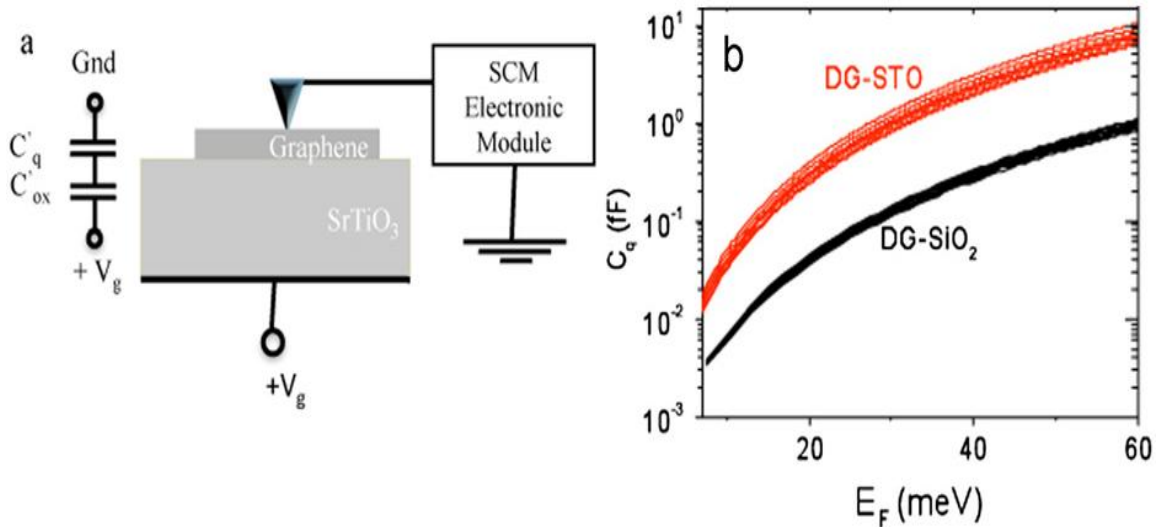
Fig. 4-5 Quantum capacitance of graphene on STO. Schematic of graphene measured by SCS (a) and C_q vs. E_F exhibiting increase in graphene on STO (b) [83].

Scanning Capacitance Spectroscopy has also been used to observe correlations between electron mean free path ℓ and charged impurity density n_{CI}. There is a clear correlation in the SCS mapping between the minima in ℓ and maxima in n_{CI} for graphene on SiO_2 and SiC, both of which have a relatively low κ. For the high-κ STO(100), ℓ and n_{CI} are uncorrelated, indicating a very effective screening of the charged impurities. Fig. 4-6 illustrates the positions of maxima (yellow) and minima (red) in the ℓ maps. Opposite results are observed for the correlations between ℓ and resonant scatterer density n_{RS} indicating that resonant scatterers are dominant in graphene on STO [84].
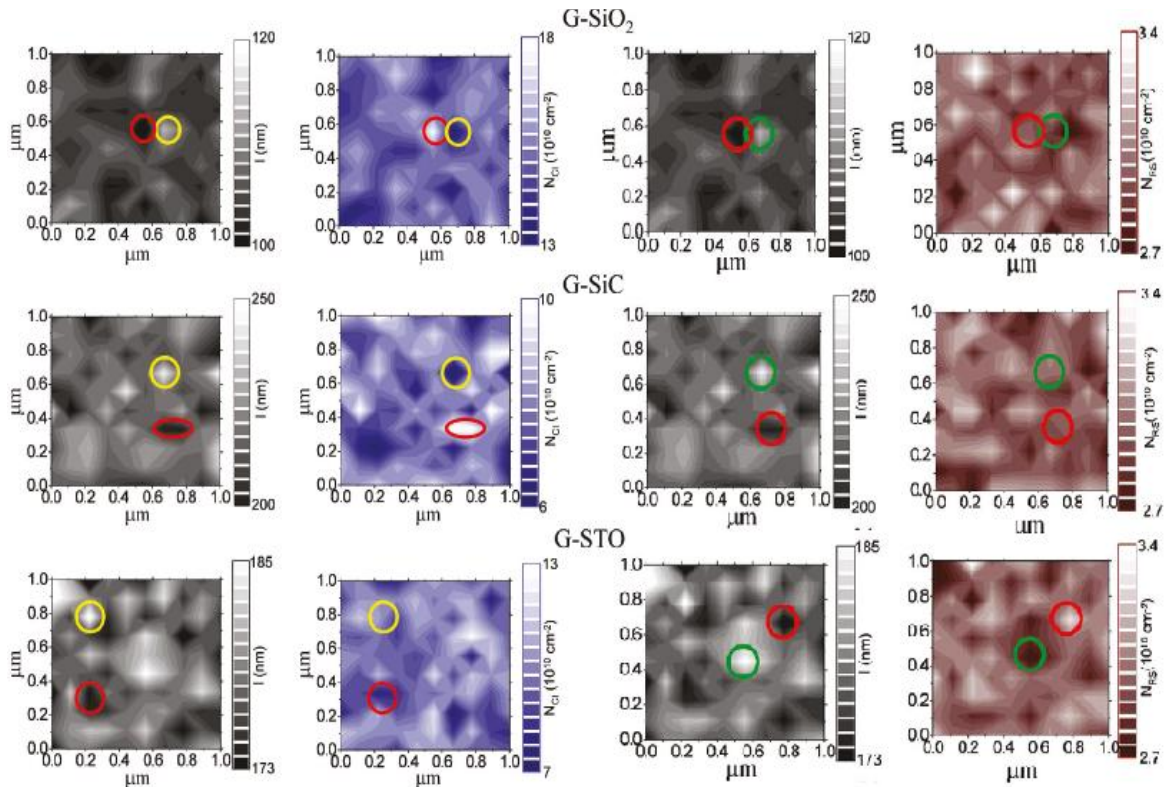
Fig. 4-6 Mapping correlations between ℓ and n_{CI}/n_{RS} for graphene on SiO_2, SiC, and STO. (Left) ℓ-map (gray) and n_{CI}-map (blue). (Right) ℓ-map and n_{RS}-map (red) [84].

4.3 Electron Transport Properties of Graphene on STO

Earlier research has been performed with single-wall carbon nanotubes (SWNT) grown by chemical vapor deposition on 20nm of STO that showed enhanced transconductance [85]. Graphene nanoribbons (GNR) were also fabricated on STO from exfoliated graphene followed by dip-pen nanolithography and O_2 plasma etching [86]. These devices showed high mobilities and low operating voltages due to the high κ and atomic flatness. Experimental research done by Alberto Morpurgo's group at University of Geneva in Switzerland is most relevant to our work [80]. Hall bar devices were fabricated from graphene exfoliated directly onto the surface of 500µm thick STO followed by electron beam lithography and metal electrode deposition. Measuring 10 devices, the range of mobilities is between 3,000 and 10,000 cm^2/Vs, the same range as similar devices on SiO_2 substrates. The most intriguing aspect of this work is the insensitivity of the transport to temperature below 50K. The dielectric constant is clearly increasing as expected at low T. The gate dependant resistance peak narrows with decreasing temperature as a smaller V_g range is needed, indicating a higher capacitance (see Fig. 4-7a). The carrier density (calculated from the Hall voltage $n = B/e R_{xy}$) also increases by an order of magnitude from 50K to 250mK (see Fig. 4-7b). But the resistivity as a function of carrier density overlaps nearly perfectly for all temperatures in this range (see Fig. 4-8a). This result is also what is normally found for devices on SiO_2 [98].
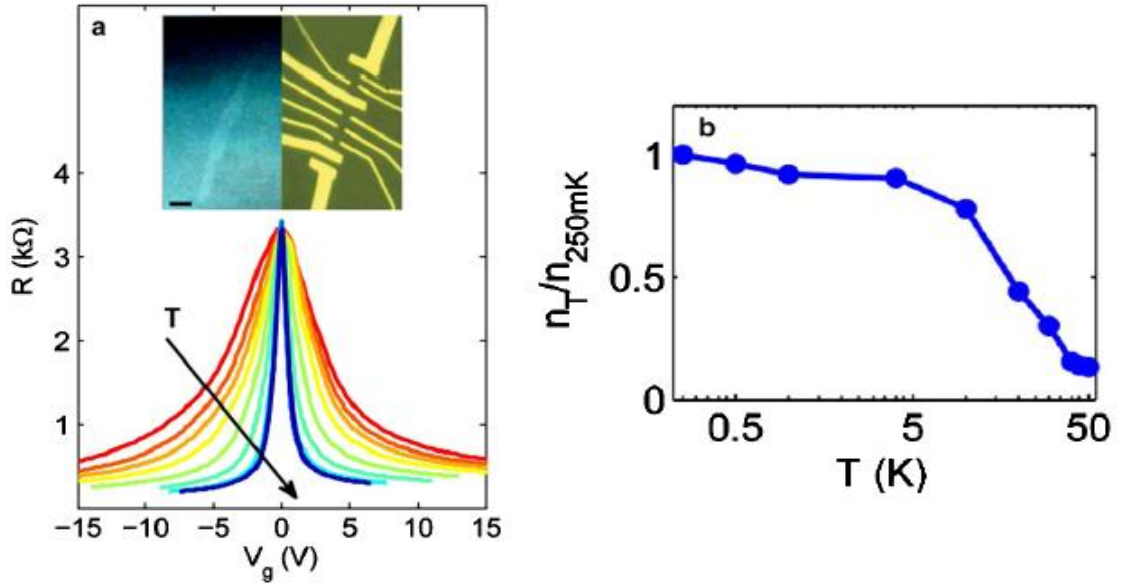
Fig. 4-7 Temperature dependence of graphene exfoliated on STO. (a) Sheet resistance vs. T shows narrowing Dirac point. Dark-field image of flake and optical image of graphene Hall bar device (inset). (b) Carrier density increases by one order of magnitude from 50K to 250mK as expected [80].
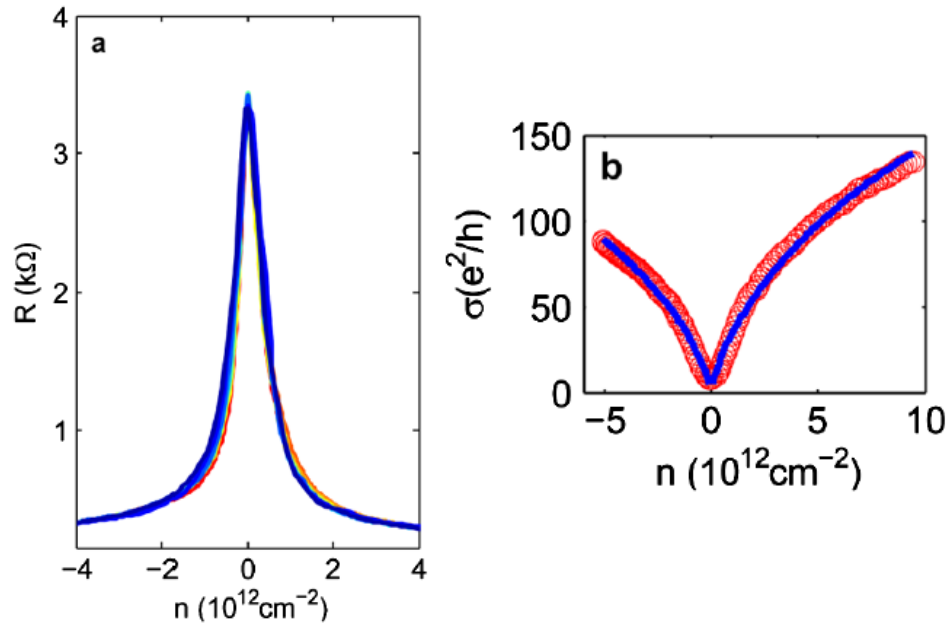
Fig. 4-8 Temperature independence of sheet resistance and conductivity vs. carrier density for graphene exfoliated on STO. [80]

It is concluded from this that the large dielectric constant of STO does not affect transport through graphene at low magnetic fields. Long-range charged impurity scattering is ruled out by the Morpurgo group as the dominant mechanism. Their results are explained by resonant scattering of short-range potentials expressed by the following:

$$\sigma_i = \frac{2e^2}{\pi h} \frac{n}{n_i} ln^2(\sqrt{n\pi}R) \qquad (3)$$

R is the potential range and n_i is the impurity concentration. The blue line in Fig. 4-8 is a fit to Eq. (3). This provides an appropriate fit away from the Dirac point. The values for the parameters n_i = 2.9 x 10^{11} cm^{-2} and the short range of R = 0.22nm are obtained from the fit and match closely to values for graphene on SiO_2 [38].

It is reasonable to conclude that a layer of water or other adsorbed molecules may be between graphene and STO to decouple the two materials. However, high magnetic field measurements conclude that the N = 0 Landau level in the R_{xx} vs. V_g curve decreases by an order of magnitude as temperature decreases from 50K to 250mK (curve not shown). This is contrary to graphene on SiO_2. It is well known that electron-electron interactions play an important role in determining the properties of the N = 0 Landau level in graphene. This signifies the effectiveness of screening by the substrate.

Graphene transport properties on STO have been studied theoretically in the context of contributions of competing scattering mechanisms [87]. It is indeed

possible that the conductivity is density dependent. In particular, the low density

regime is likely dominated by long-range Coulomb disorder for graphene on STO or

any substrate for that matter. The resonant scattering model {$\sigma \sim (n/n_i)$

$\ln^2(\sqrt{n/n_0})$}, presented by the Morpurgo group cannot qualitatively account for the

existence of the low density minimum of conductivity. There is also no physical

evidence for the existence of resonant scatterers other than providing an

intermediate density fit. In addition to the unaccounted Dirac region, the possibility

that the substrate impurity density is dependent on temperature cannot be ruled

out. A theoretical fit using a dual model associating Coulomb and resonant

scatterers and assuming that the charged impurity density is inversely proportional

to temperature can well explain the experimental data. The four scattering

mechanisms contributing to the resistivity that are considered are {A} charged

impurities ρ_{imp}, {B} short-range impurities ρ_{sd}, {C} correlated long-range charged

impurities ρ_C, and {D} resonant defects ρ_i. They are defined as:

{A}   Charged impurity: $\dfrac{1}{\rho_{imp}} = \sigma_{imp} = \dfrac{e^2}{h}\dfrac{n}{2n_{imp}\alpha^2 G_1(\alpha)}$ (4)

n_{imp} is the charged impurity density, $\alpha = e^2/\hbar v_F \kappa$ is the fine structure constant for

graphene, and:

$$G_1(x) = \frac{\pi}{4} + 6x - 6x^2 + 4x(6x^2 - 1)g(x) \qquad (5)$$

$$\text{with } g(x) = sech^{-1} \frac{2x}{\sqrt{1-4x^2}} \quad \text{for x < ½}$$

$$(6)$$

$$g(x) = sec^{-1} \frac{2x}{\sqrt{4x^2-1}} \quad \text{for x > ½}$$

{B}   Short-range impurity: $\dfrac{1}{\rho_{sd}} = \sigma_{sd} = \dfrac{8e^2}{h} \dfrac{(\hbar v_F)^2}{n_{sd} V_0^2}$ (7)

n_{sd} is the 2D short-range impurity density and V_0 is a constant short-range potential (δ-function in real space).

{C}   Correlated impurities: $\dfrac{1}{\rho_C} = \sigma_C = \dfrac{e^2}{h} \dfrac{n}{2n_{imp} \alpha^2 G_1(\alpha)} \dfrac{1}{1-a+Ba^2 (n/n_{imp})}$ (8)

$$a = \pi\, n_{imp} \alpha^2 \qquad (9)$$

$$B = \frac{G_2(\alpha)}{2G_1(\alpha)} \qquad (10)$$

$$G_2(y) = \frac{\pi}{16} - \frac{4y}{3} + 3\pi y^2 + 40y^3 \left[1 - \pi y + \frac{4}{5}(5y^2 - 1)\right] g(y) \qquad (11)$$

The contribution from resonant scatterers {D} is given in Eq. (3). It is clear that it is long-range Coulomb disorder that dominates at low density since the corresponding scattering rate is asymptotically the largest in the limit of vanishing density and it is essential to explain the low-density minimum of conductivity. The above formulas are calculated for homogeneous systems. For the inhomogeneous region at low density, a Gaussian form of potential fluctuation is assumed. The effective medium

theory of conductance with a binary mixture (electron/hole puddles) is applied and is parametrized by "*s*". This dual model explains the temperature independent conductivity of graphene on STO well in the entire range of carrier density as illustrated in Fig. 4-9. The dashed line is plotted for T = 50K with κ = 500 and corresponding impurity density induced in the substrate n_{imp} = 2 x 10^{13} cm^{-2}. The solid line is plotted at a lower T = 250mK with κ = 3500 and n_{imp} = 3 x 10^{14} cm^{-2}. The red dots are experimental data points extracted from Morpurgo group's paper.
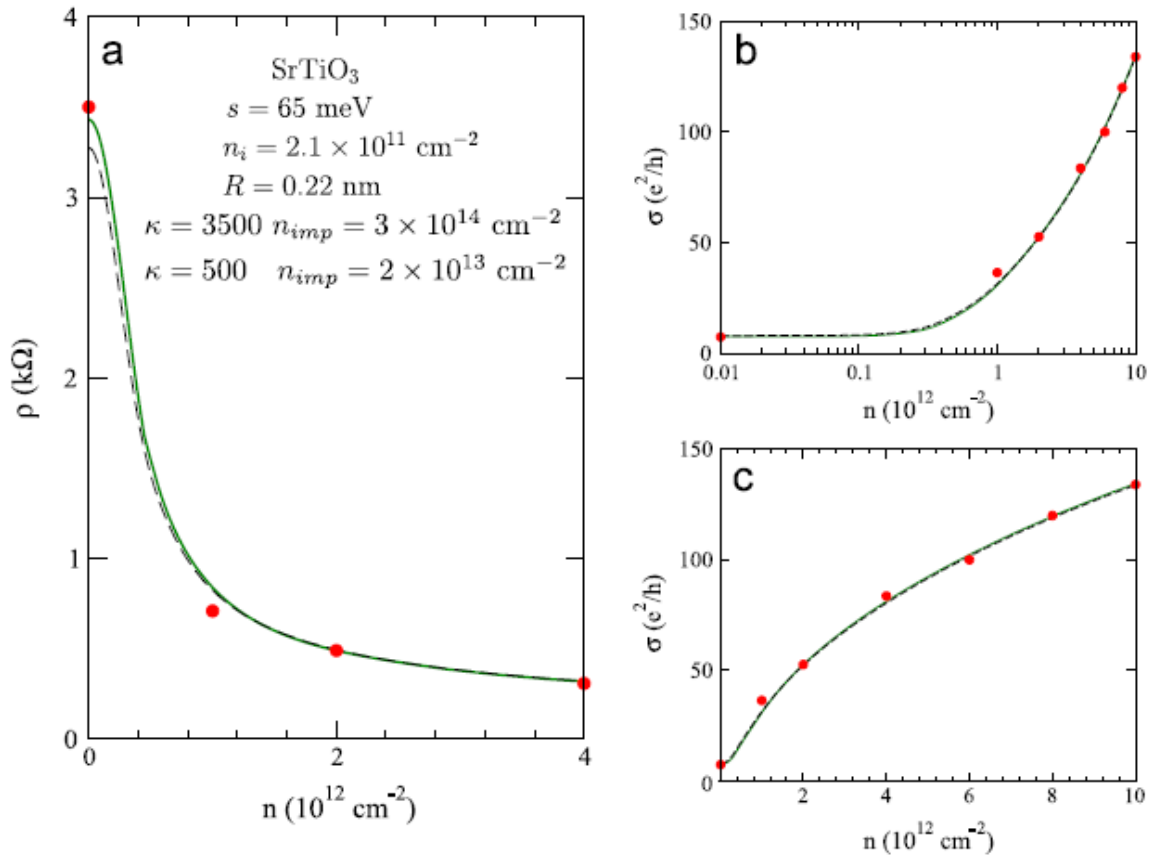
Fig. 4-9 Dual scattering model fit for graphene transport properties on STO. Details given in the text [87].

It is beneficial to determine the experimental contribution of the scattering

mechanisms in graphene on STO. Another drawback to the Morpurgo experiment is

that the exfoliated graphene devices studied can only be compared to similar

devices fabricated on SiO_2 substrates. It is advantageous to be able to study the same

device on SiO_2 and STO so a direct comparison of the transport properties can be

examined. The methods used and techniques developed for achieving these goals

are discussed in the next chapter.

Chapter 5
Experimental Methods

As a preface to this chapter, I would like to take the time to offer advice to aspiring experimentalists who may be reading this. Complacency is your greatest enemy. It takes time to develop and practice the methods to make and measure devices. Once you have become an expert at it though, it is easy for it to become second nature. You may only need to go through the motions without having to think too deeply about each step. This is a critical error. Time must be taken to ensure everything you do is deliberate. By concentrating and making sure each step is done right the first time, every time, careless mistakes can be avoided. This prevents you from having to start over from scratch which can cost you weeks of time. These mistakes are the biggest timewasters you will encounter, even more so than reading sports news on the internet.

5.1   Exfoliation of Graphene

Graphene can be obtained using a few different methods. Thermal decomposition of SiC can bring graphene to the surface [88]. Chemical Vapor Deposition (CVD) growth of graphene on transition metals such as copper, nickel, and platinum using methane gas [89-91] is another method, one I have also tried. The method used in my experiments is mechanical exfoliation developed by Konstantin Novoselov and Andre Geim in 2004 [1].

Before the graphene can be attained, the substrates must be prepared. Doped Si wafers (5 x 5mm) with 300nm of thermally grown SiO_2 are thoroughly cleaned. The chips are first soaked in a beaker of acetone on a hotplate at 65°C. The chips are then transferred to a beaker of isopropyl alcohol (IPA), then to deionized water (DI water), followed by a H_2O_2 solution and finally DI water again. Each step is for a 10 minute soak. The temperature for each is ambient except for the first step. It is not necessary that an ultrasonic cleaner is used to prepare the chips. I do not use one as it is possible that microscopic cracks can appear in the surface of the SiO_2 which can lead to dielectric breakdown and large leakage currents when the backgate is applied. Once the substrates are removed from the DI water they can be dried with nitrogen gas and they are ready for graphene exfoliation.

The graphite used is Kish graphite. Two pieces of Scotch tape ≈ 3" are placed adhesive side up and taped to a table top or other flat surface. I use a 4" x 2.5" x 0.75" aluminum block. Place a piece of Kish graphite on one of the tape pieces. Take another strip of Scotch tape about 6" long, fold it over 0.5" at the edges, place it on top of the graphite and repeatedly peel it until flakes of graphite cover the entirety of both tape pieces. Place a Si wafer on the other piece of tape. Using a diamond-tipped wafer scribe, make a small scratch (> 1mm) in the top right corner of the wafer. This will be used later when writing alignment marks. Another piece of tape about 6" long is rubbed onto the tape with graphite. Peel the tape away and then stick it to itself repeatedly until the graphite is nearly transparent.
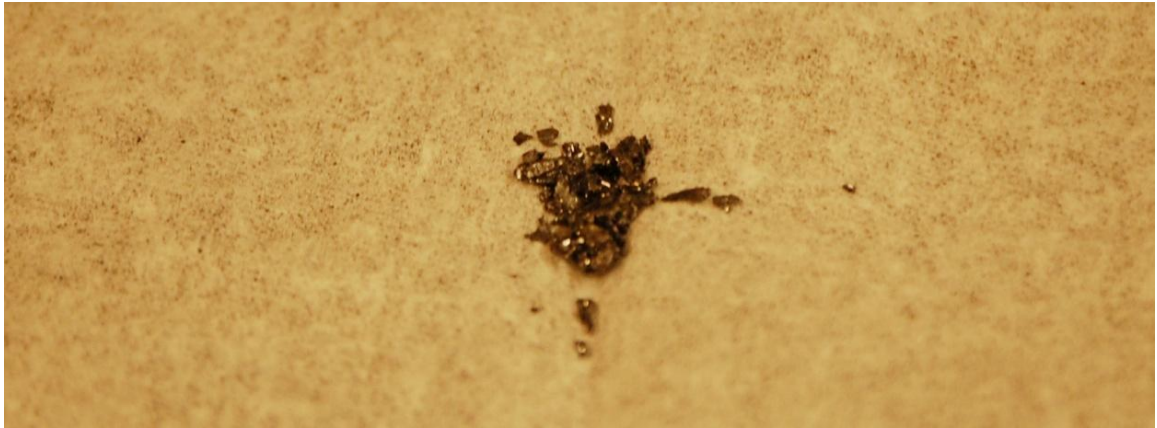
Fig. 5-1 Image of Kish graphite.
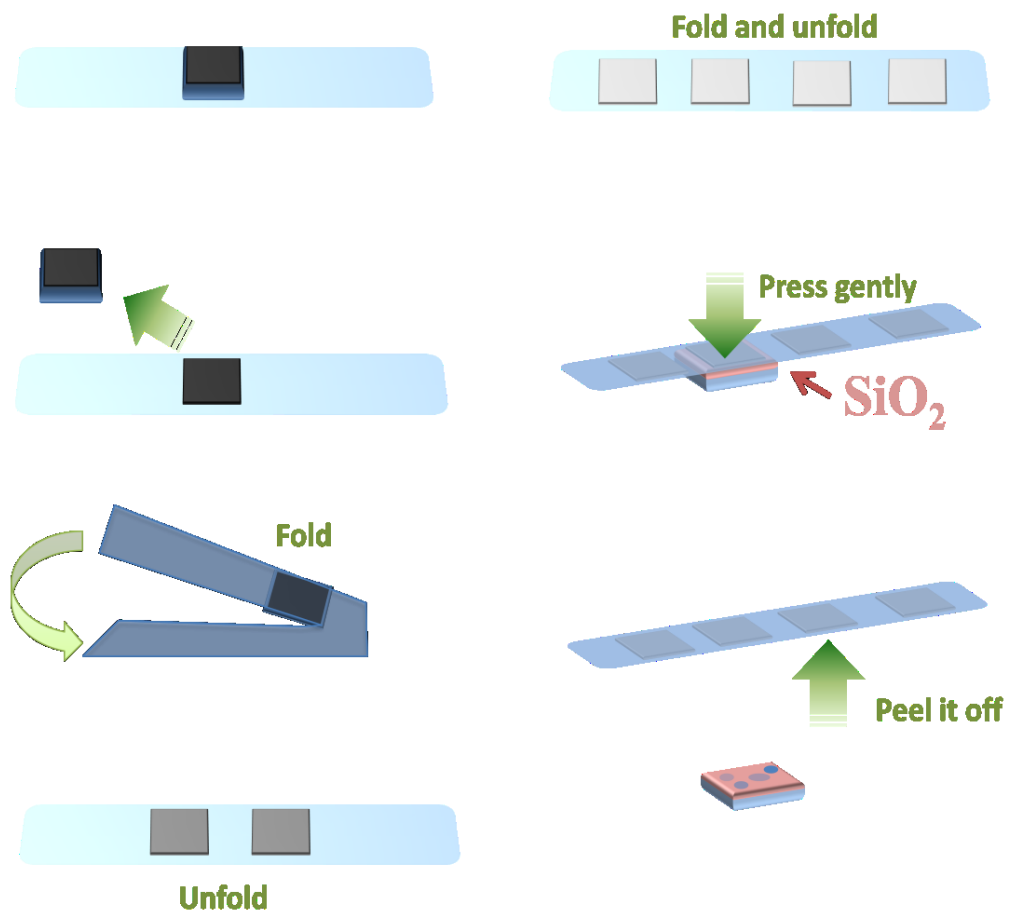
Fig. 5-2 Mechanical exfoliation of graphene.

Place the tape graphite side down on top of the Si wafer. Wrap the butt end of tweezers with electrical tape and rub this soft end gently across the Si wafer and tape for 30 seconds. Very slowly and evenly peel the tape back. It should take about a minute to remove the tape from the wafer. A razor blade can be used to remove the wafer from the Scotch tape it is stuck to. Graphene has now been exfoliated.

Locating the single layer graphene is the next step. A layer of SiO_2 that is 300nm thick is essential and was in fact a key component to the discovery of graphene. Due to optical interference with the SiO_2 layer, a color contrast can be seen in single layer graphene [4]. The number of layers can be distinguished with an optical microscope based on subtle variations in contrast (see Fig. 5-3). It takes a little experience and a lot of patience to locate usable flakes to pattern with electron beam lithography (EBL). A usable flake has dimensions no less than an area approximately 10 x 5µm, but the larger the better. The numbers of graphene layers can also be verified by Raman spectroscopy with a 532nm laser [92]. Draw a to-scale picture of the wafer with the locations of each useable flake so that the writing of alignment marks will be precise. Make sure you include the position of the scratch mark so you know the orientation of the chip relative to the flakes. Because of the time consuming and boring nature of this step, locating the graphene is the most tedious part of the experiment. It's best to have an undergrad do it.
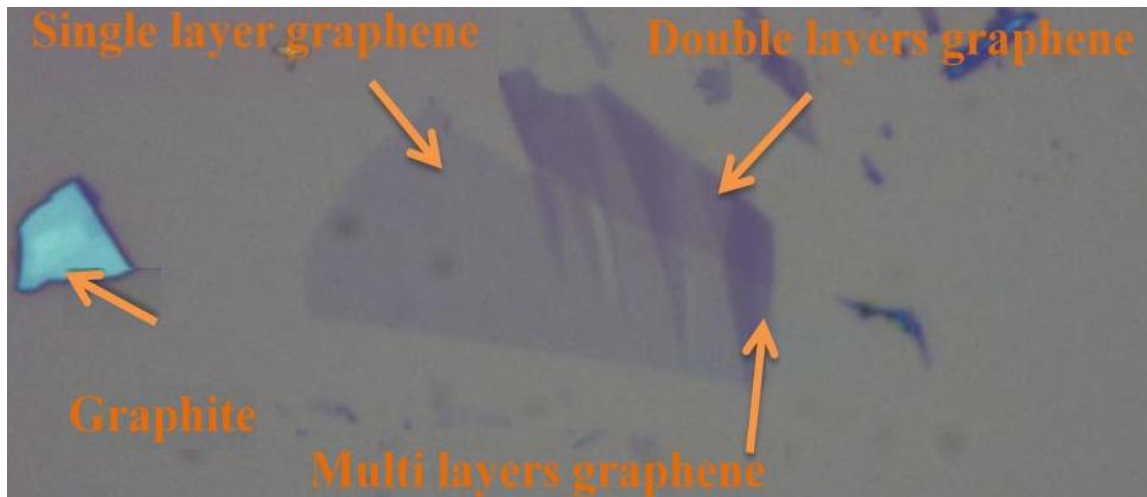
Fig. 5-3 Optical microscope image of single-, double-, and multilayer graphene and bulk graphite.

5.2 Electron Beam Lithography

EBL is now used to draw nanoscale patterns for electrodes on the graphene flake. First the chip is spin-coated with two layers of e-beam resist, one layer of methyl methacrylate (MMA) and one layer of polymethyl methacrylate (PMMA). Each layer is spun for 3200 rpm for 45 seconds with a 10 minute hard bake at 170°C on a hotplate after each coating. The total thickness of the two layers is about 500nm. The electron beam exposure is done in the SEM chamber using the NPGS software to control the beam. A voltage of 20kV is used with differing apertures depending on the feature size you want to draw. For small features (<50μm) the 20μm aperture is used to get good resolution and crisp, sharp features. The measured beam current can decrease slowly over time and after maintenance, so you may want to do a dose test if you haven't done EBL for some time. Asking the

previous user for the doses used is an easy solution. For a beam current of 90pA, the area dose is 500µC/cm². For larger features that don't need a high resolution, the 120µm aperture is used so the exposure will not take too long. The area dose is increased to 3600µC/cm².

A mixture of silver paint and acetone is carefully applied to opposite corners of the chip before loading into the SEM. These are used for focusing of the beam and setting the working distance to 6 mm. Use the 20µm aperture and zoom in to 50kX magnification to focus and adjust the X and Y stigmator. Calculate the (X,Y) coordinates on the chip for the position of the flake. Write the alignment marks. A grid of small and large crosses is written with the 20µm aperture (Fig. 5-4). The small crosses are 60µm apart and the large crosses are labeled in a matrix from 00 to 44 (Fig. 5-5 *a* and *b*). They are 300µm apart. The file name for this alignment pattern is 0001.DC2. A larger alignment pattern is written after the stage is move 1100µm above the center of the cross matrix. The file name is BOND_ALIGN.DC2 and the 120µm aperture is used. The chip can now be removed from the chamber and developed with a dip in a 1:3 mixture methyl isobutyl ketone (MIBK) and IPA for 60 seconds, dip in IPA for 30s, followed by a dip in DI water for 60s. The MMA generates more secondary electrons and has a greater exposure than the PMMA so an undercut structure is formed.
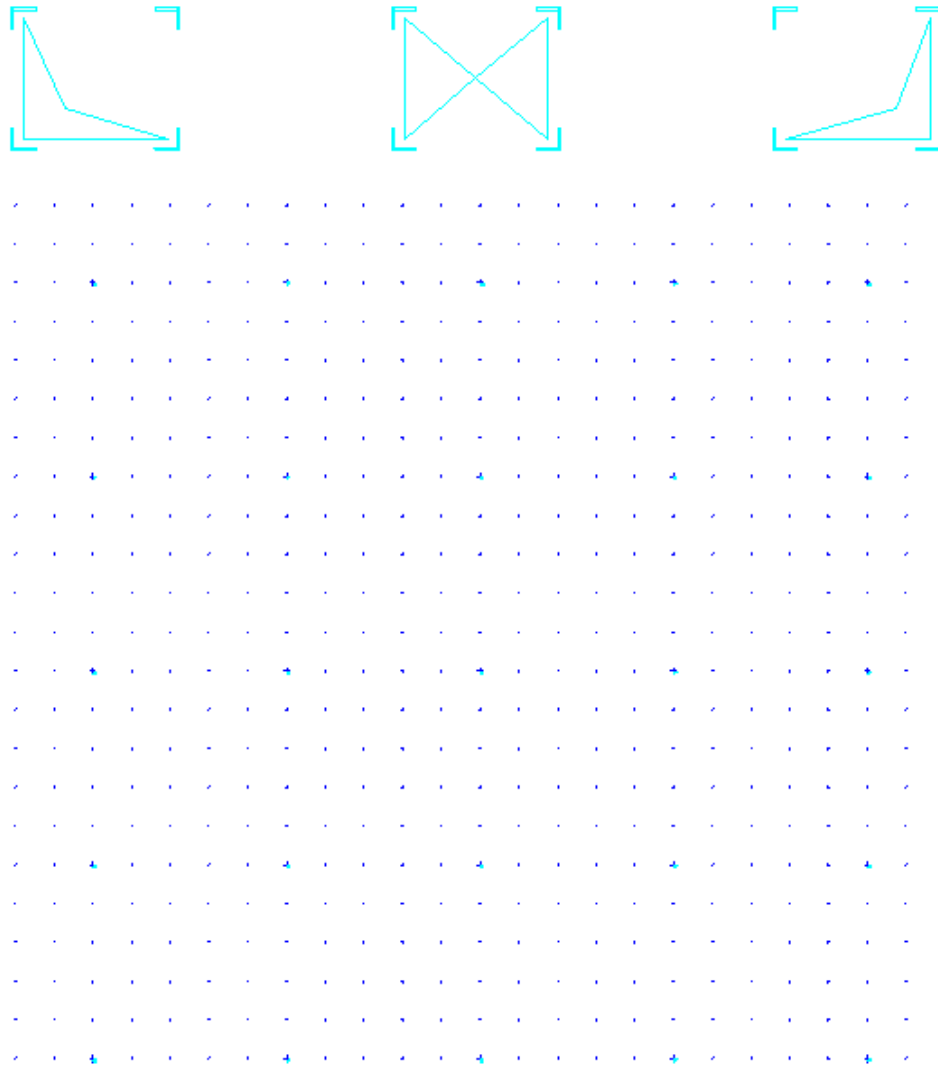
Fig. 5-4 Grid of large and small crosses for aligning with EBL.
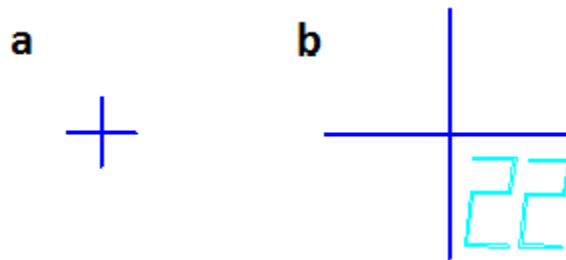
Fig. 5-5 Small cross (a) is 5µm, large cross (b) is 20µm.

Take optical microscope pictures of the position of the flake in relation to the grid at 5X, 20X and 50X objective lenses. Be sure to have the cross pattern parallel to the edge of the picture. Load the images onto the NPGS 0001.DC2 file and adjust the width and height so they match the cross pattern. Design your pattern of electrodes on the flake with contact pads, making sure not to have any pads short-circuited by a large graphite flake (that is why the 5X picture is needed). Draw two windows for large crosses and two for small crosses to use for aligning with the e-beam.

The chip can now be loaded back into the SEM chamber. The e-beam is focused again as previously described. The large BOND_ALIGN pattern is then located using inLens mode on the SEM. Roughly adjust the rotation of the stage so the lines are parallel to the monitor display. Begin the NPGS pattern. Do a fine adjust of the rotation, a rough adjust of the position to the large crosses, a fine adjust of the position to the small crosses, and write the pattern. Remove the chip and develop again as previously described. The device has now been patterned and is ready for metal deposition and lift-off in an acetone or PG remover bath to remove the resist with metal on top. Fig. 5-6 illustrates a few main EBL steps. The device can be annealed in vacuum or in a hydrogen/argon environment at a temperature range of 250°C to 400°C to clean it by removing resist residue [93].
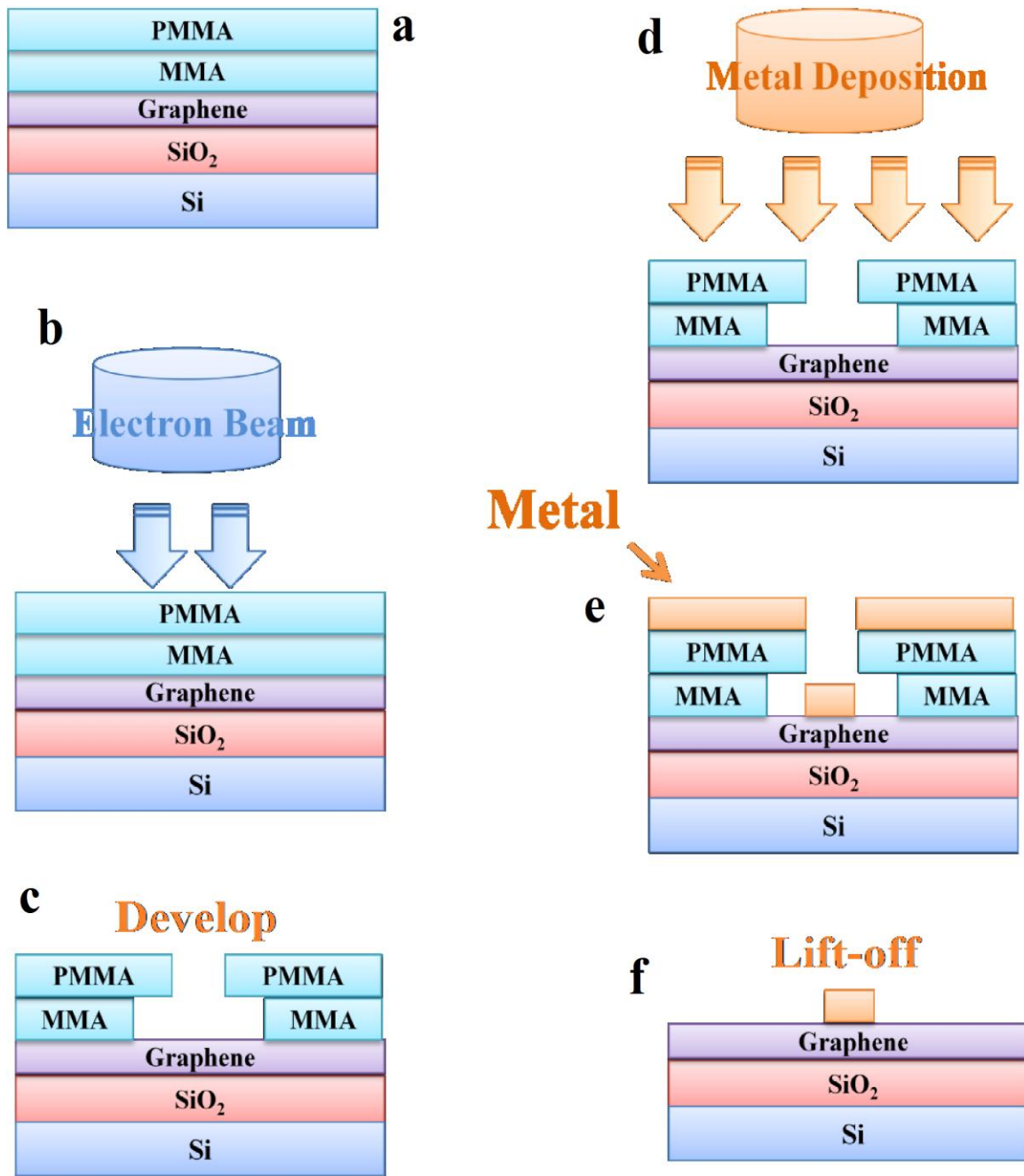
Fig. 5-6 Six main steps for EBL patterning of graphene device. Spin-coat of resist(a), writing pattern with e-beam (b), develop with MIBK, IPA and DI water (c), metal deposition (d and e), and lift-off with acetone or PG remover (f).

5.3   Graphene Field-Effect Transistor Devices

The graphene devices must have a minimum of five electrodes. A source and a drain at the ends, two on the same side for measuring longitudinal voltage in a 4-probe setup (V_{xx}), and one on the opposite side to measure the transverse voltage or Hall voltage (V_{xy}). Typical metals to deposit for the electrodes are titanium with gold on top. The 10nm of titanium acts as a sticking layer with 100nm of gold used for oxidation resistance and ease of wirebonding. I only use 80nm of palladium grown in the molecular beam epitaxy chamber in Prof. Roland Kawakami's lab. I will explain the reason for this in section 5.5. While five is the minimum number of electrodes needed, it is beneficial to have as many as can fit onto a larger flake. Some electrodes may have high contact resistance or may migrate off of the flake during device transfer. Device transfer will be discussed in section 5.5. The drain electrode is grounded and also acts as the ground plate for the backgate.
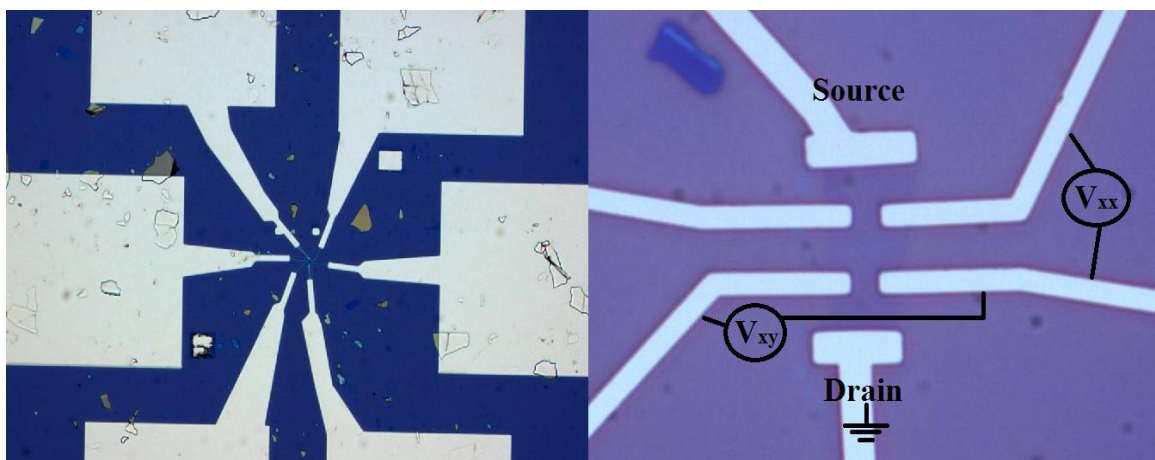
Fig. 5-7 Optical image of graphene FET on SiO$_2$. Low mag. image showing contact pads (left). High mag. image showing source, drain, longitudinal and transverse electrodes (right).

5.4   Measurement Setup

All measurements for this research were performed in a Continuous Flow Cryostat. The system is composed of a Janis Cryostat chamber (see schematic in Fig. 5-8), Janis liquid helium transfer line, GMW electro-magnet with a Kepco power supply, and a Varian Turbo pumping station. The chamber can be pumped to a pressure of 10^{-7} Torr. Liquid helium is used for cooling and a cryogenic temperature can be reached and controlled with a Lakeshore 330 Temperature Controller down to 4K. A Stanford Research Systems Model SR830 DSP Lock-In Amplifier is used to apply an AC source current. An input resistor of $14.12M\Omega$ limits the current to the nano amp range. With two Lock-in amplifiers connected, the voltages V_{xx} and V_{xy} can be measured at the same time. A low frequency of 27.71Hz is used for the measurements. A Keithley 2400 SourceMeter applies the backgate voltage and can measure the leakage current. The gate voltage is connected to an RC circuit before it is applied to the sample to prevent sudden voltage spikes. The measuring equipment is controlled by LabVIEW programs. The sample holder for the system was designed and built in the laboratory. It is composed of a flat brass plate with an Al_2O_3 spacer and a copper foil for applying the backgate. The 1mm thick Al_2O_3 provides electrical isolation while maintaining good thermal contact. Kapton coated copper pins line the edges of the brass plate. The tops of the pins are wirebonded to the sample while the underside is soldered to wires leading to a BNC box for connecting to the measuring equipment.
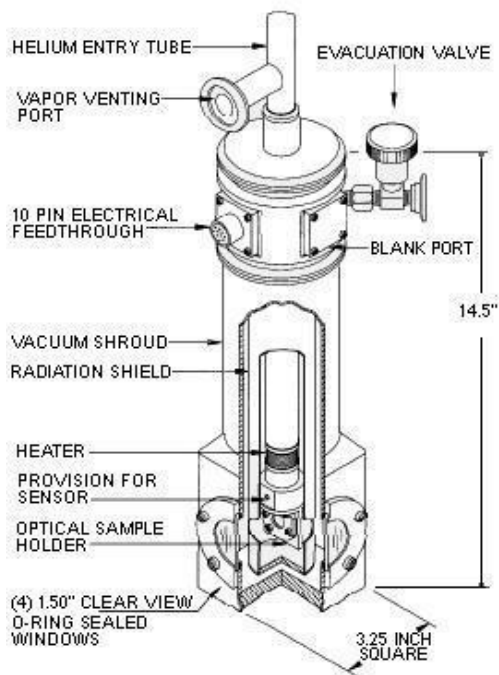
Fig. 5-8 Continuous Flow Cryostat Chamber. Schematic of the system (left). Picture of the system with pump and electro-magnet (right).
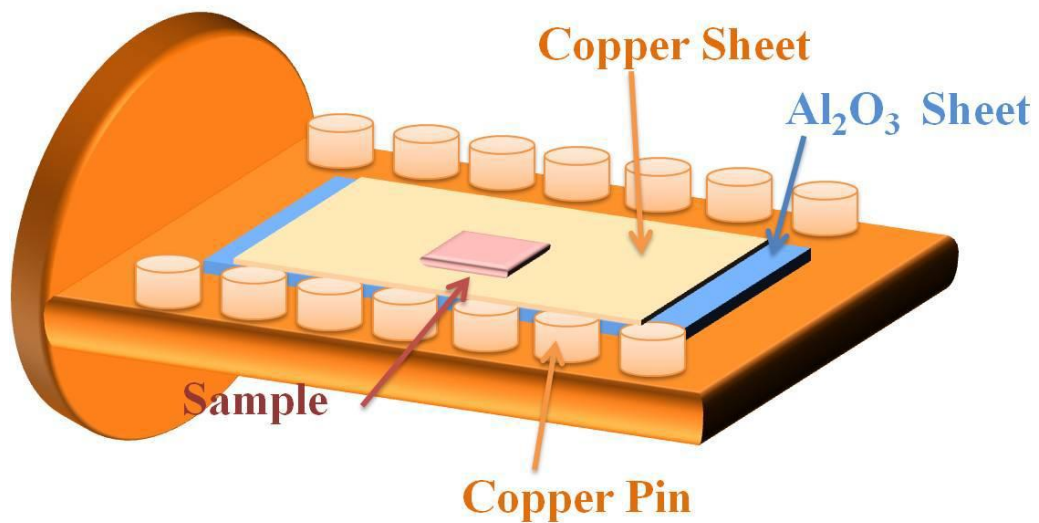
Fig. 5-9 Schematic of the sample holder.

5.5 Device Transfer Technique

The graphene device is fabricated on the surface of SiO_2. This has been done thousands of times by dozens of groups around the world. The thickness of SiO_2 is specifically chosen to be $\approx 300nm$ as mentioned previously because of the ease of locating the flake with optical microscopy. Additional methods for locating single layer graphene flakes are atomic force microscopy (AFM), scanning tunneling microscopy (STM), and Raman mapping. These methods have the potential of damaging the flake and furthermore require a high throughput and are very time-consuming. It may not be particularly straightforward to locate graphene on a substrate other than SiO_2 or even for differing thicknesses. It is indeed possible to establish the position of exfoliated graphene with optical microscopy on the surface of 500μm thick STO using the dark-field. The Morpurgo group has accomplished this [80] and even I have been able to do it myself. But there are additional processing issues with using a thick, high-κ material. The electron beam will become skewed when writing a pattern with EBL due to a surface charging effect. A thin layer (~2nm) of gold must be deposited on top of the PMMA prior to EBL patterning to dissipate the charge. This only adds an additional processing step and may not always be effective. It is much more cost-effective to make and test the devices on cheap Si wafers than expensive STO. Another problem with fabricating directly onto STO is that you can only compare the electron transport characteristics of the device with similar devices on SiO_2.

I have developed a technique for transferring an entire device from the surface of SiO$_2$ to any arbitrary substrate that I choose. This technique eliminates the need to locate the flake on the target substrate for EBL patterning. The graphene device can be measured before and after transferring for a direct comparison of the transport properties. This technique is a modified version of work done by Alfonso Reina in the Jing Kong group at MIT [94]. They have successfully transferred single and few-layer graphene flakes to arbitrary substrates. The key difference with my work is that I have fabricated an entire device with metal electrodes prior to the transfer. I will outline each step in the remainder of this section.

The first step is to fabricate the graphene device on Si/SiO$_2$ wafer as described in section 5.2. The metal used for the electrodes is Pd gown via MBE. This is used in replacement of Ti/Au. The Ti is used as a sticking layer. The problem is that it sticks too well. It is difficult to peel from the surface of SiO$_2$ during the transfer. Pd has been successful from the first instance and I have used it ever since. It also has the benefit of trouble-free wirebonding and exceptionally low contact resistance. The device is next measured while on the SiO$_2$ in accordance with the procedures outlined in sections 5.3 and 5.4. The chip is now prepared for transfer.

A spin-coating of two layers of PMMA is done with 3000 rpm for one minute each. The PMMA is hard-baked on a hotplate at 170°C for 10 minutes between coatings. Submerge the chip in a plastic beaker of a 1 molar solution of sodium hydroxide (NaOH) for approximately two days. The NaOH will partially wet-etch the

SiO$_2$. Remove the chip from the NaOH and place in a beaker of DI water. The PMMA layer can be carefully peeled from the surface. Using two pairs of tweezers (preferably metal with flat, rounded edges), one will hold the chip at the edges to the bottom of the beaker and with the other tweezers, gently pick at all of the edges of the PMMA layer until you can see that it is no longer attached. I specifically select Si wafers that have clean edges without cracks so the PMMA layer will detach easily. Once you can see that the PMMA film can move freely, slowly lift the chip to the surface. The transparent layer with the device will adhere to the surface of the water due to surface tension and the hydrophobic nature of PMMA. This is the step that takes the most skill and a steady hand.

With PMMA/device layer floating on the surface, the target substrate is brought up from underneath so that the layer is pulled out and lies flat. Place this onto a hotplate at 50°C for ten minutes. Most of the extraneous wrinkles will disappear as the water is slowly baked away at the interface. The target substrate can then be placed in a beaker of acetone at 65°C for 30 minutes to remove the PMMA followed by a 10 minute bath in IPA. It is imperative that you do NOT use squirt bottles or an ultrasonic cleaner. This may wash away portions of the device, rendering it useless for measuring. Dry the chip with a gentle flow of nitrogen gas and it is ready for transport measurements. Pictures of the equipment needed and a diagram of the transfer technique are provided on the following pages.
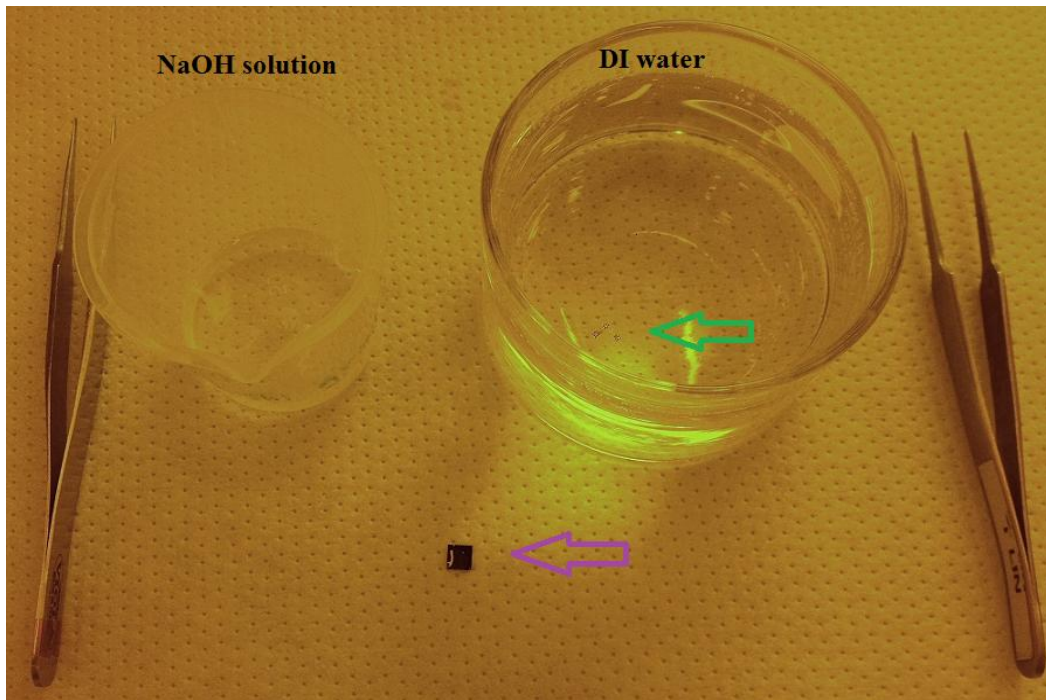
Fig. 5-10 Image of equipment needed for device transfer. Two pairs of tweezers, plastic beaker of NaOH solution, beaker of DI water. Green arrow highlights PMMA layer with 3 devices. Purple arrow highlights used Si wafer.
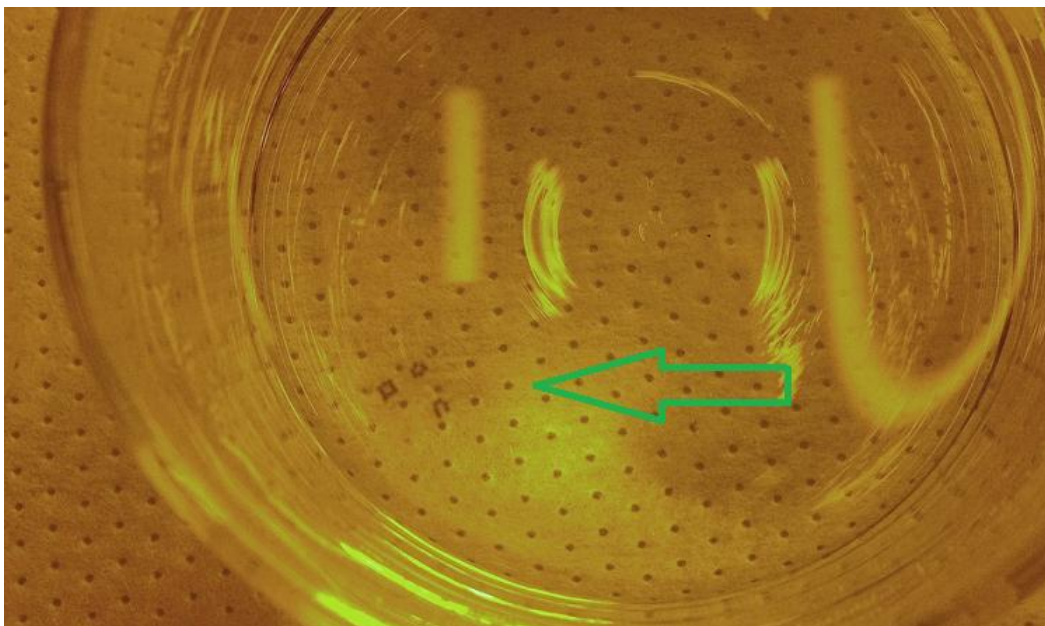
Fig. 5-11 Close-up image of PMMA/device layer floating in DI water.
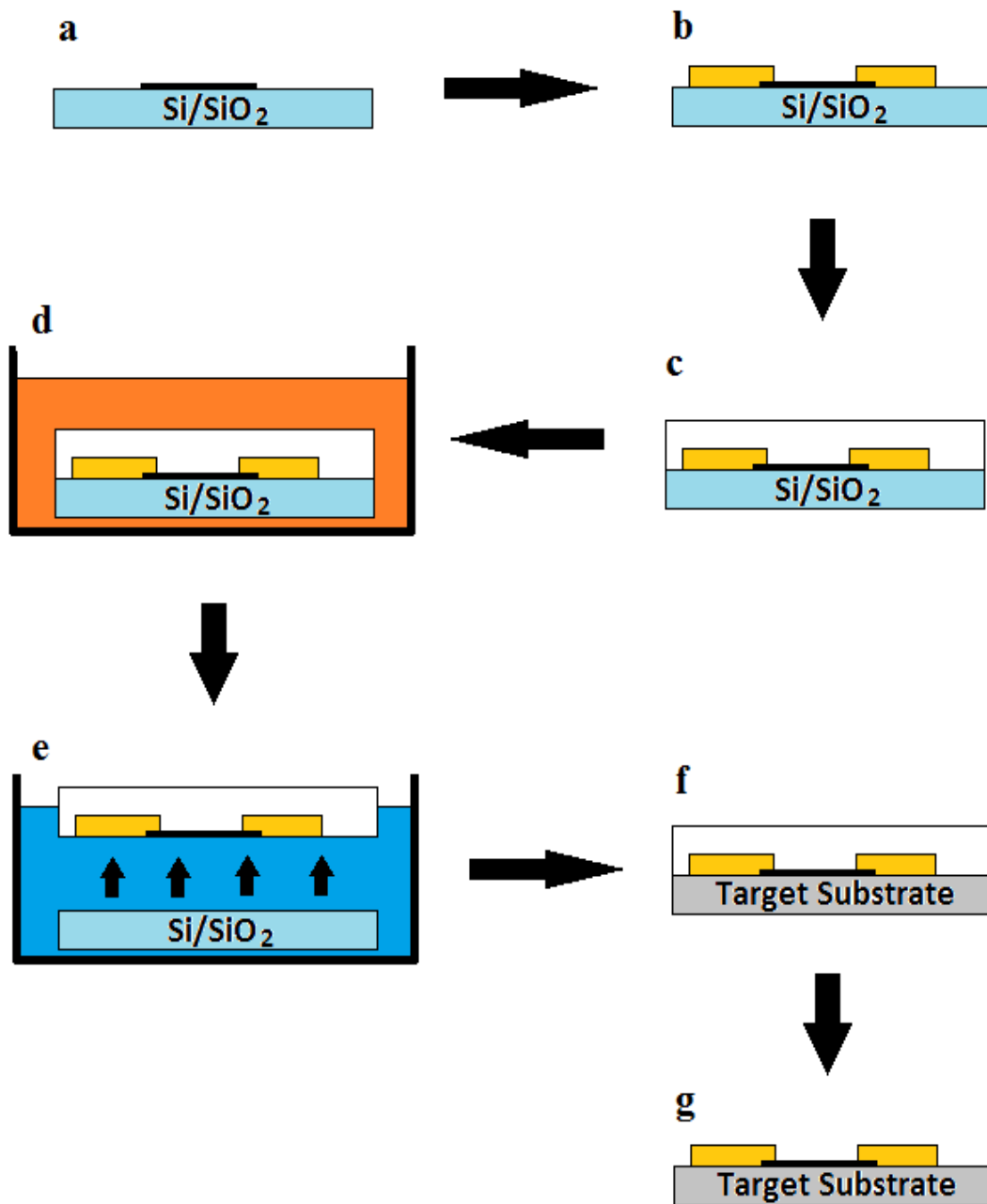
Fig. 5-12 Diagram of main steps in the device transfer technique. Exfoliate
graphene (a), EBL patterning of device and metal deposition (b), spin-coat PMMA
layer (c), submerge in NaOH solution for 2 days (d), peel from SiO_2 and lift to the
surface of DI water (e), place PMMA/device layer onto new substrate (f), remove
PMMA with acetone (g).

Fig. 5-13 Image of graphene devices after transfer to STO.

Before Transfer   After Transfer
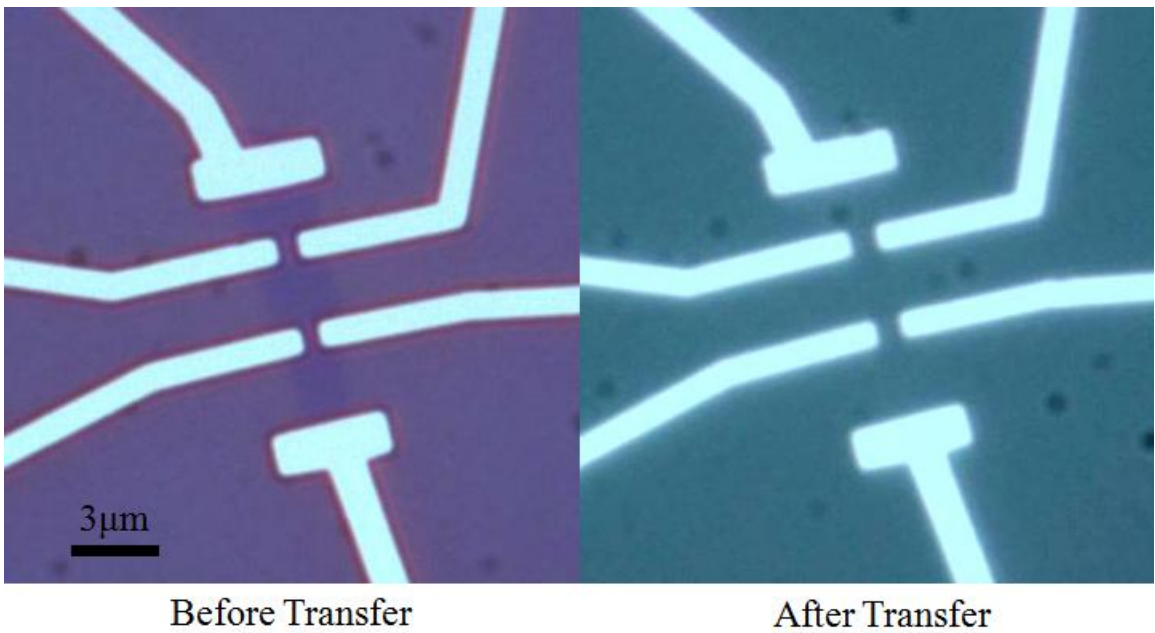
Fig. 5-14 Same graphene device on SiO$_2$ (left) and STO (right).

5.6   Preparation of STO Substrates

The target substrate we have used for the transfer has been single crystal STO. Both 500μm thick STO (111) from CrysTec GmbH and 200μm thick STO (100) from MTI Corporation have been used. The substrates have to be cleaned before the transfer by successive dips in acetone, IPA, and DI water. Each of these steps is done with an ultrasonic cleaner for 30 minutes at ambient temperature. The substrates are then picked up by the edges with plastic tweezers and dipped in a buffer oxide etchant (BOE) solution for two minutes. BOE is a mixture of a buffering agent ammonium fluoride (NH_4F) and hydrofluoric acid (HF). This step is to ensure an atomically flat surface. The last cleaning step is to dip in DI water for 20 minutes, changing the water half way through.

A final step of annealing the substrate at 800°C for one hour in ozone was added. The purpose of this was to ensure that there were no oxygen deficiencies at the surface. The transport properties of graphene on STO were not affected between annealed and unannealed substrates. Annealed substrates had three times higher surface roughness however as evidenced by before and after AFM images (see Fig. 5-15).

Image Statistics

Img. Rms (Rq)	0.891 nm
Img. Ra	0.434 nm

Box Statistics

Z range	6.766 nm
Rms (Rq)	0.593 nm
Mean roughness (Ra)	0.352 nm
Kurtosis	19.025

Image Statistics

Img. Rms (Rq)	1.293 nm
Img. Ra	0.976 nm

Box Statistics

Z range	9.304 nm
Rms (Rq)	1.145 nm
Mean roughness (Ra)	0.906 nm
Kurtosis	3.393
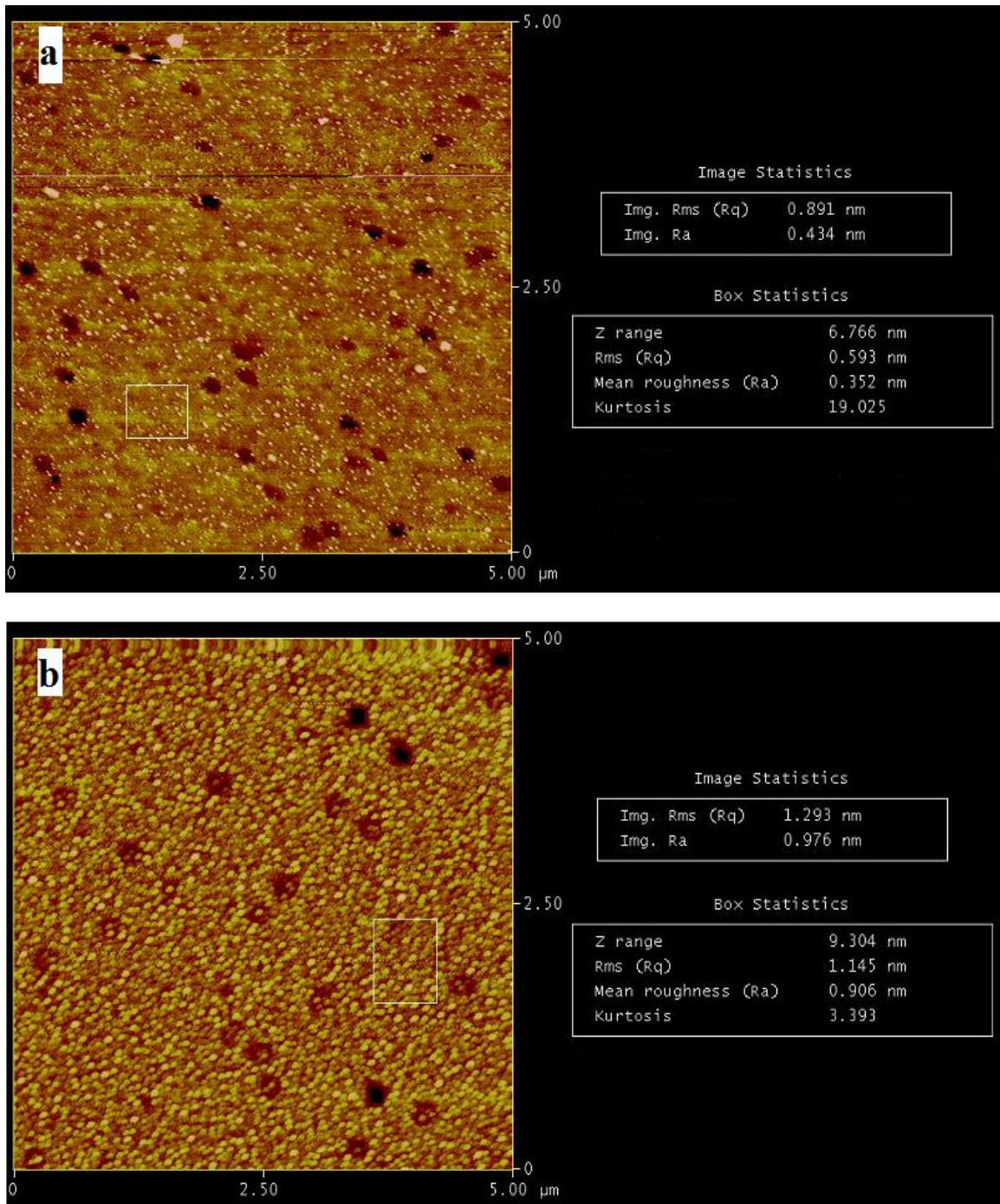
Fig. 5-15 AFM images of STO substrates before (a) and after (b) annealing in ozone at 800°C.

5.7 Pulsed Laser Deposition of STO

Growth of thin layers of STO was accomplished using the PLD system built in our laboratory. PLD is a physical vapor deposition technique using a high-power pulsed laser focused onto a target material in vacuum. The target material is vaporized from a rotating stage, sending a plume of material plasma onto the sample. The sample is situated above the target, faced down and normal to the plume (Fig. 5-16). The homemade PLD system consists of a vacuum chamber with aligned mirrors to guide the laser. A Coherent Compex Pro KrF excimer laser with wavelength of 248nm is used as the ablation source (Fig. 5-17).
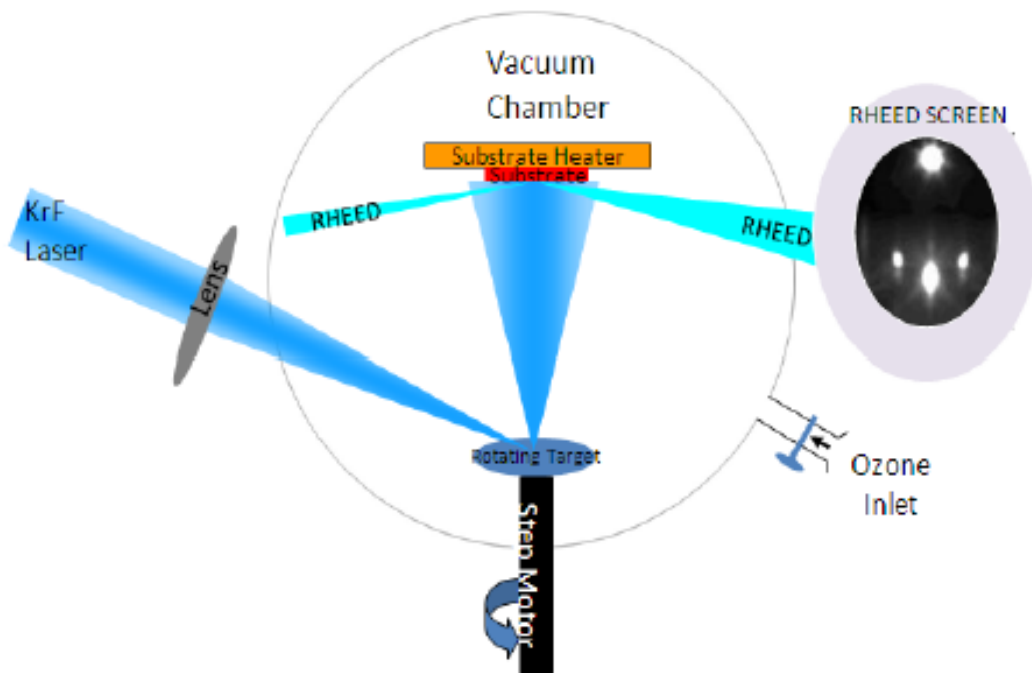
Fig. 5-16 Diagram of PLD system.

Fig. 5-17 Picture of PLD system built in Dr. Jing Shi's lab.

The STO is grown on a conducting niobium (Nb) doped STO (100) substrate with 0.1% doping concentration. The Nb-doped STO substrate is cleaned and prepared for deposition in the same manner as the STO single crystal substrates described in the previous section. The sample is loaded in the chamber and evacuated overnight to a base pressure of 9×10^{-8} Torr. Ozone is leaked in for a pressure of 7×10^{-3} Torr and the resistive sample heater is increased to approximately 800°C. Ozone and high temperatures are needed to ensure that we achieve very good oxygen stoichiometry. Oxygen deficiencies will cause the STO to be conducting and unacceptable gate leakage will result. The laser power is adjusted to ~190 mJ and is pulsed at a frequency of 1Hz for 10 minutes. The sample is then

allowed to heat for 10 minutes. Nines cycles of this are repeated. The annealing in

ozone between depositions is again to ensure no oxygen deficiencies. The sample is

removed from the chamber and annealed in a tube furnace for 6 hours at 1100°C

with an O_2 flow. The sample is place back in the PLD chamber and the process is

repeated. We must take pains to prevent any oxygen deficiencies, otherwise this

time intensive process will be pointless with a device that cannot be gated.

It is important to know the thickness of the STO layer grown so that the

capacitance can be determined. The PLD system has a reflected high energy electron

diffraction (RHEED) system to monitor the number of layers and the crystallinity of

the film in real time as it is grown. As the intensity of the RHEED pattern waxes and

wanes, one complete cycle indicates that one layer has been grown. Counting the

number of cycles gives an accurate measure of thickness with one layer equal to

0.9nm.
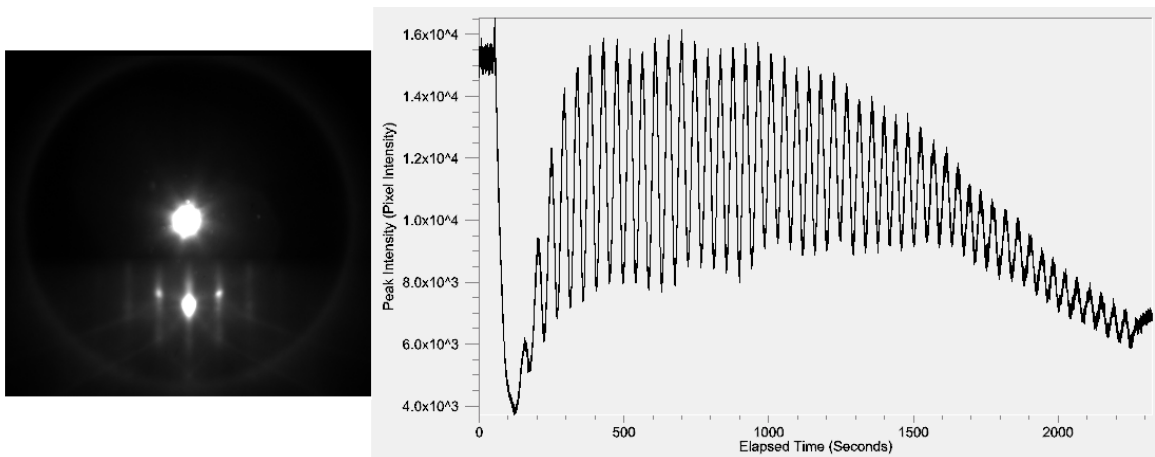
Fig. 5-18 RHEED pattern (left) and Intensity vs. time curve (right). Oscillations
indicate layer-by-layer growth.

The thickness can be roughly verified using the Dektak profilometer in the cleanroom. A stylus is dragged across at a step edge between the grown layer and an area shadowed by the sample holder. The resolution is comparably low for this instrument, but it is adequate for films on the order of hundreds of nanometers. AFM images are taken to corroborate that the film is atomically flat. Fig. 5-19 shows that the STO film grown has clear step edges.

Many films were deposited for the transfer of a graphene device. Only one had a low enough gate leakage to be measurable. More extensive work needs to be done with this research for a nice paper to be published.
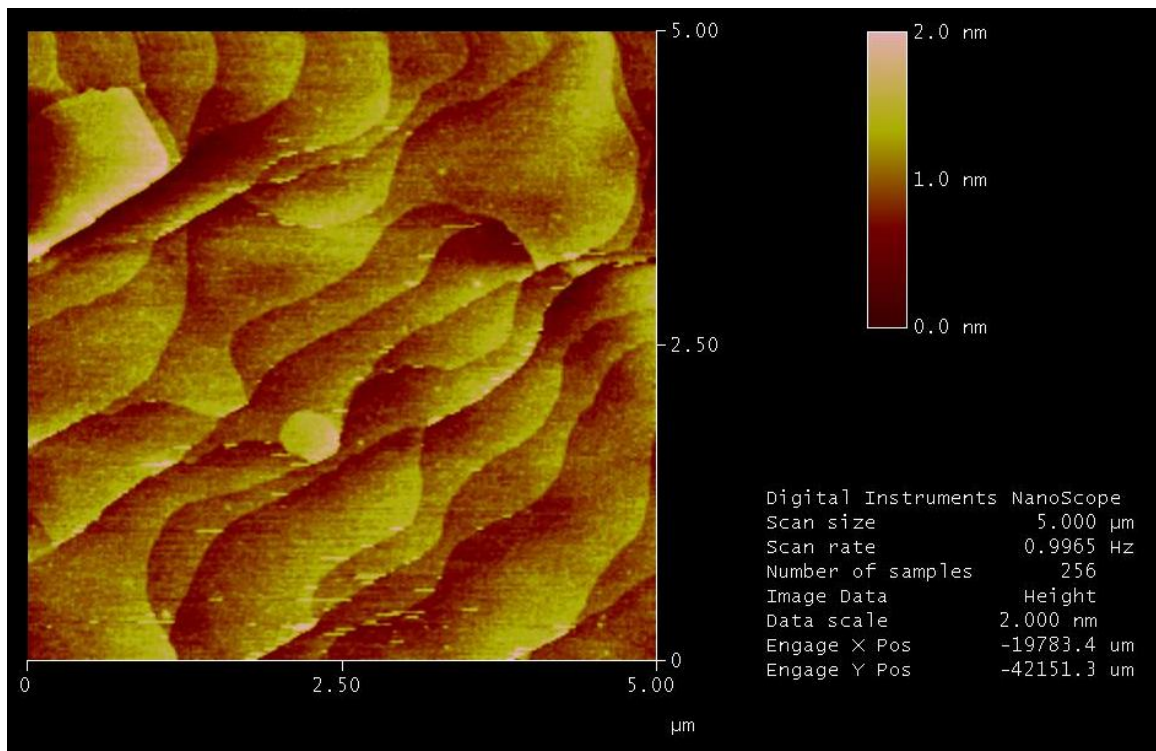
Fig. 5-19 AFM image of STO deposition via PLD on Nb-doped STO(100).
Atomically flat step terraces are visible.

Chapter 6
Results and Conclusions

6.1   Introduction

The device transfer method has been developed to study graphene devices on arbitrary substrates and compare transport properties with graphene on SiO_2. STO has been chosen as the target substrate for a number of reasons. The most trivial reason is that we have the ability to grow thin, epitaxial layers in our laboratory. But we also wanted to utilize the high dielectric constant of STO. At room temperature, the dielectric constant of STO is two orders of magnitude higher than that of SiO_2. The hypothesis was that with the enhanced dielectric screening, the mobility should be increased by two orders of magnitude. At cryogenic temperatures, STO has a dielectric constant of between 5,000 and 10,000. The mobility of graphene is expected to increase dramatically with lowering temperature. Evidence showing that the carrier mobility is not greatly enhanced with a high-κ environment will be presented and discussed. Other interesting and unexpected phenomena such as the time dependence of the backgating measurements and saturation of the carrier density at high V_g will also be presented and discussed.

6.2 Gate Dependence

With a gate oxide of SiO_2, the graphene gate dependence exhibits the usual hysteretic behavior. However, upon heating the sample and vacuum pumping the chamber for 10 or more hours, the hysteresis will disappear. This effect has been studied extensively by Deqi Wang [65] and is attributed to chemical adsorbates on the graphene surface that act as charge reservoirs. The graphene that has been transferred to the surface of STO exhibits an extreme hysteresis effect. Sample heating and pumping has no effect of minimizing this hysteresis. There are two methods we have discovered that can change the positions of the dual Dirac points; by increasing the gate step wait time and changing the sweeping range of V_g. For the wait time variation, the gate voltage is ramped and waits at a set point for a determined amount of time. After this time has expired, then the measurement is taken. This gives the STO some time to "relax". The next gate voltage is ramped to and the waiting begins again. With the increase in wait time, the Dirac positions change sides. For example, at three minute wait, the peak on the down sweep is on the left at a negative gate voltage and up sweep peak is on the right at positive gate voltage. With a longer wait time of six minutes, these peaks will switch positions. At an even longer wait time of 12 minutes, the two peaks are further apart. These curves are plotted in Fig. 6-2.
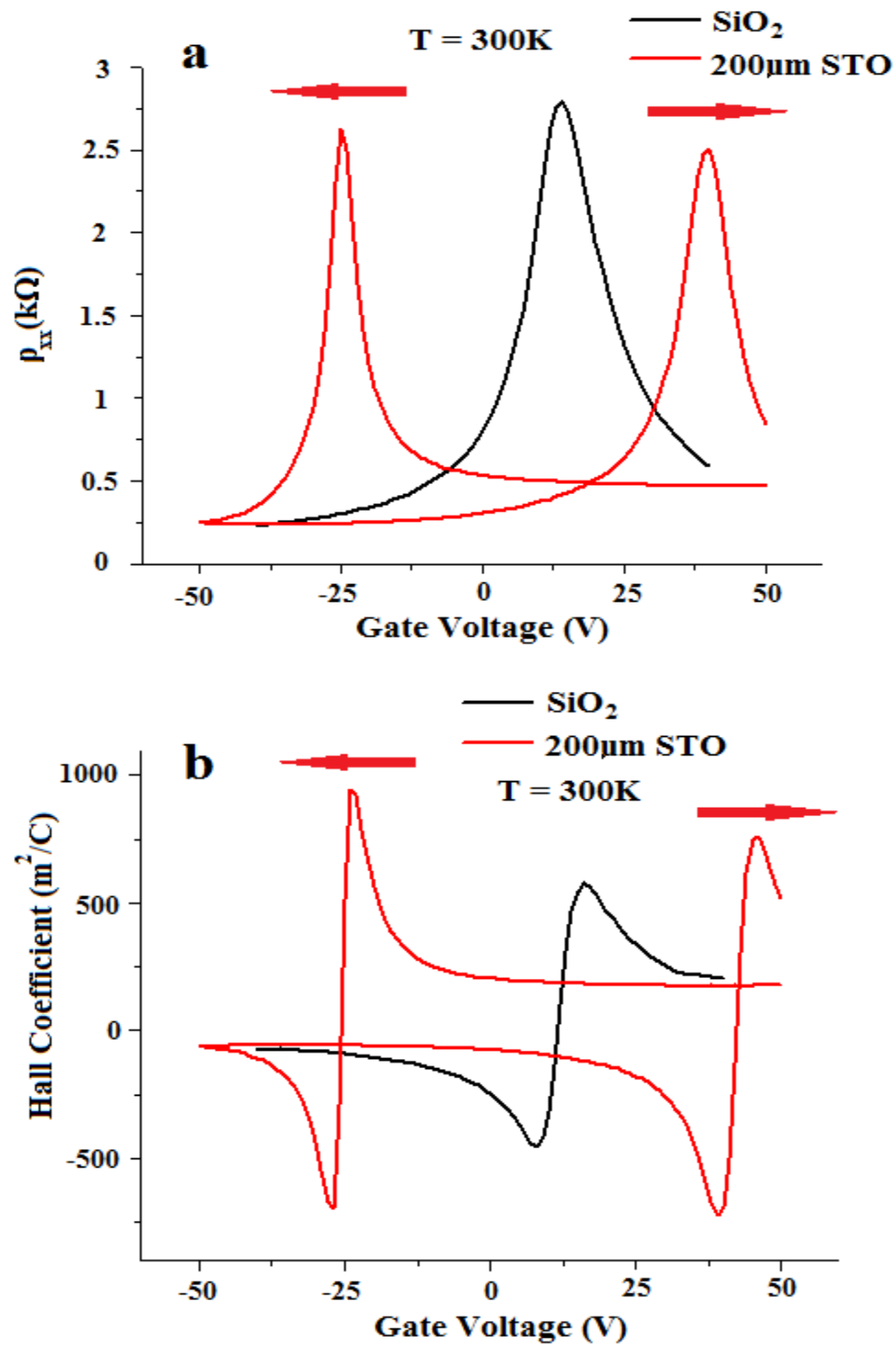
Fig. 6-1 Graphene sheet resistance (a) and Hall coefficient with B = 0.15T (b) on SiO₂ (black) and transferred to 200μm STO (red). Arrows indicate direction of V_g sweeping.
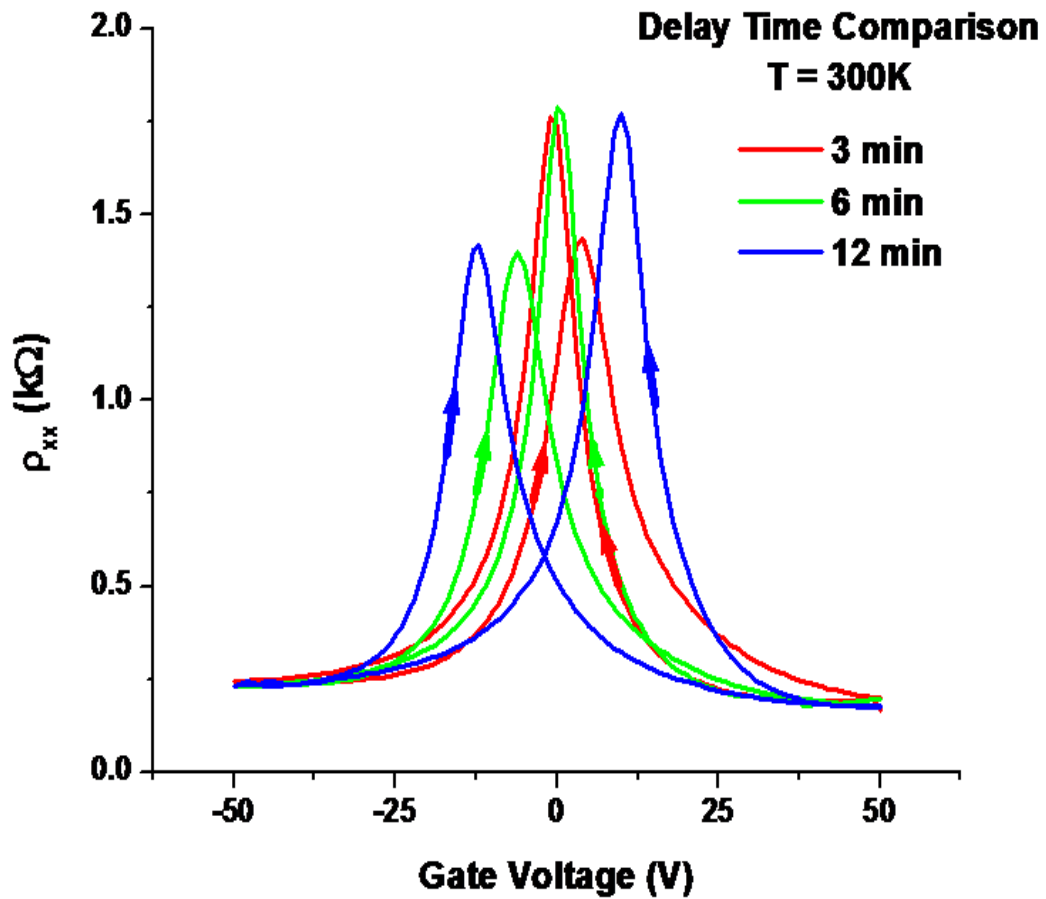
Fig. 6-2 Sheet resistance of graphene on 200μm STO with varying gate step wait times. Arrows indicate the direction of the V_g sweep. Peaks change position at longer wait times. See text for details.

Because the STO is 200μm thick and has a high κ, the gate voltage range can be increased to the maximum value attainable by a Keithley 2400 source meter: ±200V. For varying V_g ranges with the same wait time, the positions of the two Dirac points appear at different gate voltages. This wasn't too surprising if the relaxation of STO is considered, as it takes more time to sweep the gate with a higher V_g range. The time dependence of STO relaxation will be discussed in section 6.4.
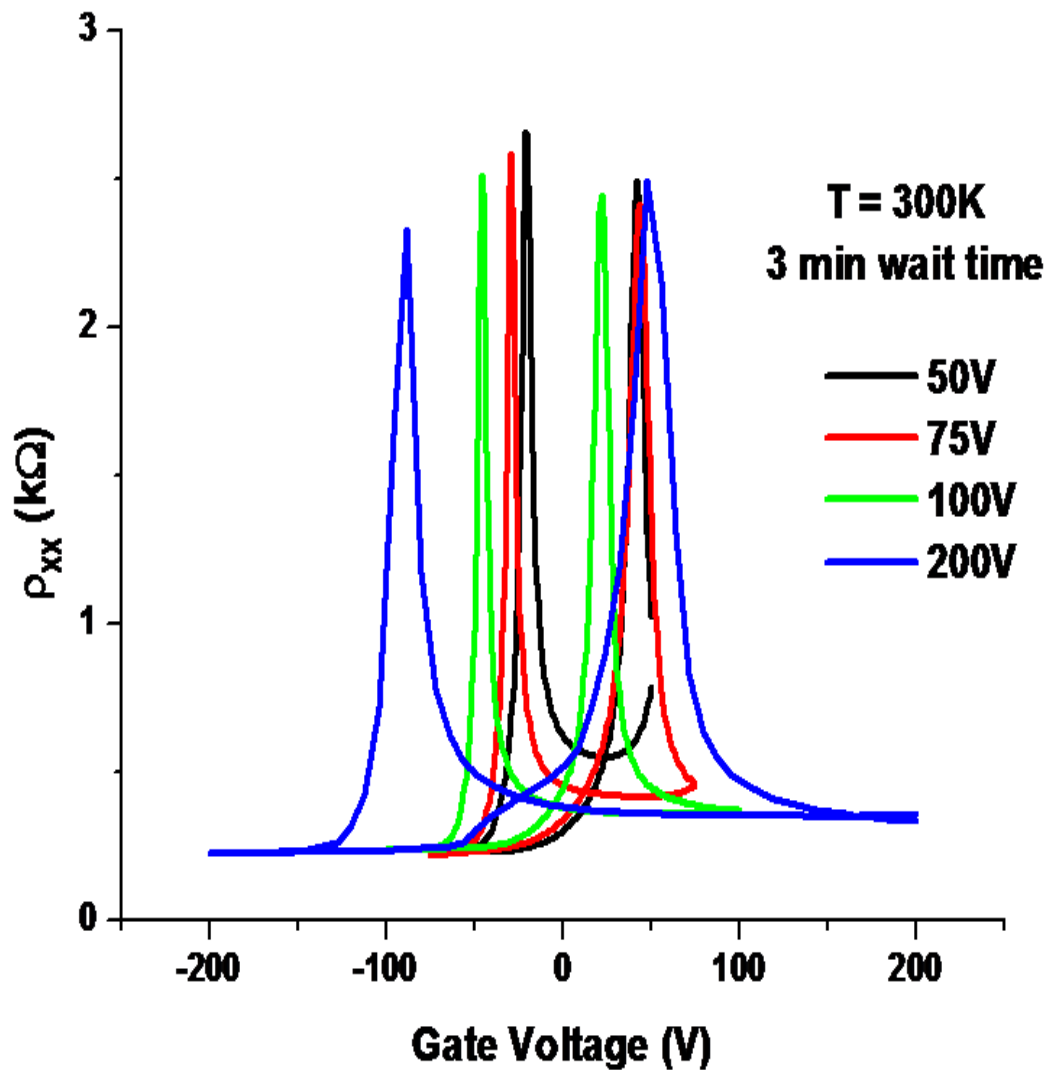
Fig. 6-3 Sheet resistance of graphene on 200μm STO with varying V_g range. The wait time is consistent for all curves. Positions of the Dirac peaks vary with V_g range.

At high gate voltages, the carrier density is expected to increase linearly.

Densities as high as between 10^{14} and 10^{15} cm^{-2} were anticipated with the high

capacitance of STO. Such high values are expected to give rise to superconductivity

in graphene as the M and M' points are reached [95]. However, these high values of

carrier densities are not what we have been observing with our devices on STO. As

the gate voltage approaches high values, the carrier density saturates. We believe

this behavior can be modeled by surface dipoles in STO. More on this will be

discussed in section 6.5. The *n* vs. V_g curves (Fig. 6-4) have been linear fitted around

the Dirac point to make them continuous.
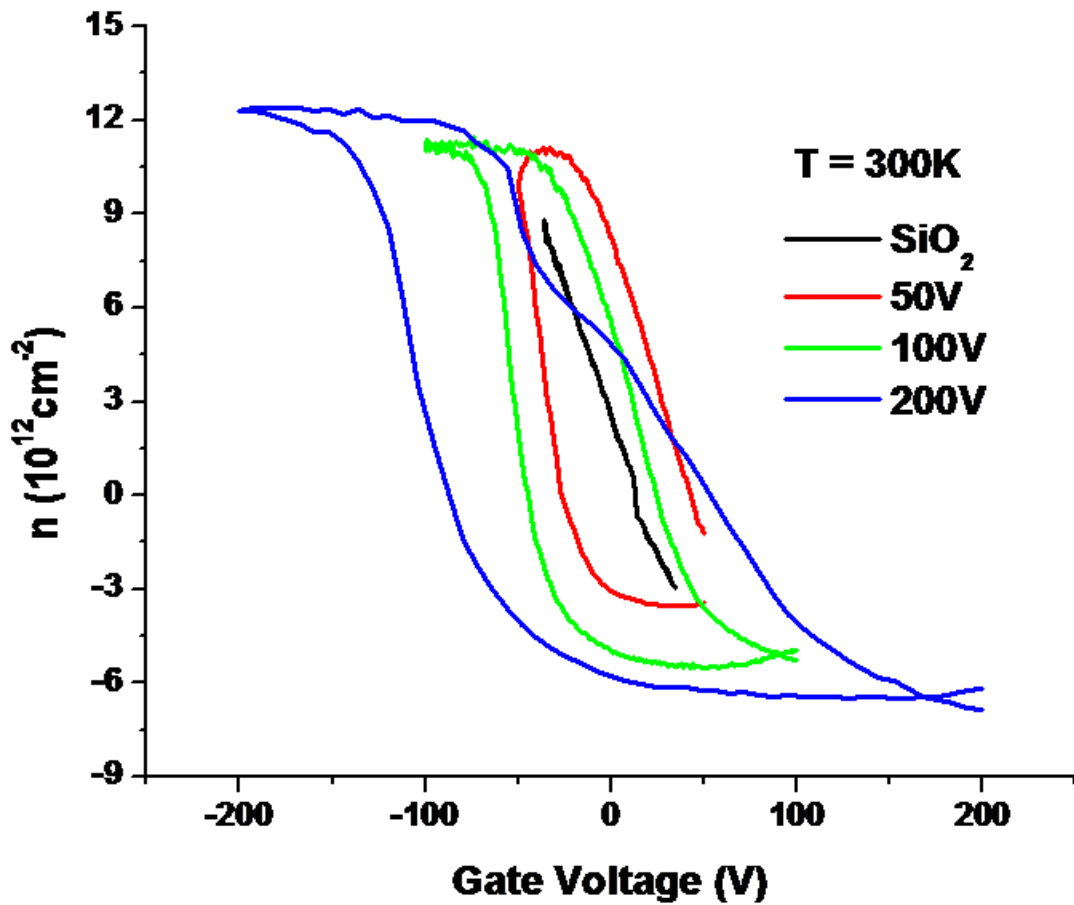
Fig. 6-4 Carrier density vs. gate voltage of graphene on 200μm STO. Density
becomes saturated at high V_g.

The conductivity of the graphene sheet as a function of the carrier density, however, is not hysteretic. The carrier density is calculated from the Hall data (R_{xy} vs. V_g) using a constant magnetic field of 1500 Gauss. This is used as the x-axis with the Dirac point regions linear fitted. The carrier density calculation breaks down in this region due to the divergence (n is proportional to $1/eR_{xy}$). The y-axis, σ_{xx}, is calculated from the longitudinal resistance R_{xx} vs. V_g measurement. With this plot of σ_{xx} vs. n, V_g is a hidden variable, each curve is nearly identical and is independent of voltage range and wait time. The graphene mobility, calculated from the slopes of these curves ($\sigma = ne\mu$), is equivalent for all curves on STO. The σ_{xx} vs. n plot reveals the intrinsic electronic transport characteristic of graphene on STO. A more accurate comparison can be made between transport properties of graphene on SiO_2 and STO. At high density, the slope for STO is smaller than for SiO_2, indicating lower mobility. But at low density, the σ_{min} plateau is much smaller for STO, which indicates a decrease in the electron/hole puddle region. This is evidence that Coulomb scattering suppression is happening in the regime. Precisely what is predicted by the Das Sarma theory [87] for scattering at low density. A fit to the model will be presented in the next section.
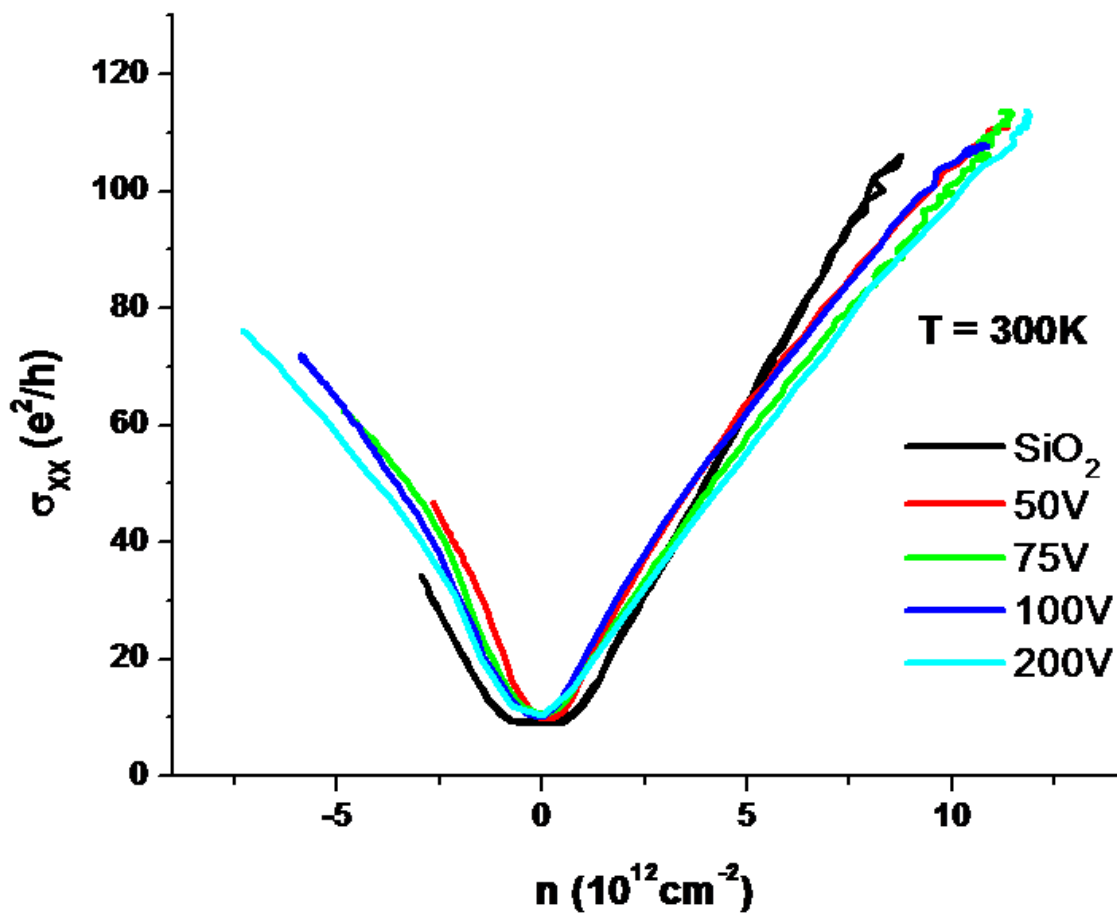
Fig. 6-5 Conductivity vs. carrier density for graphene on 200μm STO.
Measurement taken at room temperature for various gate voltage ranges. All curves for STO are nearly identical. SiO₂ data has larger plateau region around σ_{min}, but a higher mobility at high density.

6.3   Temperature Dependence

The dielectric constant of STO has a striking dependence on the temperature. It will increase from 200 – 300 at room temperature up to between 5,000 and 10,000 at cryogenic temperatures [80]. With this two orders of magnitude increase, it was our hypothesis that the dielectric screening of charged impurity scatterers should cause the mobility to increase by two orders of magnitude. We have not seen this effect in any of our devices. On the contrary, we observe minimal to no change in the mobility at high carrier densities, and only 3 to 4X higher mobility at low density as shown in Fig. 6-6. The apparent enhancement around the Dirac point may seem a bit misleading as the calculation breaks down at zero carrier density. The disregarded density region for SiO_2 and 300K STO is $\pm 1.3 \times 10^{12}$ cm^{-2}. For 4K STO, a smaller density range of $\pm 3.5 \times 10^{11}$ cm^{-2} is discounted. The region of the breakdown is illustrated by hollow squares in Fig. 6-6. The result is in agreement with the Sankar Das Sarma model of competing scattering mechanisms at differing densities [87]. With this model, the assumption is made that charged impurity scattering is dominant at low densities in graphene on STO and on all substrates for that matter. Our data shows that the mobility enhancement around the Dirac point is evidence of the dominant Coulomb scattering being suppressed. It is not as high as we have hypothesized due to the competing scatterers which are still active. At high densities, the mobility is unaffected due to the augmented dominance of short-range scatterers which are density independent. The conductivity vs. density curves for

graphene at 300K and 4K has been fitted to this model and are in very good

agreement (Fig. 6-7).

$$\frac{1}{\sigma_T} = \frac{1}{\sigma_{imp}} + \frac{1}{\sigma_{sd}} \qquad (1)$$

The model fit I did in accordance with the Eq. (1) is to approximate that the charged

impurity conductivity is linearly proportional to the carrier density ($\sigma_{imp} = \beta n$) and

the short-range scattering conductivity contribution is independent of n and is a

constant ($\sigma_{sd} = \alpha$). The model fit gives us the values for parameters α and β for 300K

and 4K. Both parameters are increased at low temperature indicating charged

impurity and short-ranged scattering are being suppressed. By setting $\beta = e\mu$, the

mobility change at low density can be calculated from the model fit. Only a modest

percent increase in the mobility is calculated which does not agree with our

hypothesis of an increase of two orders of magnitude at low temperature. The

values for α, β and μ at 300K and 4K for the device on STO are presented in

Table 6-1.

Table 6-1 Fitting parameters α, β, and calculated μ for graphene on STO at 300K and 4K.

	α	β	Mobility cm^2/Vs
300K	393.95	13.191	3,189
4K	534.92	17.598	4,254
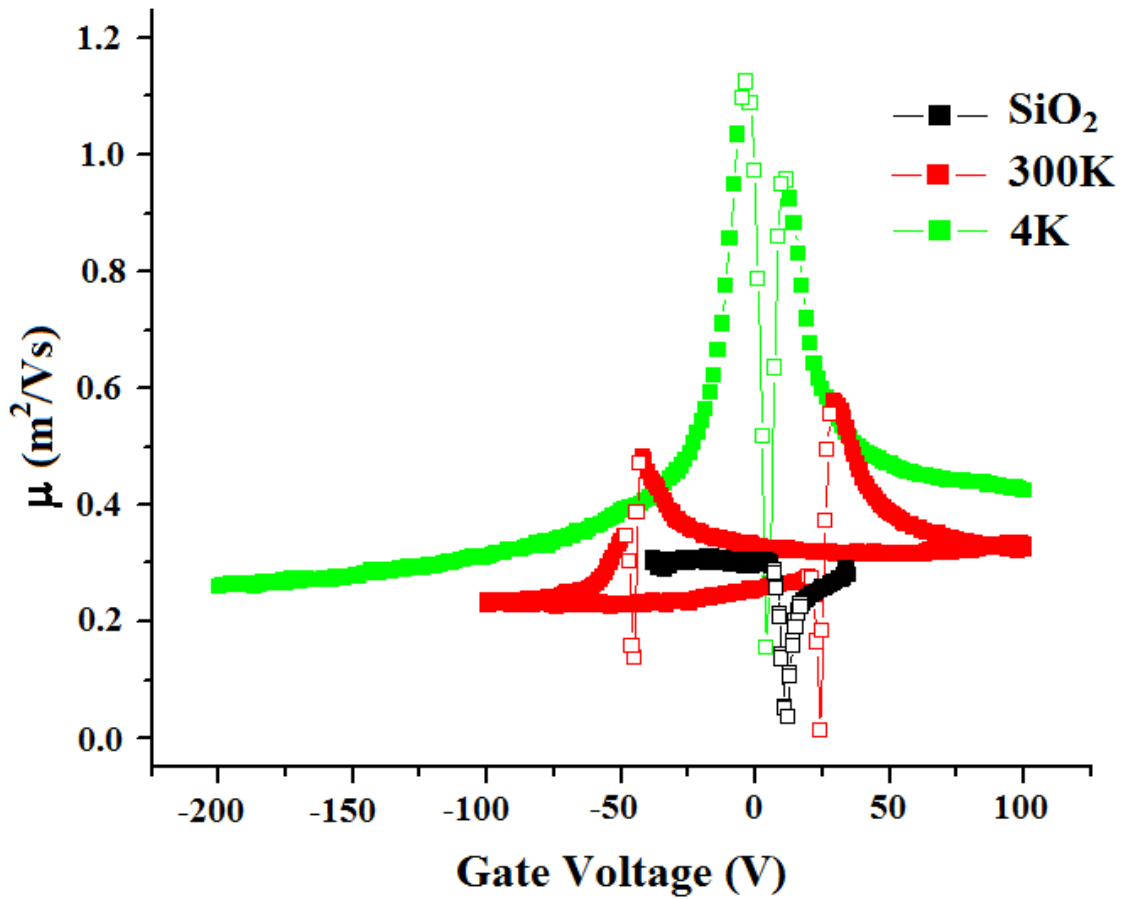
Fig. 6-6 Mobility vs. gate voltage for graphene on STO at room temperature and cryogenic temperature. Graphene mobilities at high density are comparable to each other at both temperatures and with graphene on SiO$_2$. At low density, the calculation starts to break down due divergence of n. The region to be discounted is labeled with hollow squares.
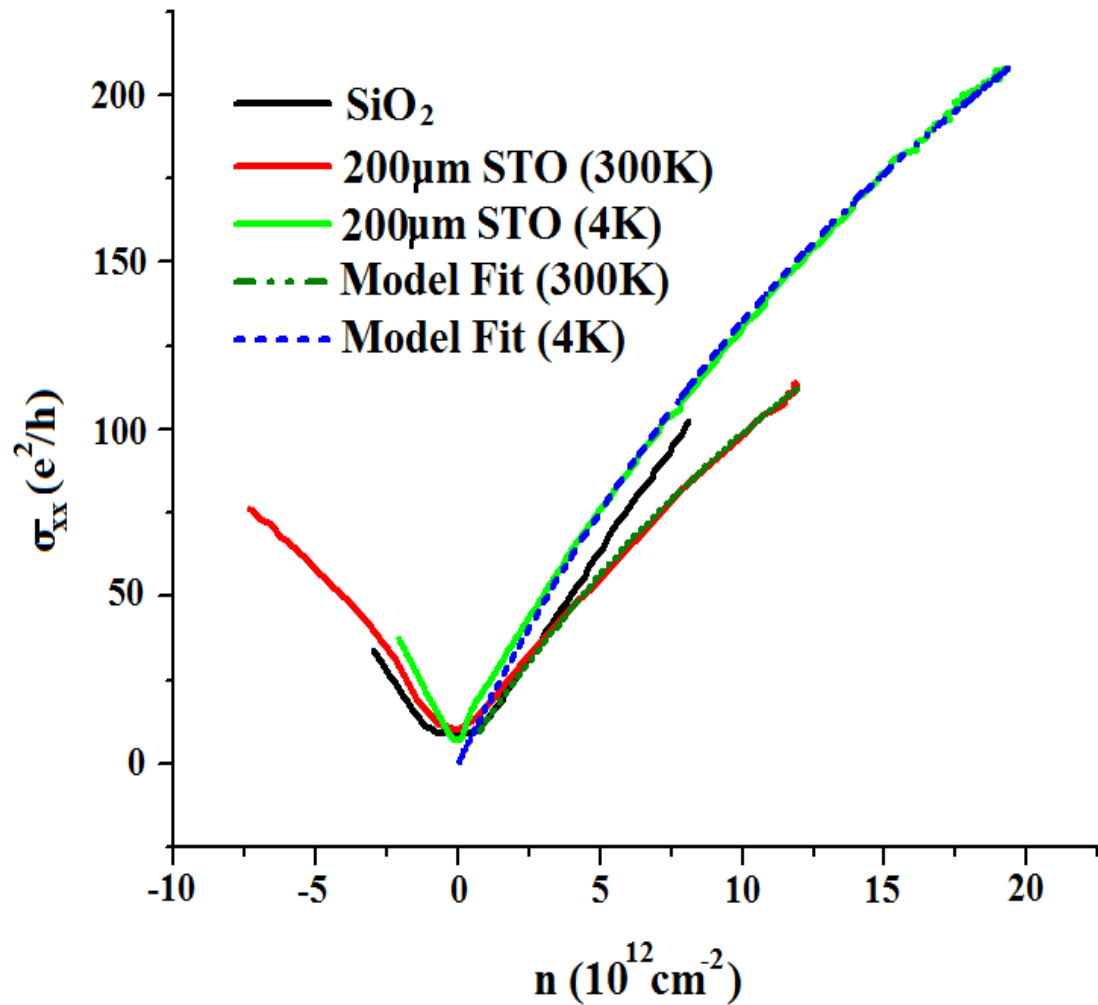
Fig. 6-7 Conductivity vs. density for graphene on STO at room temperature and cryogenic temperature. The curves are fit to a model of dual scattering mechanisms. Details in text.

6.4   Time Dependence

The time dependent relaxation of the STO substrate has been hinted at with the time delay measurements of the gate voltage as discussed in section 6.2. It was necessary to measure this relaxation as a function of time. In order to do this, the gate voltage was first ramped to +200V and held constant until the sheet resistance stabilized (Fig. 6-8). This allowed the STO to rest into a constant state. This was needed so every measurement was initiated at the exact same state. The gate voltage was then ramped down to differing final voltages while R_{xx} and R_{xy} were measured as functions of time. Even while V_g had finished quickly ramping down, the carrier type is stuck at electrons for a time and the density continued to change slowly. At large negative or positive voltages (see Fig. 6-9 and 6-10), the relaxation to constant density occurred relatively quickly due to the driving force of the high electric field. At low gate voltages, the switch from electrons to holes occurred much more slowly due to the smaller driving force of a weaker electric field. At the final gate voltage of +50V, the carrier density begins at n-type at +200V, it switches to hole-type and then back again to electrons. Fig. 6-11 gives a closer look at R_{xx} sweeping twice through a resistance maximum while the Hall coefficient switched signs twice. A voltage of +40V and below has only one switch from electrons to holes, while +60V and above there is no switch, its stays n-type. +50V appears to be a "tipping point". It is my hypothesis that this is the true position of a singular Dirac point if there were an absence of hysteresis. Graphene conductivity plotted as a

function of carrier density in Fig. 6-12 has time as a hidden variable and again

reveals that there is no hysteresis and that every curve is identical. This is more

evidence that the time dependent nature of the measurements is intrinsic to the STO

and the σ_{xx} vs. n curve is the intrinsic response to graphene electron transport.
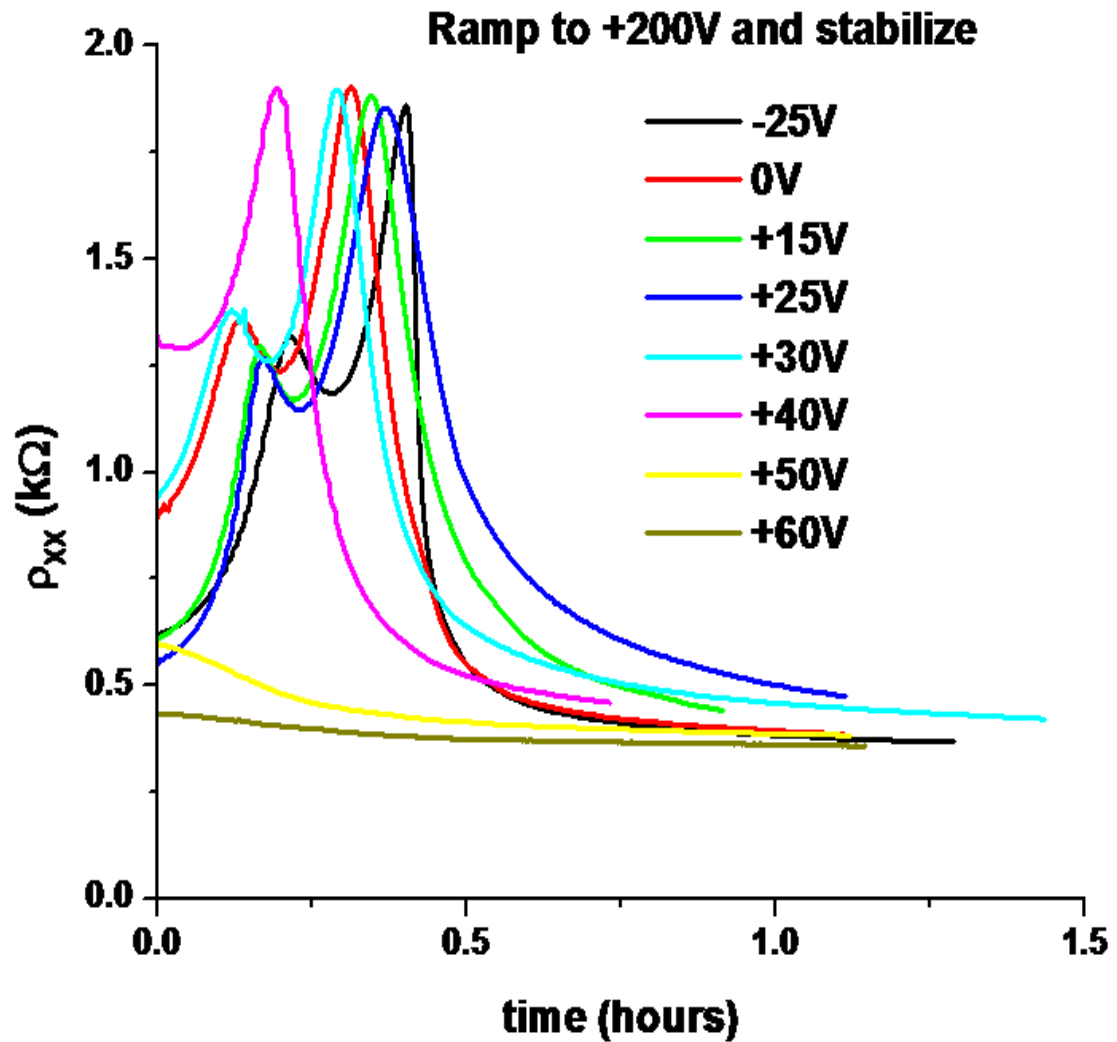
Fig. 6-8 Resistance vs. time for graphene on STO ramped to +200V. R_{xx} was allowed to stabilize at a constant value so every ramp down measurement had the same initial value.
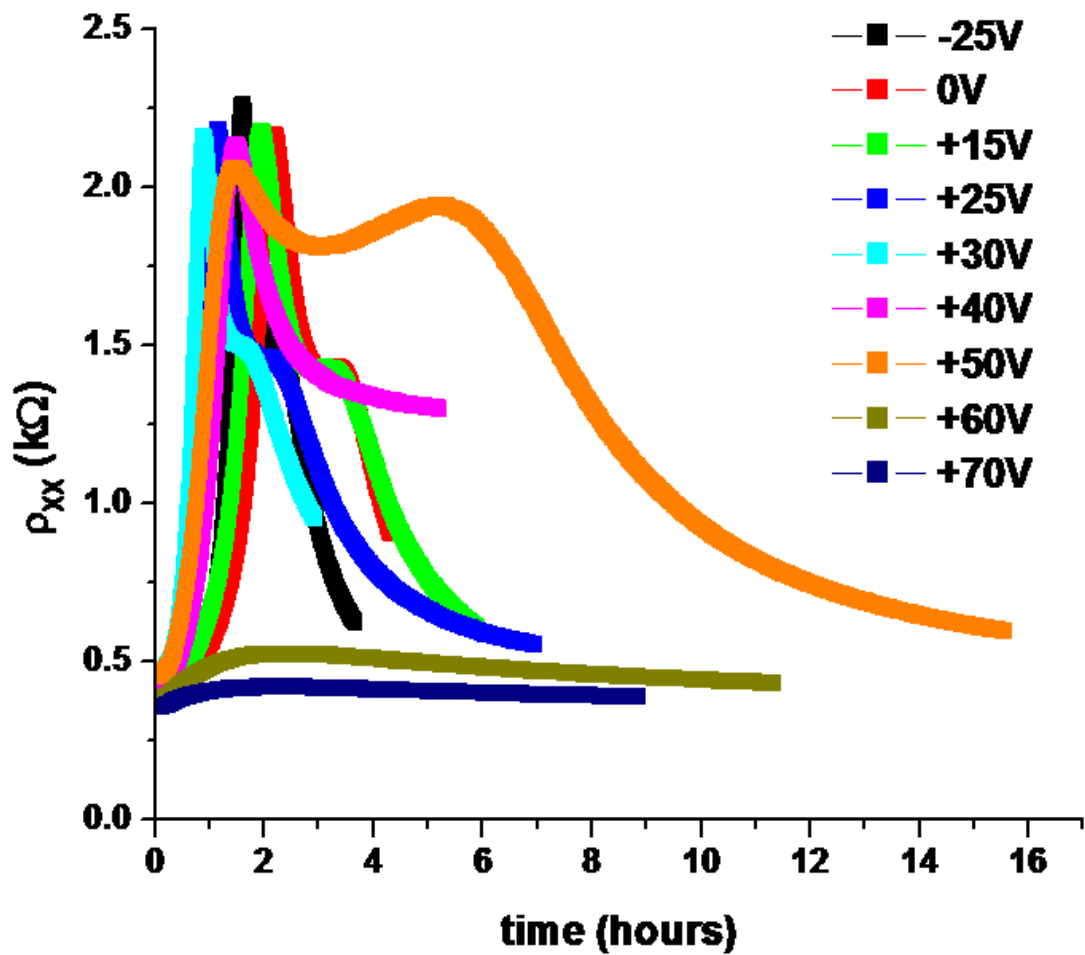
Fig. 6-9 Resistance vs. time for graphene on STO. Each curve began at a stable value at +200V and ramped down to different final voltages. Measurements are taken at 300K.
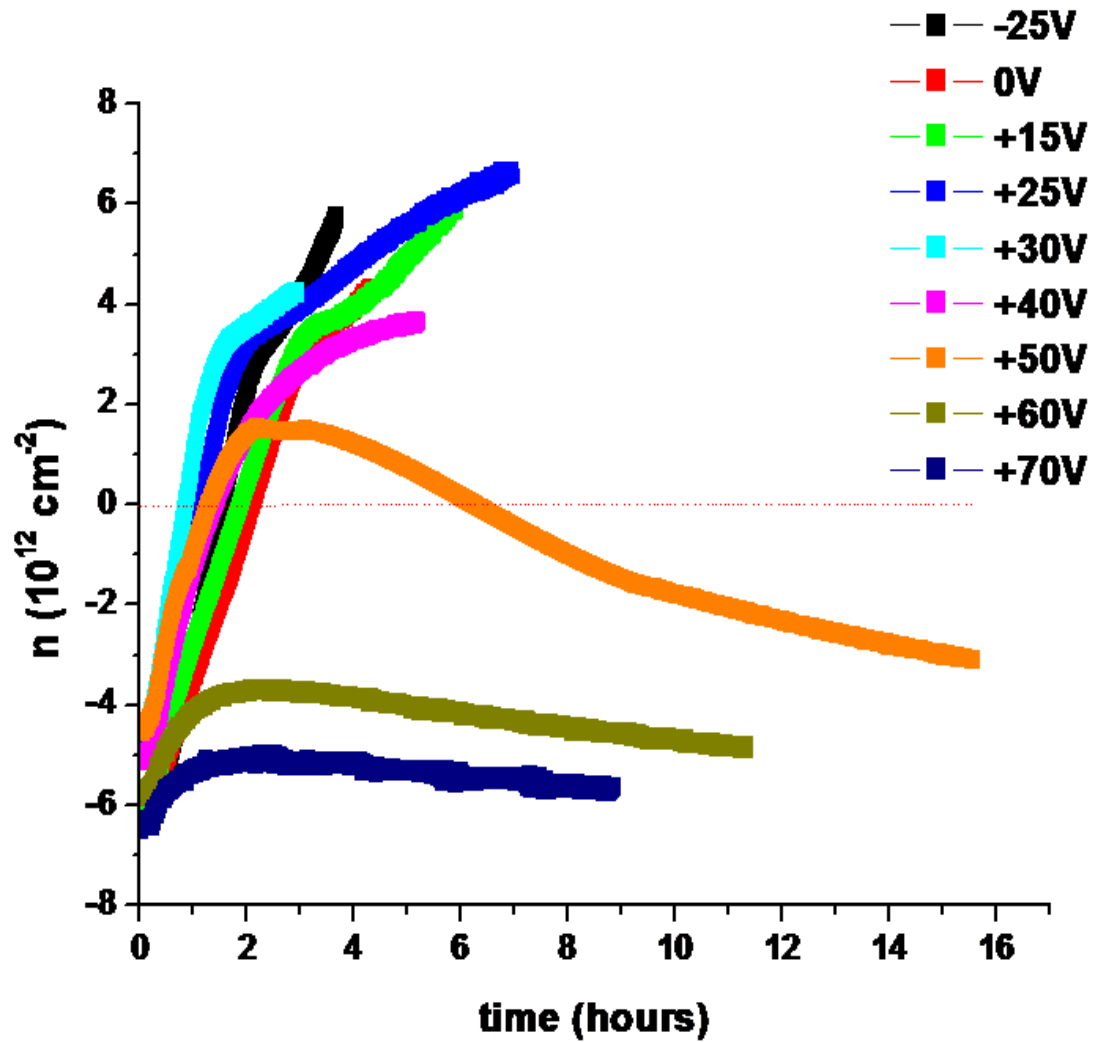
Fig. 6-10 Carrier density vs. time for graphene on STO. +40V and below had a switch of carrier type from electrons to holes. +60V and above showed no carrier switch. +50V exhibited two carrier type switches.
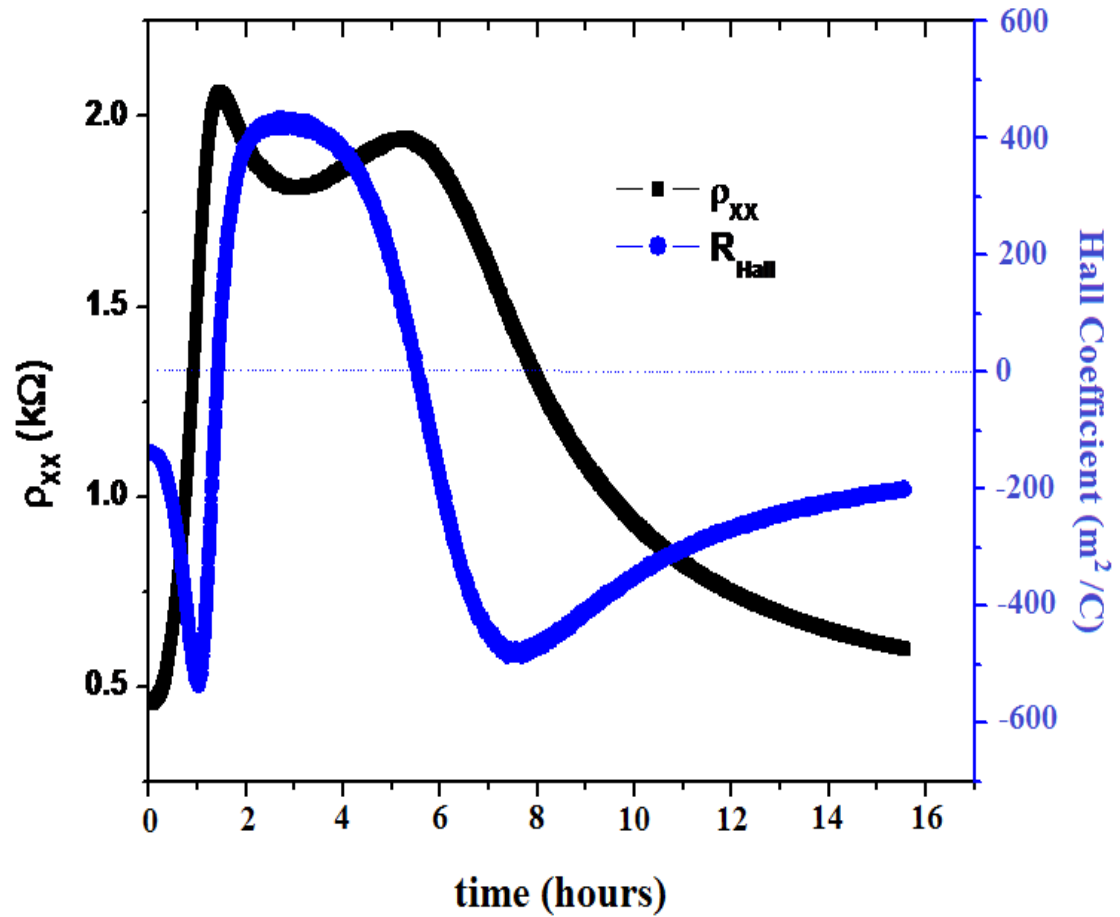
Fig. 6-11 Long relaxation of graphene on STO for final V$_g$ of +50V. Carrier type switches from electrons to holes and back to electrons over time with a constant gate voltage. The time scale for relaxation is much longer than for all other measurements.
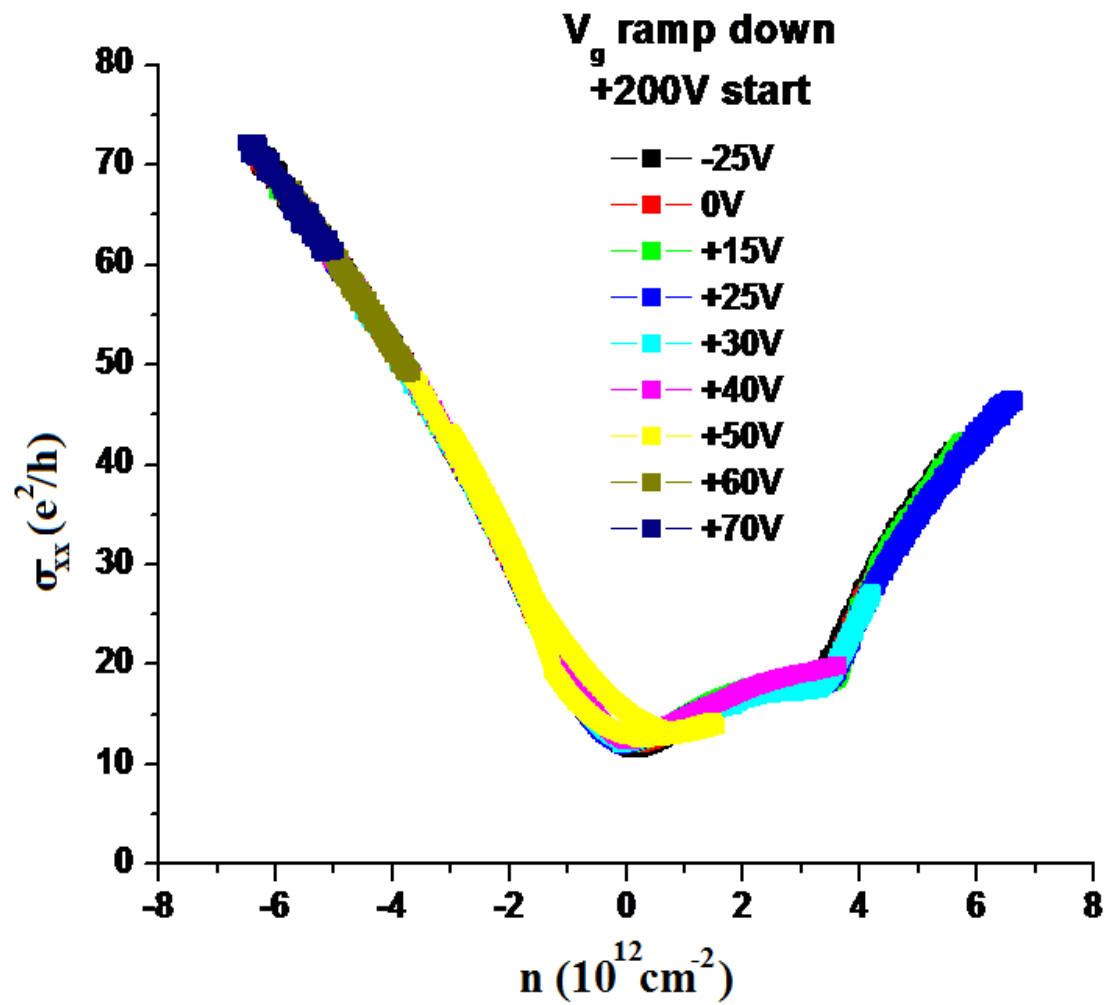
Fig. 6-12 Conductivity vs. carrier density for graphene on STO with differing final V_g. Time is a hidden variable. All curves are identical indicating intrinsic characteristic of graphene electron transport.

6.5　Surface Dipole Model of STO

The hysteresis in the gate dependent measurements and the existence of time dependent relaxation has been a troublesome feature of graphene on the surface of STO. Of the eight devices that have been transferred to STO, every one has had these effects. A few devices I have fabricated from graphene exfoliated directly onto the surface of STO that have also exhibited this behavior. The Morpurgo group has also reported that they have observed hysteresis in the devices on STO and cite this as the reason they keep the gate voltage sweeping range as low as possible [80]. In contrast, a device has been transferred from the surface of SiO_2 to the surface of a separate Si wafer with 300nm SiO_2 with no observed hysteresis or relaxation prior to or after the transfer (Fig. 6-12). This confirms that the hysteretic gate dependence of graphene on STO is a product of STO surface interactions and not a side effect of the transfer technique. As a side note, the mobility of graphene in the SiO_2 to SiO_2 transfer is only reduced by less than 30%, proving the transfer technique is viable and does not cause major degradation of the graphene flake. The position of the Dirac point has not been changed either, indicating a consistent charged impurity environment. More work is needed to verify this as the graphene mobility was low initially. With a low initial mobility, the graphene flake may not be susceptible to addition scatterers possibly induced by the transfer method.
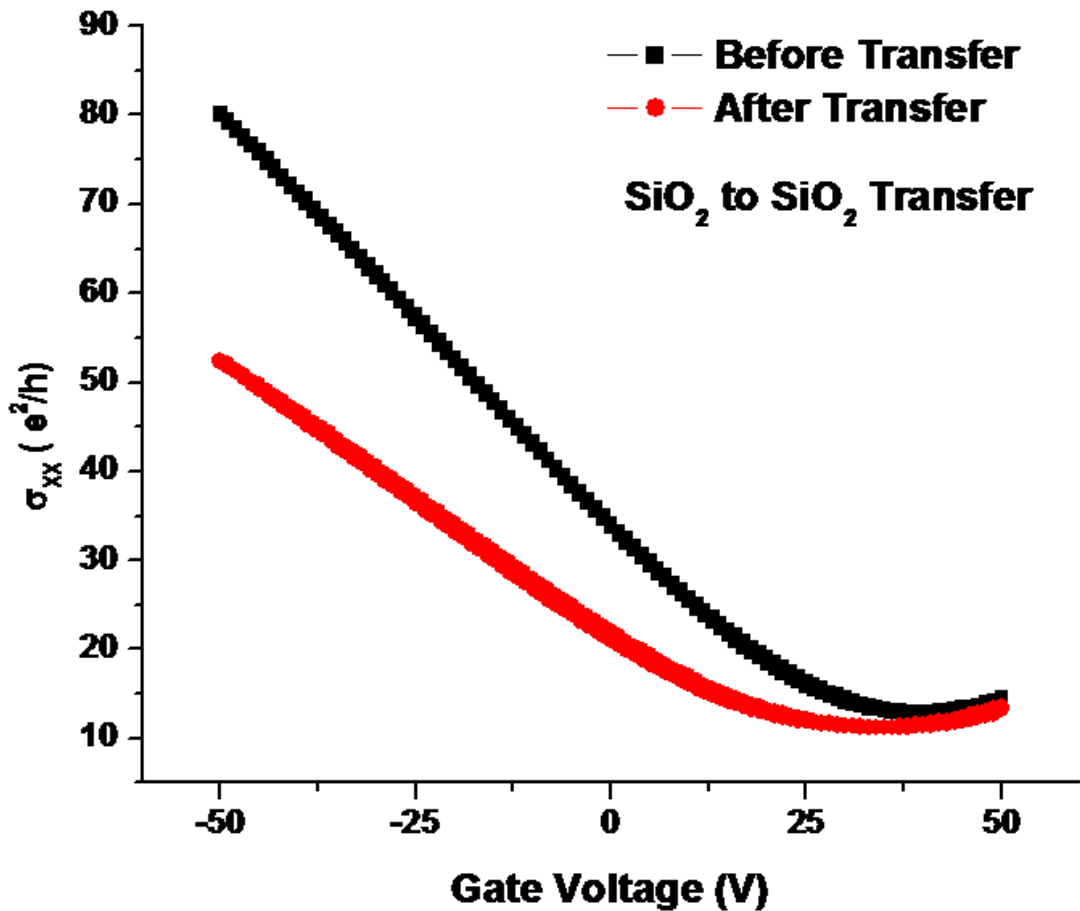
Fig. 6-13 Comparison of graphene transferred from SiO$_2$ to SiO$_2$. No change in position of Dirac point and only small (<30%) decrease in mobility.

The surface of STO(100) is fundamentally different than the bulk properties. Unlike BaTiO$_3$, another perovskite material, bulk STO does not exhibit any ferroelectric behavior at room temperature. The surface, however, does demonstrate ferroelectric polarization due to a "puckering" of oxygen atoms at the surface. The existence of surface dipoles has been studied theoretically [96] and with low energy electron diffraction (LEED) [97]. Both are in agreement that either

of the two surface terminating structures, SrO or TiO_2, results in a dipole moment.

In the bulk material, these atoms all should lie perfectly in a plane. At the surface the

oxygen atoms are pulled out of the plane by a distance $s = 0.08$Å for the TiO_2

terminated and $s = 0.16$Å for the SrO terminated plane (Fig. 6-13). The static

polarization, $P = qs/a^2 d_0$ ($a = 3.9$Å is the lattice constant), caused by the oxygen

displacement has an equivalent value for both surface domains. This is because the

amount of charge displaced, $q(Ti) = 4e = 2q(Sr)$, and the distance of displacement,

$s(Sr) = 2s(Ti)$, gives the same product of $P = 0.17$ C/m² which is near the bulk value

for $BaTiO_3$ at room temperature [93]. P is equal to the surface bound charge density.

A value of $P = 0.17$ C/m² has a corresponding density on the order of 10^{14} cm⁻²
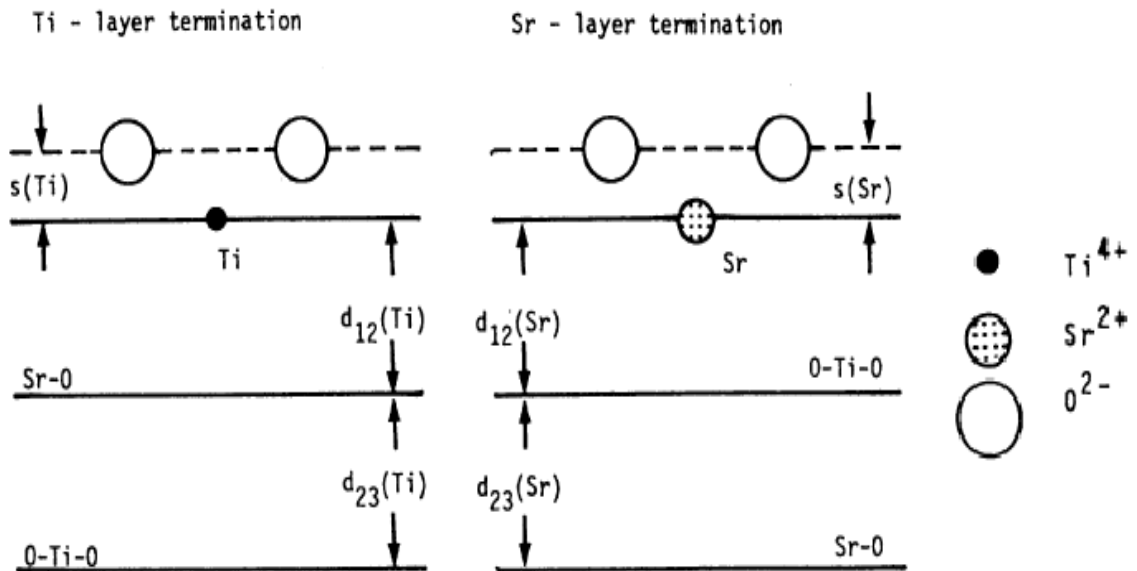
Fig. 6-14 Surface terminating structures for STO(100). Oxygen atoms are displaced out of the plane causing a surface dipole moment [97].

The presence of these surface dipole moments can be used to explain much

of our findings. For every device on 200μm STO, the gate dependent measurements

with large V_g ranges have had the same features of higher carrier density to the left

of the Dirac point (hole carriers) and lower density to the right of the Dirac point

(electron carriers). From Fig. 6-4, the shift due to background bound surface charges

is ~ 3 x 10^{12} cm^{-2}. If we can assume that at zero applied electric field (V_g = 0) the

natural state of the STO(100) surface is a dipole moment with oxygen atoms pulled

out of the surface plane as illustrated in Fig. 6-15a. The dipole moment is in the

direction normal to the surface and down. At V_g = +200V the direction of the applied

electric field is up from the surface, which overcomes the dipole's background

electric field (Fig. 6-15b) and causes the carrier type to be electrons. Sweeping down

to +50V, the applied electric field is strong enough to pull the oxygen atoms close to

the surface plane and causes a long relaxation time, but this state is unstable (Fig. 6-

15c). This instability provides the explanation for the multiple changes in carrier

type over time (Fig. 6-10 and Fig. 6-11). Ramping all the way down to -200V and the

applied electric field is now in the same direction as natural dipole state and causes

the dipole strength to increase (Fig. 6-15d). Because the magnitude of the total

electric field is higher at -200V than +200V, the carrier density is higher.

The unusual carrier density saturation can also be explained by the surface

dipole moments. The applied electric field can vary the direction and the magnitude

of the surface dipoles and these dipoles control the type and density of the charge

carriers in graphene. The maximum magnitude of the dipole moments is dependent on the stretching of the Ti-O and the Sr-O bonds. There is a limit to how far these can be stretched. So therefore, if the magnitude of the surface dipoles saturates, so will the carrier density in graphene.

All measurements for graphene electron transport were finished, the STO chip was deposited with gold on the entire surface and bulk capacitance was measured (Fig. 6-16). The capacitance of bulk STO was a constant value and exhibited no hysteresis. The Au atoms are free to move during the deposition and quench the dipoles by "unpuckering" the O atoms. The carbon atoms in graphene are tightly bound and cannot move freely to quench the dipoles. Due to the atomic thickness and robust bonding, we have evidence that the graphene is sensitive to the surface states of STO.
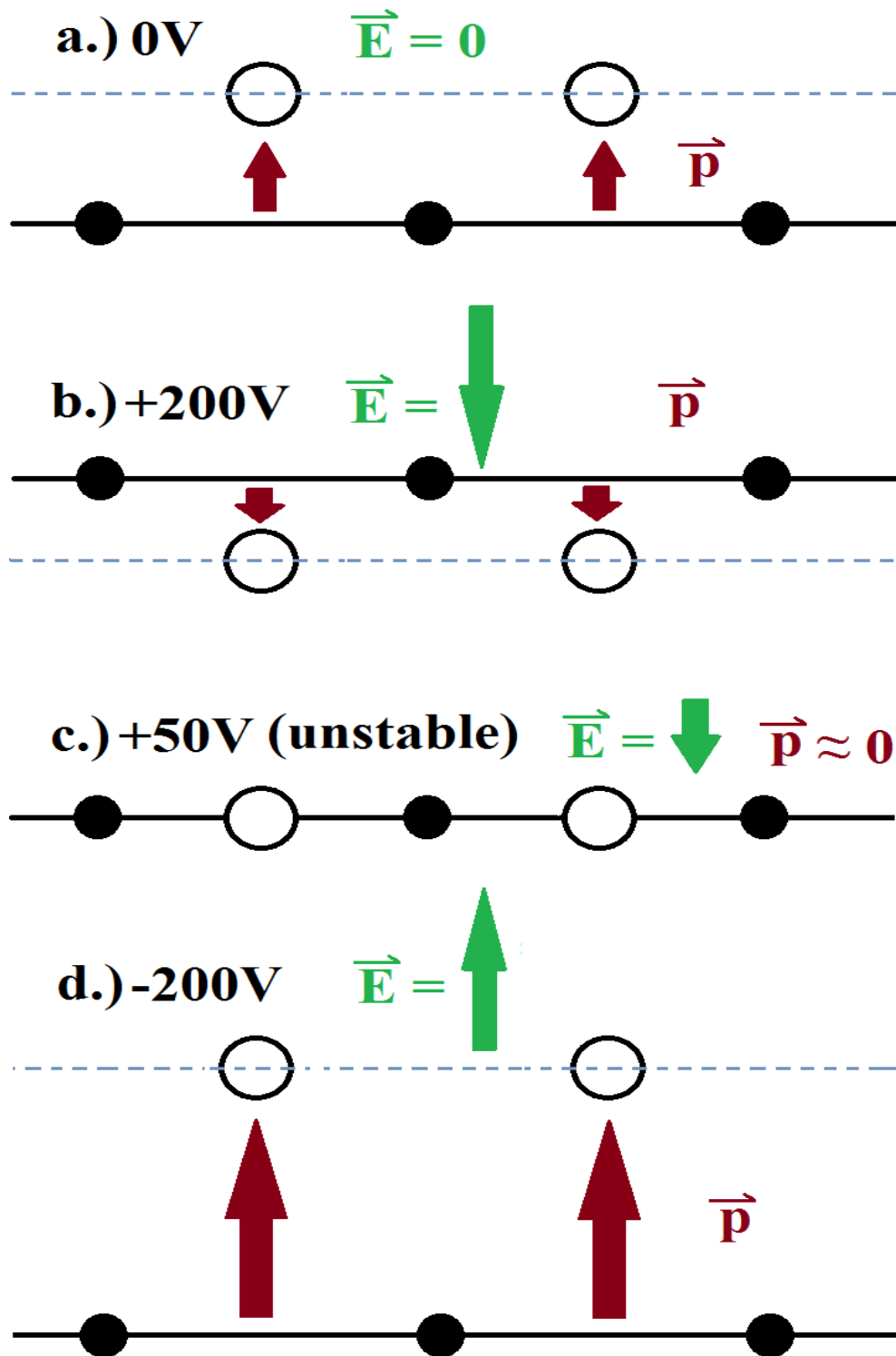
Fig. 6-15 Surface dipole model for STO(100). Orientations and magnitudes of dipole moments are dependent on applied electric field. See text for details.

a.)

$$\frac{V_C}{V_{in}} = \frac{\dfrac{i}{\omega C}}{R + \dfrac{i}{\omega C}} = \frac{1}{1 + (\omega CR)^2} - i\,\frac{\omega CR}{1 + (\omega CR)^2}\;,\;\omega = 2\pi f,\,R = 15.46M\Omega$$

b.)
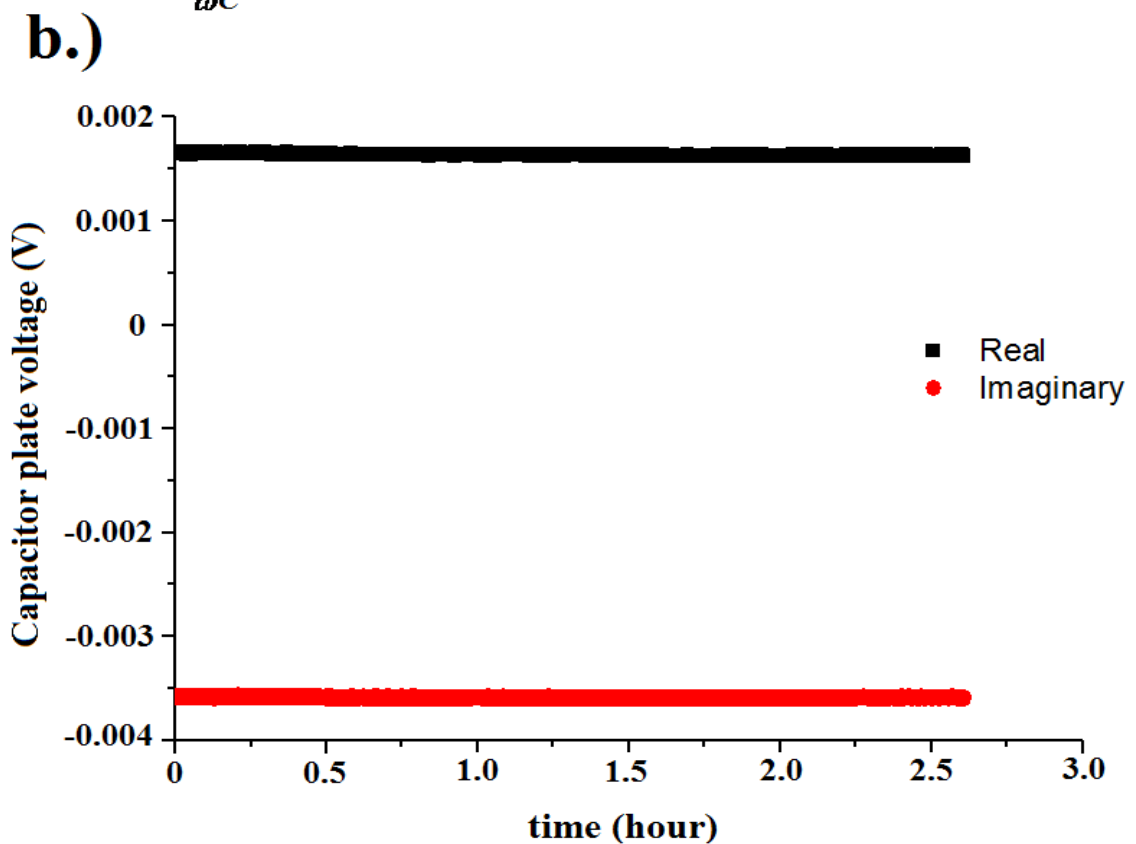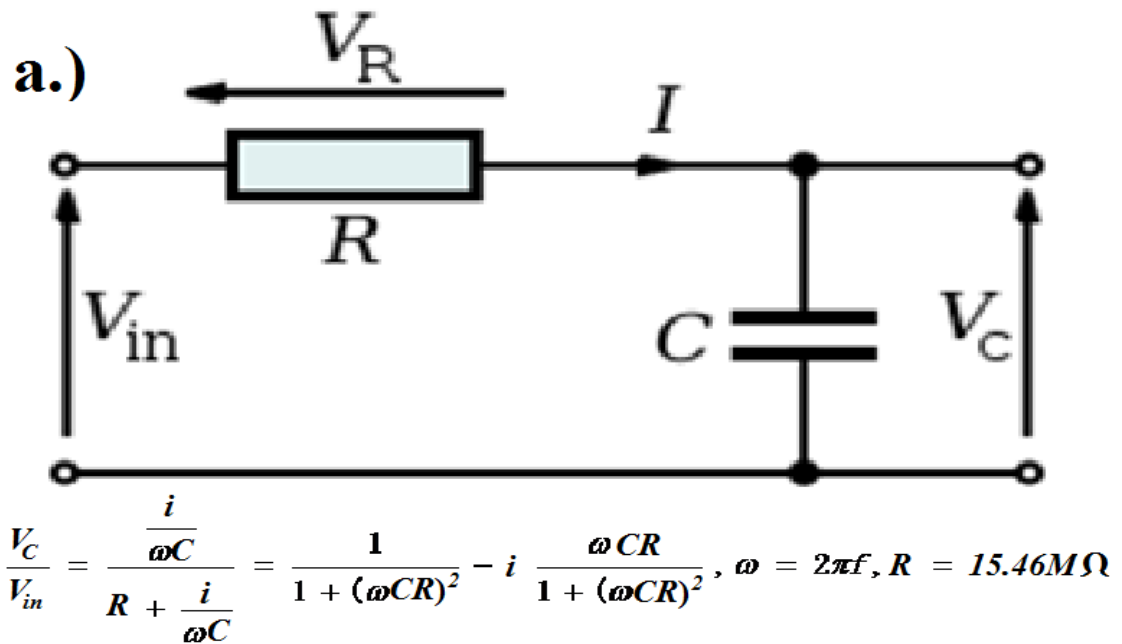
Fig. 6-16 Capacitance measurement of bulk STO. Schematic of measurement setup and capacitance calculation (a). Time dependence showing constant values (time independent) (b).

6.6   Graphene on 250nm STO

STO has been grown on Nb-doped STO(100) via pulsed laser deposition. The details of the growth are in Chapter 5. A graphene device has been successfully transferred to the surface for electrical measurements. A much higher capacitance is achieved and the Dirac point can be swept through with a much smaller gate voltage range (Fig. 6-16). We are able to produce a much more effective graphene FET. The voltage range is limited as the gate leakage becomes unacceptable above 4V at room temperature. Similar gate dependent hysteresis is observed in the thin film STO as with the 200μm thick STO indicating surface dipoles are active, but time dependence was not done with this device. The temperature dependence shows that the Dirac point become sharper at low temperature which would seem to indicate increased mobility (Fig. 18). However, the conductivity vs. density curves for various temperatures are all nearly identical and very close to the value for graphene on SiO_2 (Fig. 6-19). This is the same result as the Morpurgo group [80]. We have been able to reach a higher carrier density with this device. The maximum density of 3×10^{13} cm^{-2} is the highest we have been able to achieve. The density for this device also saturates as indicated by the accumulation of data points at high density in the σ_{xx} vs. n curve (Fig. 6-19). Only one device has been successfully transferred and measured on PLD grown STO. More extensive work needs to be done in order to publish a nice paper in *Science* and *Nature* at the same time. I better be second author!
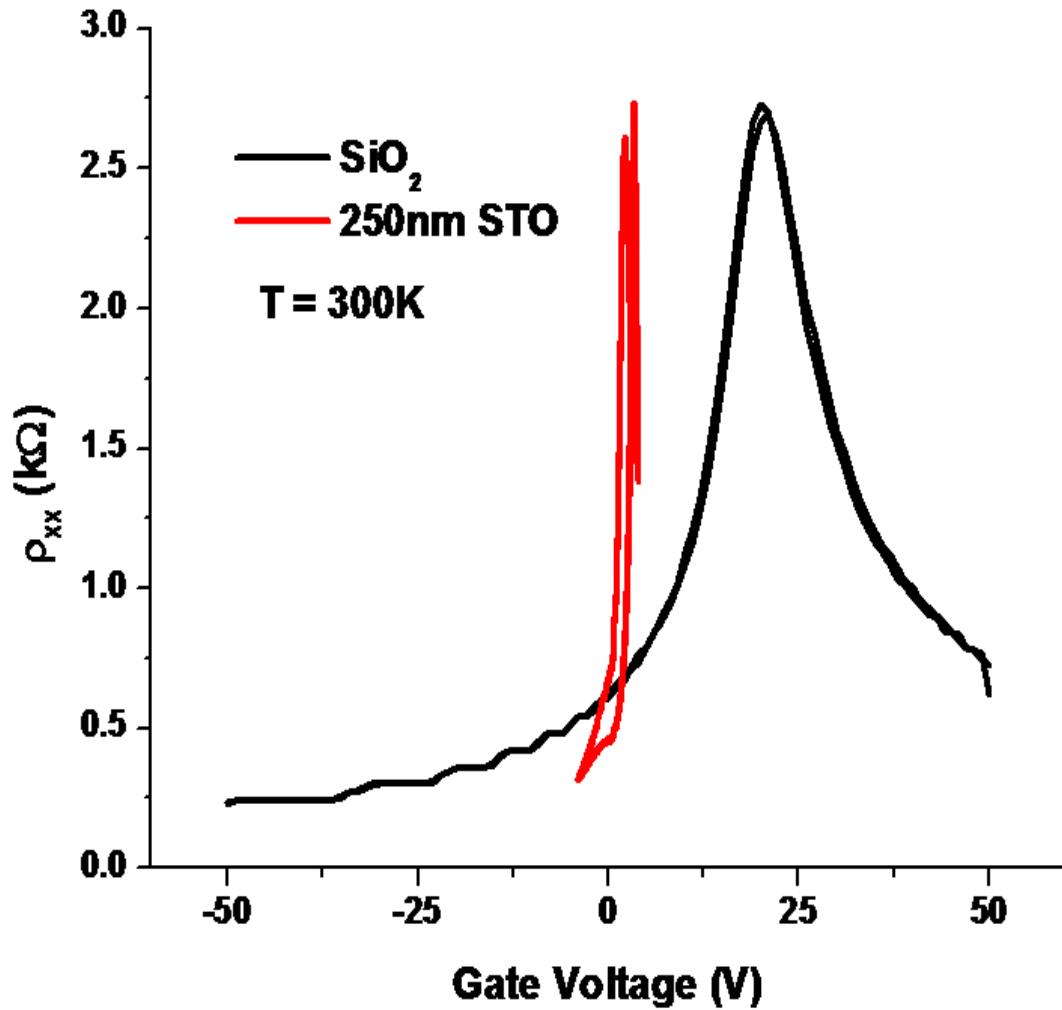
Fig. 6-17 Sheet resistance vs. V_g for graphene on SiO_2 and transferred to 250nm PLD grown STO. The higher capacitance of STO is evident in the smaller gate voltage range needed to sweep through the Dirac point.
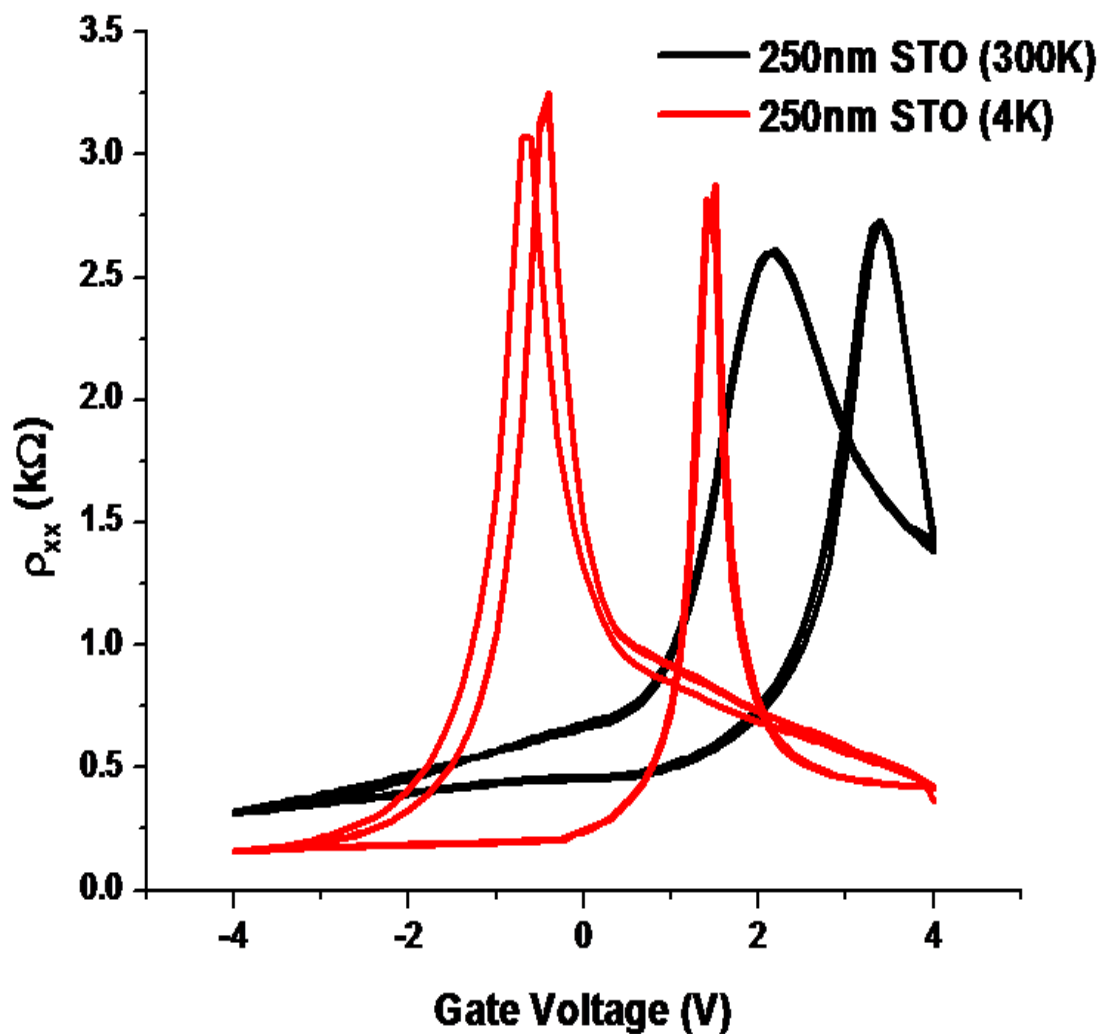
Fig. 6-18 Temperature dependence of graphene on 250nm PLD grown STO. Dirac points become sharper at lower temperature. Hysteresis is still observed in thin films of STO.
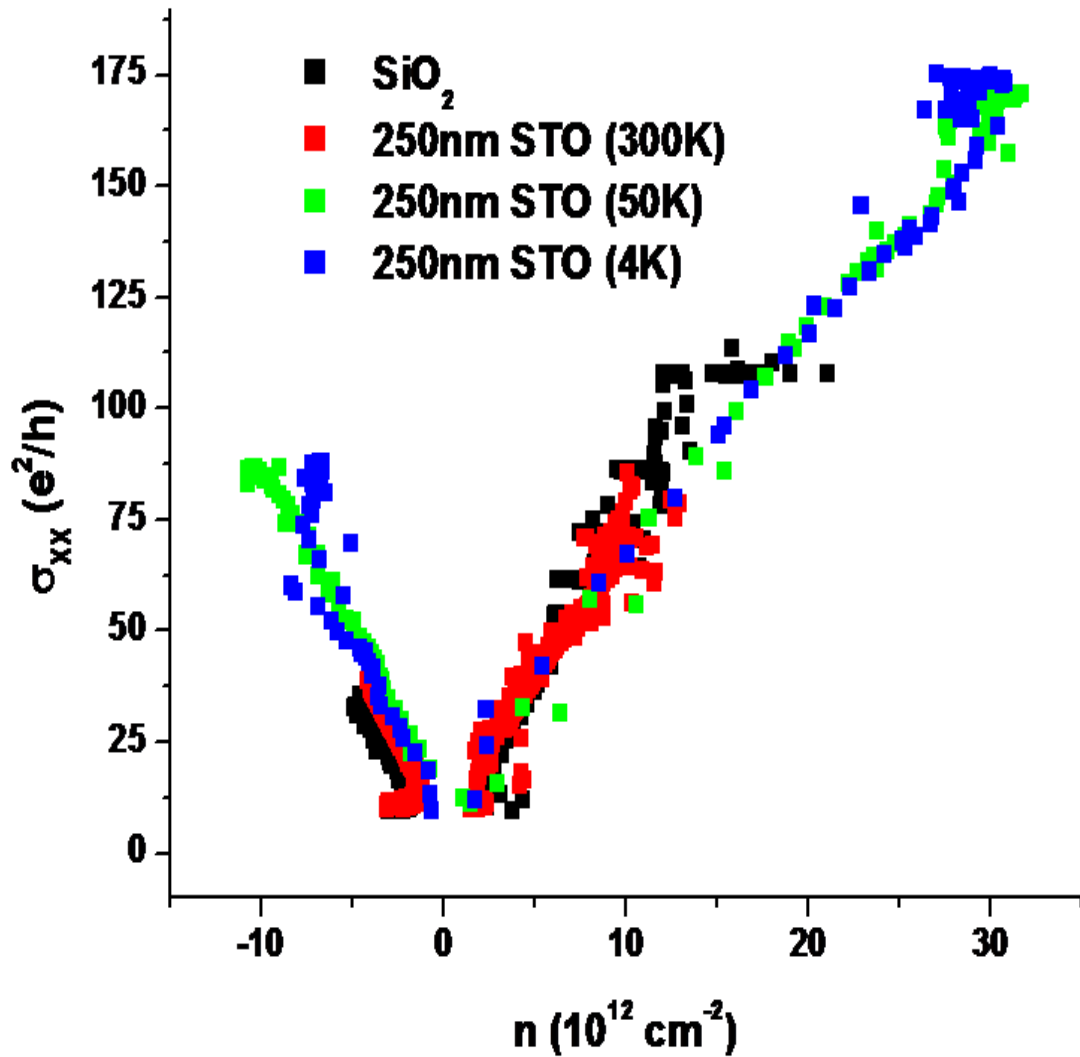
Fig. 6-19 Conductivity vs. density for graphene on SiO$_2$ and transferred to 250nm PLD grown STO. Various temperatures are plotted. Curves overlap nearly perfectly indicating no change in μ. High density of 3 x 10^{13} cm^{-2} is achieved. Density saturation is still occurring.

6.7 Conclusions

Graphene devices have been successfully fabricated on the surface of 300nm SiO_2 wafers. After measuring the electronic properties on SiO_2, the entire device can be peeled from the surface and placed on any arbitrary surface using the device transfer technique that I have developed. A direct comparison of the electronic properties of one device can be made while on the surface of two different substrates. The substrate we have chosen is strontium titanate due to its high dielectric constant which was expected to enhance the screening of charged impurity scattering. An effective screening was not observed, but unusual gate dependent hysteresis and time dependence of the carrier density was measured. These phenomena can be explained by the surface dipole model of STO. It is graphene that is sensitive to the surface states of STO.

References

[1]   K.S. Novoselov *et al.*, Electrical field effect in atomically thin carbon films. *Science* **306**, 666 (2004).

[2]   R.E. Peierls, Quelques proprieties typiques des corpes solides. *Ann. I. H. Poincare* **5**, 177 (1935).

[3]   L.D. Landau, Zur Theorie der phasenumwanlungen II. *Phys. Z. Sowjetunion* **11**, 26 (1937).

[4]   A.K. Geim, K.S. Novoselov, The rise of graphene. *Nature Materials* **6**, 183 (2007).

[5]   A.H. Castro Neto, F. Guinea, N.M.R. Peres, K.S. Novoselov, A.K. Geim, The electronic properties of graphene. *Rev. Mod. Phys.* **81**, 109 (2009).

[6]   K.S. Novoselov *et al.*, Two-dimensional gas of massless Dirac fermions in graphene. *Nature* **438**, 197 (2005).

[7]   Y. Zhang, Y. Tan, H.L. Stormer, P. Kim, Experimental observation of the quantum Hall effect and Berry's phase in graphene. *Nature Letters* **438**, 201 (2005).

[8]   V.P. Gusynin, S.G. Shaparov, Unconventional Integer Quantum Hall Effect in Graphene. *Phys. Rev. Lett.* **95**, 146801 (2005).

[9]   X. Du *et al*. Fractional quantum Hall effect and insulating phase of Dirac electrons in graphene. *Nature Letters* **462**, 192 (2009).

[10]   K. Bolotin, *et al*. Observation of the fractional quantum Hall effect in graphene. *Nature Letters* **462**, 196 (2009).

[11]   K.S. Novoselov, *et al*. Room-Temperature Quantum Hall Effect in Graphene. *Science* **315**, 1379 (2007).

[12]   E. Stolyarova, *et al*. High-resolution scanning tunneling microscope imaging of mesoscopic graphene sheets on an insulating surface. *PNAS* **104**, 22 (2007).

[13]   M. Ishigami, J.H. Chen, W.G. Cullen, M.S. Fuhrer, E.D. Williams. Atomic Structure of Graphene on SiO_2 *Nano Letters*. **7**, 1643 (2007).

[14]   A.A. Balandin *et al*. Superior Thermal Conductivity of Single-Layer Graphene. *Nano Letters* **8**, 902 (2008).

[15]   P. Wei, W. Bao, Y. Pu, C.N. Lau, J. Shi. Anomalous Thermoelectric Transport of Dirac Particles in Graphene. *Phys. Rev. Lett.* **102**, 166808 (2009).

[16]   C. Lee, X. Wei, J.W. Kysar, J. Hone. Measurement of the Elastic Properties and Intrinsic Strength of Monolayer Graphene. *Science* **321**, 385 (2008).

[17]   Q. Zhao, M.B. Nardelli, J. Bernholc. Ultimate strength of carbon nanotubes: A theoretical study. *Phys. Rev. B* **65**, 144105 (2002).

[18]   N. Tombros, C. Jozsa, M. Popinciuc, H.T. Jonkman, B.J. van Wees, Electronic spin transport and spin precession in single graphene layers at room temperature. *Nature* **448**, 571 (2007).

[19]   W. Han *et al*. Electron-hole asymmetry of spin injection and transport in single-layer graphene. *Phys. Rev Lett*. **102** 137205 (2009).

[20]   E.H. Hwang, S. Das Sarma. Acoustic phonon scattering limited carrier mobility in two-dimensional extrinsic graphene. *Phy. Rev. B*. **77**, 115449 (2008).

[21]   J. Chen *et al*. Intrinsic and extrinsic performance limits of graphene devices on SiO_2. *Nature Letters*. **3**, 206 (2008).

[22]   H. Suzuura, T. Ando. Phonons and electron-phonon scattering in carbon nanotubes. *Phys. Rev. B*. **65**, 235412 (2002).

[23]   G. Pennington, N. Goldman. Semiclassical transport and phonon scattering of electrons in semiconducting carbon nanotubes. *Phys. Rev. B*. **68**, 045426 (2003).

[24]   S. Fratini, F. Guinea, Sustrate-limited electron dynamics in graphene. *Phys. Rev. B*. **77**, 195415 (2008).

[25]   B. Laikhtman, P.M. Solomon. Remote phonon scattering in field-effect transistors with a high κ insulating layer. *J. of App. Phys*. **103**, 014501 (2008).

[26]   M. Fischetti, D. Neumayer, E. Cartier. Effective electron mobility in Si inversion layers in metal-oxide-semiconductor systems with high-κ insulator: The role of remote phonon scattering. *J. of Appl. Phys.* **90**, 4587 (2001).

[27]   K. Zhou *et al*. Deposition of High-Quality HfO_2 on Graphene and the Effect of Remote Oxide Phonon Scattering. *Phys. Rev. Lett*. **105**, 126601 (2010).

[28]   K. Bolotin *et al*. Temperature-Dependent Transport in Suspended Graphene. *Phys. Rev. Lett*. **101**, 096802 (2008).

[29]   M. Katsnelson, A. Geim. Electron scattering on microscopic corrugations in graphene. *Phil. Trans. R. Soc. A*. **366**, 195 (2007).

[30]   S. Adam, S. Das Sarma. Scattering mechanisms and Boltzmann transport in graphene. *Physica E.* **40**, 1022 (2008).

[31]   T. Low *et al*. Deformation and Scattering in Graphene over Substrate Steps. *Phys. Rev. Lett*. **108**, 096601 (2012).

[32]   S. Ji *et al*. Atomic-scale transport in epitaxial graphene. *Nat. Mat*. **11**, 114 (2012).

[33]   E. H. Hwang, S. Adam, S. Das Sarma. Carrier Transport in Two-Dimensional Graphene Layers. *Phys. Rev. Lett*. **98**, 186806 (2007).

[34]   Y. Tan *et al*. Measurement of Scattering Rate and Minimum Conductivity in Graphene. *Phys. Rev. Lett*. **99**, 246803 (2007).

[35]   J. Yan *et al*. Raman scattering and tunable electron-phonon coupling in single layer graphene. *Solid State Comm*. **143**, 39 (2007).

[36]   X. Du *et al*. Approaching ballistic transport in suspended graphene. *Nat. Nanotech*. **3**, 491 (2008).

[37]   K. Bolotin *et al*. Temperature-Dependent Transport in Suspended Graphene. *Phys. Rev. Lett*. **101**, 096802 (2008).

[38]   J. Chen *et al*. Defect Scattering in Graphene. *Phy. Rev. Lett*. **102**, 236805 (2009).

[39]   R. Narula, S. Reich. Double resonant Raman spectra in graphene: A two-dimensional explanation of the Raman amplitude. *Phys. Rev. B*. **78**, 165422 (2008).

[40]   J. Katoch *et al*. Uncovering the dominant scatterer in graphene sheets on SiO_2. *Phys. Rev. B*. **82**, 081417 (2010).

[41]   D. Elias *et al*. Control of Graphene's Properties by Reversible Hydrogenation: Evidence for Graphane. *Science* **323**, 610 (2009).

[42]   T. Ando. Screening and Impurity Scattering in Monlayer Graphene. *J. Phys. Soc. Japan* **75**, 074716 (2006).

[43]   T. Wehling *et al*. Adsorbates on graphene: Impurity states and electron scattering. *Chem. Phys. Lett*. **476**, 125 (2009).

[44]   K. Nomura, A. MacDonald. Quantum Transport of Massless Dirac Fermions. *Phys. Rev. Lett*. **98**, 076602 (2007).

[45]   S. Adam *et al*. A self-consistent theory for graphene transport. *Proc. Natl. Acad. Sci. USA* **104**, 18392 (2007).

[46]   M. Trushin, J. Schliemann. Minimum Electrical and Thermal Conductivity of Graphene: A Quasiclassical Approach. *Phys. Rev. Lett*. **99**, 16602 (2007).

[47]   F. Schedin *et al*. Detection of individual gas molecules adsorbed on graphene. *Nature Letters*. **6**, 652 (2007).

[48]   J. Chen *et al*. Charged-impurity scattering in graphene. *Nature Letters*. **4**, 377 (2008).

[49]   J. Chen *et al*. Diffusive charge transport in graphene on SiO_2. *Sol. State. Comm*. **149**, 1080 (2009).

[50]   J. Yan, M. Fuhrer. Correlated Charged Impurity Scattering in Graphene. *Phys. Rev. Lett*. **107**, 206601 (2011).

[51]   A. Efros *et al*. Maximum low-temperature mobility of two-dimensional electrons in heterojunctions with a thick spacer layer. *Phys. Rev. B*. **41**, 8295 (1990).

[52]   P. T. Coleridge. Small-angle scattering in two-dimensional electron gases. *Phys. Rev. B*. **44**, 3793 (1991).

[53]   E. Buks, M. Heiblum, H. Shtrikman. Correlated charged donors in a two-dimensional electron gas. *Phys. Rev. B*. **49**, 790 (1994).

[54]   Q. Li *et al*. Theory of 2D Transport in Graphene for Correlated Disorder. *Phys. Rev. Lett*. **107**, 156601 (2011).

[55]   K. McCreary *et al*. Effect of cluster formation on graphene mobility. *Phys. Rev. B*. **81**, 115453 (2010).

[56]   M. Katsnelson, F. Guinea, A. Geim. Scattering of electrons in graphene by clusters of impurities. *Phys. Rev. B*. **79**, 195426 (2009).

[57]   M. Fuhrer. *Diffusive Charge Transport in Graphene*. KITP Program: Low Dimensional Electron Systems (2009) Conference Presentation.

[58]   A. Sommerfeld. *Atomic Structure and Spectral Lines*. Methuen (1921). Print

[59]   A. Ruark, H. Urey. *Atoms, Molecules and Quanta*. McGraw-Hill (1930) Print.

[60]   C. Jang *et al*. Tuning the Effective Fine Structure Constant in Graphene: Opposing Effects of Dielectric Screening on Short- and Long-Range Potential Scattering. *Phys. Rev. Lett*. **101**, 146805 (2008).

[61]   L. Ponomarenko *et al*. Effect of a High-κ Environment on Charge Carrier Mobility in Graphene. *Phys. Rev. Lett*. **102**, 206603 (2009).

[62]   F. Chen *et al*. Dielectric Screening Enhanced Performance in Graphene FET. *Nano Letters* **9**, 2571 (2009).

[63]   F. Chen, J. Xia, N. Tao. Ionic Screening of Charged-Impurity Scattering in Graphene. *Nano Letters* **9**, 1621 (2009).

[64]   A. Newaz *et al*. Probing charge scattering mechanisms in suspended graphene by varying its dielectric environment. *Nat. Comm*. **3**, 734 (2012).

[65]   D. Wang *et al*. Manipulating Graphene Mobility and Charge Neutral Point with Ligand-Bound Nanoparticles as Charge Reservoir. *Nano Letters* **10**, 4989 (2010).

[66]   D. Jena, A. Konar. Enhancement of Carrier Mobility in Semiconductor Nanostructures by Dielectric Engineering. *Phys. Rev. Lett.* **98**, 136805 (2007).

[67]   B. Fallahazad *et al*. Dielectric thickness dependence of carrier mobility in graphene with HfO_2 top dielectric. *App. Phys. Lett.* **97**, 123105 (2010).

[68]   J. Shim *et al*. Water-Gated Charge Doping of Graphene Induced by Mica Sustrates. *Nano Letters*. **12**, 648 (2012).

[69]   W. Gannett *et al*. Boron nitride substrates for high mobility chemical vapor deposited graphene. *App. Phys. Lett.* **98**, 242105 (2011).

[70]   M. Yankowitz *et al*. Emergence of superlattice Dirac points in graphene on hexagonal boron nitride. *Nat. Phys.* **8**, 382 (2012).

[71]   C. Dean *et al*. Boron nitride substrates for high-quality graphene electronics. *Nat. Nanotech.* **5**, 722 (2010).

[72]   H. W. Gandy. Optical Transmission of Heat-Treated Strontium Titanate. *Phys. Rev.* **113**, 795 (1959).

[73]   Ana C. L. S. Marques. Advanced Si pad detector development and $SrTiO_3$ studies by emission channeling and hyperfine experiments. **http://hdl.handle.net/10451/1643** Doctoral Thesis (2009).

[74]   V. M. Goldschmidt. *Geochemistry*. Oxford Univ. Press (1958).

[75]   F. W. Lytle. X-ray Diffractometry of Low-Temperature Phase Transformations in Strontium Titanate. *J. App. Phys.* **35**, 2212 (1964).

[76]   D. E. Grupp, A. M. Goldman. Giant Piezoelectric Effect in Strontium Titanate at Cryogenic Temperatures. *Science*. **276**, 392 (1997).

[77]   H. Frederikse, W. Thurber, W. Hosler. Electronic Transport in Strontium Titanate. *Phys. Rev. Lett.* **134**, A442 (1964).

[78]   M. Itoh et al. Ferroelectricity Induced by Oxygen Isotope Exchange in Strontium Titanate Perovskite. *Phys. Rev. Lett.* **82**, 3540 (1999).

[79]   R. A. Cowley. Lattice Dynamics and Phase Transitions of Strontium Titanate. *Phys. Rev. Lett.* **134**, (1964).

[80]   N. Cuoto, B. Sacépé, A. Morpurgo. Transport through graphene on SrTiO$_3$. *Phys. Rev. Lett.* **107**, 225501 (2011).

[81]   B. Bußmann, O. Ochedowski, M. Schleberger. Doping of graphene exfoliated on SrTiO$_3$. *Nanotechnology*. **22**, 265703 (2011).

[82]   S. Luryi. Quantum capacitance devices. *Appl. Phys. Lett.* **52**, 501 (1988).

[83]   S. Sonde *et al*. Influence of substrate dielectric permittivity on local capacitive behavior in graphene. *Physica E*. (2011), doi:10.1016/j.phye.2011.01.019

[84]   F. Giannazzo *et al*. Mapping the Density of Scattering Centers Limiting the Electron Mean Free Path in Graphene. *Nano Letters*. **11**, 4612 (2011).

[85]   B. Kim, T. Brintlinger, E. Cobas, M. Fuhrer. High-performance carbon nanotube transistors on SrTiO$_3$/Si substrates. *Appl. Phys. Lett.* **84**, 1946 (2004).

[86]   Y.-S. Shin *et al*. High-Mobility Graphene Nanoribbons Prepared Using Polystyrene Dip-Pen Nanolithography. *J. Amer. Chem. Soc.* **133**, 5623 (2011).

[87]   S. Das Sarma, Q. Li. Graphene on SrTiO$_3$. *Sol. Stat. Comm.* **152**, 1795 (2012).

[88]   C. Berger *et al*. Ultrathin Epitaxial Graphite: 2D Electron Gas Properties and a Route toward Graphene-based Nanoelectronics. *J. Phys. Chem. B*. **108**, 19912 (2004).

[89]   Q. Yu *et al*. Graphene segregated on Ni surfaces and transferred to insulators. *Appl. Phys. Lett.* **93**, 113103 (2008).

[90]   A. Reina *et al*. Large-Area, Few-Layer Graphene Films on Arbitrary Substrates by Chemical Vapor Deposition. *Nano Letters*. **9**, 30 (2009).

[91]   X. Li *et al*. Large-Area Synthesis of High-Quality and Uniform Graphene Films on Copper Foils. *Science*. **324**, 1312 (2009).

[92]   A. C. Ferrari *et al*. Raman Spectrum of Graphene and Graphene Layers. *Phys. Rev. Lett.* **97**, 187401 (2006).

[93]   Z. Cheng *et al*. Toward Intrinsic Graphene Surfaces: A Systematic Study on Thermal Annealing and Wet-Chemical Treatment of SiO_2-Supported Graphene Devices. *Nano Letters*. **11**, 767 (2011).

[94]   A. Reina *et al*. Transferring and Identification of Single- and Few-Layer Graphene on Arbitrary Substrates. *J. of Phys. Chem. C*. **112**, 17741 (2008).

[95]   M. Einenkel, K. Efetov. Possibility of Superconductivity due to electron-phonon interaction in graphene. *Phys. Rev. B*. **84**, 214508 (2011).

[96]   V. Ravikumar, D. Wolf, V. Dravid. Ferroelectric-Monolayer Reconstruction of the $SrTiO_3$ (100) Surface. *Phys. Rev. Lett*. **74**, 960 (1995).

[97]   N. Bickel *et al*. Ferroelectric Relaxation of the $SrTiO_3$(100) Surface. *Phys. Rev. Lett*. **62**, 2009 (1989).

[98]   S. Cho, M. Fuhrer. Charge transport and inhomogeneity near the minimum of conductivity point in graphene. *Phys. Rev. B*. **77**, 081405 (2008).